Institut für Erd- und Umweltwissenschaften

Quantification of ground motions by broadband simulations

by
Katrin Kieling

In fulfilment of the requirements for the degree
"doctor rerum naturalium"
(Dr. rer. nat.)
for the scientific discipline "Geophysics"
submitted to the Faculty of Mathematics and Natural Sciences
at the University of Potsdam

University of Potsdam
Institute of Geosciences

June 22, 2015

Published online at the
Institutional Repository of the University of Potsdam:
URN urn:nbn:de:kobv:517-opus4-85989
http://nbn-resolving.de/urn:nbn:de:kobv:517-opus4-85989

"Ever tried. Ever failed. No matter.
Try again. Fail again.
Fail better."

Samuel Beckett

Notation

Some symbols are used frequently in this dissertation. This list shall provide an overview of what the symbols mean.

u	slip, displacement
k	wavenumber
v_p	compressional-wave (= P-wave) velocity
v_s	shear-wave (= S-wave) velocity
v_r	rupture velocity
γ	proportionality factor between v_r and v_s
M	seismic moment
M_w	Moment magnitude
M_e	Energy magnitude
τ	rise time
$\Delta\sigma$	stress drop
η	parameter fixing taper width
α	exponent for fractal distribution
κ	parameter defining the amplitude fall-off in the frequency domain
μ	rigidity
ρ	density
PGA	peak ground acceleration
PGV	peak ground velocity

Contents

Abstract

In many procedures of seismic risk mitigation, ground motion simulations are needed to test systems or improve their effectiveness. For example they may be used to estimate the level of ground shaking caused by future earthquakes. Good physical models for ground motion simulation are also thought to be important for hazard assessment, as they could close gaps in the existing datasets. Since the observed ground motion in nature shows a certain variability, part of which cannot be explained by macroscopic parameters such as magnitude or position of an earthquake, it would be desirable that a good physical model is not only able to produce one single seismogram, but also to reveal this natural variability.

In this thesis, I develop a method to model realistic ground motions in a way that is computationally simple to handle, permitting multiple scenario simulations. I focus on two aspects of ground motion modelling. First, I use deterministic wave propagation for the whole frequency range – from static deformation to approximately 10 Hz – but account for source variability by implementing self-similar slip distributions and rough fault interfaces. Second, I scale the source spectrum so that the modelled waveforms represent the correct radiated seismic energy. With this scaling I verify whether the energy magnitude is suitable as an explanatory variable, which characterises the amount of energy radiated at high frequencies – the advantage of the energy magnitude being that it can be deduced from observations, even in real-time.

Applications of the developed method for the 2008 Wenchuan (China) earthquake, the 2003 Tokachi-Oki (Japan) earthquake and the 1994 Northridge (California, USA) earthquake show that the fine source discretisations combined with the small scale source variability ensure that high frequencies are satisfactorily introduced, justifying the deterministic wave propagation approach

even at high frequencies. I demonstrate that the energy magnitude can be used to calibrate the high-frequency content in ground motion simulations.

Because deterministic wave propagation is applied to the whole frequency range, the simulation method permits the quantification of the variability in ground motion due to parametric uncertainties in the source description. A large number of scenario simulations for an M=6 earthquake show that the roughness of the source as well as the distribution of fault dislocations have a minor effect on the simulated variability by diminishing directivity effects, while hypocenter location and rupture velocity more strongly influence the variability. The uncertainty in energy magnitude, however, leads to the largest differences of ground motion amplitude between different events, resulting in a variability which is larger than the one observed.

For the presented approach, this dissertation shows (i) the verification of the computational correctness of the code, (ii) the ability to reproduce observed ground motions and (iii) the validation of the simulated ground motion variability. Those three steps are essential to evaluate the suitability of the method for means of seismic risk mitigation.

Zusammenfassung

In vielen Verfahren zur Minimierung seismischen Risikos braucht man Seismogramme, um die Effektivität von Systemen zu testen oder diese zu verbessern. So können realistische Bodenbewegungen genutzt werden, um das Ausmaß der Erschütterungen durch zukünftige Erdbeben abzuschätzen. Gute physikalische Bodenbewegungsmodelle haben auch das Potential, Lücken in den beobachteten Datensätzen zu schließen und somit Gefährdungsabschätzungen zu verbessern. Da die in der Natur beobachtete Bodenbewegung einer gewissen Variabilität unterliegt, von der ein Teil nicht durch makroskopische Parameter wie Magnitude oder Position des Erdbebens erklärt werden kann, ist es wünschenswert, dass ein gutes physikalisches Modell nicht nur ein einzelnes Seismogramm produziert, sondern auch die natürliche Variabilität widerspiegelt.

In dieser Arbeit beschreibe ich eine Methode zur Modellierung von realistischen Bodenbewegungen, die – aufgrund ihrer einfachen Modellkonfiguration – mehrere Szenario-Simulationen ermöglicht. Dabei konzentriere ich mich auf zwei Aspekte: Einerseits nutze ich ein deterministisches Verfahren für die Wellenausbreitung für den gesamten Frequenzbereich, von der statischen Deformation bis etwa 10 Hz, unter Berücksichtigung der Variabilität der Quelle durch die Einbeziehung von selbstähnlichen Slipverteilungen und rauen Störungsflächen. Andererseits skaliere ich das Quellspektrum so, dass die modellierte Wellenform die abgestrahlte seismische Energie wiedergibt. Damit überprüfe ich, ob die Energie-Magnitude als Stellgröße geeignet ist, die den Anteil der Energie beschreibt, der im Hochfrequenzbereich abgestrahlt wird. Der Vorteil der Energie-Magnitude ist, dass diese aus Beobachtungen, sogar in sehr kurzer Zeit, ermittelt werden kann.

Anwendungen der entwickelten Methode für das Wenchuan (China) Erdbeben von 2008, das Tokachi-Oki (Japan) Erdbeben von 2003 und das Northridge (Kalifornien, USA) Erdbeben von 1994

demonstrieren, dass durch eine feine Diskretisierung und kleinskalige Variabilität in der Quelle hohe Frequenzen ausreichend in die Wellenform eingeführt werden, was den deterministischen Ansatz auch im Hochfrequenzbereich bestätigt. Ich zeige, dass die Energie-Magnitude verwendet werden kann um den Hochfrequenzanteil in Bodenbewegungssimulationen zu kalibrieren.

Da die determistische Wellenausbreitung auf den gesamten Frequenzbereich angewandt wird, können die Variabilitäten, die durch parametrische Unsicherheiten in der Quellbeschreibung entstehen, beziffert werden. Zahlreiche Simulationen für ein M=6 Beben zeigen, dass die Rauigkeit der Quelle und die Slipverteilung durch Minderung der Direktivitätseffekte die simulierte Variabilität der Bodenbewegung gernfügig verringern. Dagegen haben die Bruchgeschwindigkeit und die Lage des Hypozentrums einen stärkeren Einfluss auf die Variabilität. Die Unsicherheit in der Energie-Magnitude dagegen führt zu großen Unterschieden zwischen verschiedenen Erdbebensimulationen, welche größer sind als die beobachtete Variabilität von Bodenbewegungen.

In Bezug auf die vorgestellte Methode zeigt diese Arbeit (i) den Nachweis der Richtigkeit des Computerprogramms, (ii) die Eignung zur Modellierung beobachteter Bodenbewegung und (iii) den Vergleich der simulierten Variabilität von Bodenbewegung mit der beobachteten. Dies sind die ersten drei Schritte auf dem Weg zur Nutzbarkeit von Bodenbewegungssimulationen in Maßnahmen zur Verminderung des seismischen Risikos.

Chapter 1

Introduction

The main goal of this dissertation is the development of a model to simulate the ground motion caused by earthquakes and the investigation of the most influential model parameters. The modelling approach reproduces the main characteristics of seismic waveforms generated by earthquake ruptures while the model itself is relatively simple. Earthquake rupture characteristics are easy to modify and the simulations are computationally less expensive than other methods. This allows for a series of simulations to study the influence of source variability on ground motion and its variability.

This introductory chapter reveals the importance of ground motion simulations in the context of seismic risk assessment. After shortly reviewing current research topics and open questions in waveform modelling, I summarise the measures taken in the course of this work to fill some of the existing gaps.

1.1 Motivation

Strong ground motions caused by earthquakes pose a major threat to buildings and structures and thereby endanger people living in an ever more densely populated society. Among the other earthquake hazards such as tsunamis, landslides, or liquefaction, ground shaking is the one causing most injuries, fatalities and economic losses. Despite the growing knowledge about the Earth, earthquake processes and cycles, the prediction of events is still impossible. Since we currently have no way to predict earthquakes, the only way to cope with them is to mitigate their effects. Risk mitigation implies that the vulnerability of the society is reduced. An important measure is the application of correct building codes, which are based on the calculation of engineers who consider possible ground motions caused by earthquakes.

Engineering applications require estimates of strong ground motions for wide ranges of distances and earthquake magnitudes. Unfortunately, the existing records only represent a small subset of possible earthquake scenarios. Modelling of ground motion seems to be an ideal aspirant to satisfy these engineering needs. For the determination of structural

responses and damage estimation, information on amplitude, phase as well as duration are of significant importance. These parameters can be calculated from simulations of broadband seismic waveforms. Ideally, a good model does not only give one good simulation but the probability distribution for the relevant ground motion parameters. This means that the mean ground motion and its variability can be estimated. Equally important are realistic ground motion time series for a wide frequency band, as those are needed in performance based seismic design, where the building or facility is constructed such that it complies with various performance goals e. g. "collapse prevention", "downtime for less than three months", or "life safety", and the damage following various scenarios has to be determined in shaking tests. At present, usually recorded ground motions are used in these tests. But as the maximum earthquake magnitude is unlikely already recorded in the region of interest, observed seismograms have either to be scaled to the desired intensity or adopted from other regions, where stronger earthquakes were actually recorded. In the future, simulations could provide the ground motion caused by the envisioned earthquake magnitude in the chosen region.

Earthquake risk mitigation does not only mean the regulation of building designs and constructions. It also includes fast reaction to an occurring earthquake. Earthquake early warning or earthquake early response systems (e. g. Zollo et al., 2009, Picozzi et al., 2013) can prevent losses and save lives, for example by automatically stopping high-speed trains, closing bridges and gas-pipelines, or starting the emergency shut-down of nuclear power plants. By issuing announcements via modern media even individual persons can be warned. Realistic simulations of ground motions are used as a synthetic data generator for testing such early warning or response systems. Seismograms have to be used to check whether the system would give the right warnings in case of an earthquake.

Additionally, realistic simulations are of seismological interest. They may give us deeper insights into the influence of different source parameters on the resulting ground motion. These simulations could also help to identify which characteristics of source and propagation have the strongest effect on ground motions.

And finally, different source scenarios give us the ability to estimate the variability of ground motions and thus to quantify the uncertainties connected to them. This actually brings us back to the subject of earthquake risk mitigation, since quantification of the uncertainties is of central importance for the further development of Probabilistic Seismic Hazard Analysis, which is currently the most common tool for the estimation of seismic design loads. For structures and facilities the damage of which would cause many fatalities or injuries, such as nuclear power plants, the correct estimation of the variability of ground motion is crucial for the determination of the recurrence interval which has to be met with the respective design load.

1.2 Research topics

Much attention was devoted to the task of providing synthetic ground motions that match observations for the whole frequency band. Although empirical Ground Motion Prediction Equations (GMPE) are well established and provide very reasonable results, there is also a need for good physical models, which are applicable even in regions with sparse data coverage or for hitherto unrecorded scenarios. Even though it may be debatable whether simulations can ever outperform empirical relations in the cases of good data coverage, they will surpass GMPEs in extreme scenarios.

Realistic models should approximately reproduce amplitude and duration, frequency content and phases. Several different methods have been developed in the past to meet this challenge, a selection of which I will shortly review in chapter 2. Historically, the quality of the simulations improved with increasing knowledge about rupture processes and with the increasing number of parameters determined from observations. In the 1960s, seismologists could determine the seismic moment with rather good accuracy (Aki, 1966) and it was already known that an earthquake looks like a double-couple – a pair of opposing forces – in the far-field. Therefore simulations of ground motions were based on point source simulations. Those were able to explain observed low-frequency ground motion at a certain distance from the source. With increasing knowledge about rupture processes and with first results from inversions of seismic waveforms to sources with variable displacement along a fault plane of a certain size, the simulation of extended faults was established. But still this was only possible for relatively low frequencies. A major question was and still is the handling of high-frequency ground motion and their seemingly stochastic nature. Hanks and McGuire (1981) state that it is virtually impossible to synthesise high-frequency ground motion deterministically. They claim that it requires at least one stochastic parameter. In contrast, Aki (2003) believes that "it may be a viable goal for strong motion seismologists to use entirely deterministic modelling, at least for path and site effects, before the end of the twenty-first century." However, current simulations still rely on deterministic modelling only for the low-frequency range (Graves and Pitarka, 2010; Pacor et al., 2005). The high-frequency band is modelled by a stochastic approach. The question remains, whether the same deterministic techniques applied for low-frequency simulations can be equally applied to the high-frequency range.

Another important issue in kinematic ground motion modelling is the amount of energy radiated in the high-frequency band. In kinematic source modelling the dislocation along the fault is specified as a function of space and time without explicit consideration of a physical model for the rupture process which leads to reduced computational requirements. From the modeller's point of view, the high-frequent energy release has to be fixed by a parameter defining the duration of the dislocation of a point along the fault (the rise time of the moment-rate function), or the equivalent parameter in the frequency domain describing the source displacement spectrum (the corner frequency). Usually this is done by either empirically constraining the rise time (Graves and Pitarka, 2010) or by fixing

the stress drop (the difference in stress on the fault before and after the earthquake) and relating the rise time to the subfault size (Zeng et al., 1994). In either way the rise time itself or the stress drop have to be fixed empirically or by an educated guess. A possibility to constrain the rise time of the moment-rate function from observation would be useful to reduce the number of unknown parameters in the model which are variable for each earthquake.

Once a simulation approach is developed, its advantages can also be exploited to find out more about ground motions themselves. Currently the approach used most often to estimate seismic design loads is Probabilistic Seismic Hazard Analysis (PSHA). In practice, this procedure does not consider whole waveforms but is based on empirical Ground Motion Prediction Equations. These are obtained from a regression analysis of recorded data and give estimates of ground motion parameters such as peak ground acceleration (PGA), peak ground velocity (PGV), or spectral acceleration at discrete frequencies. The uncertainty connected to the prediction from the GMPE strongly influences the calculated hazard (Bommer and Abrahamson, 2006). On the other hand, the epistemic uncertainty of ground motion can be reduced when more knowledge is acquired (Atik et al., 2010). Numerical simulations could help to disaggregate the variability into its components belonging to path, site or source effects. They can quantify the influence of single parameters or the reduction in variability if we were to know more explanatory variables.

Finally, physics based simulations are considered to close certain gaps in the datasets for empirical ground motion prediction. Abrahamson (2012) pointed out some criteria that have to be met by simulations in order to be incorporated in seismic hazard studies. Those criteria include not only the verification of the computational correctness and the calibration to observed ground motion, but also validation of the variability, transparency of the methods, and robustness of the results with respect to other simulation methods. Some of these points, such as the verification and calibration, are usually addressed by authors of simulation codes. Thorough validation and comparison of physics-based simulations was recently presented within the SCEC Broadband Platform validation program (Dreger et al., 2015). However, ground motion variability is rarely validated, although well constrained ground motion variability is a substantial requirement for the use of synthetic data in seismic hazard studies.

1.3 Novelties of the approach

In this work I concentrate on the development of a simulation method for broadband seismograms, i. e. waveforms that cover the frequency band from static deformation up to approximately 10 Hz. The modelling procedure includes some of the existing knowledge about the physics of earthquake processes. Unlike empirical methods, which rely on databases of similar settings, this makes the approach applicable even to regions without prior earthquakes and to distance and magnitude ranges with sparse data coverage. In contrast to previous approaches, I use a deterministic wave propagation for the whole

frequency range up to 10 Hz. By using an analytical approach and a simple, layered earth-model, the computational efforts for calculating Green's functions are reduced. Characteristics of complex ground motions at high frequencies and close to the fault are reproduced by considering small-scale slip variability and fault roughness. In this way, stochastic features are included in the source description. This corresponds to "shifting" all causes for high-frequency contributions to the rupture process instead of including further scattering effects in the path or site description. Part of the scattering effect which is caused by heterogeneities in the subsurface is mimicked by variations of source mechanism throughout the fault, which leads to a similar smoothing of the radiation pattern. The prolongation of the signal by scattering effects is accounted for only by the reflection and refraction of the waves at interfaces of the velocity layers. I show that it is possible to model the whole frequency range with the same simulation approach, namely by calculating high-frequency ground motion using the same tools as the low-frequency ground motion. The use of small scale source variations permits a number of different source scenarios with the same major parameters obtained from observations. By simulating different scenarios not only one possible ground motion parameter is obtained but a range of values, the mean and variance of which express the intensity of probable ground shaking and the respective uncertainty.

An important new ingredient of the methodology is the combined use of two different magnitudes for constraining the rise time of the moment-rate function: the moment magnitude M_w and the energy magnitude M_e. Thereby I avoid a guessed or empirically constrained stress drop. For my purpose it is therefore desirable that the two magnitudes are determined independently but considered jointly during the simulation of the ground motion. Additionally, using different (but statistically reasonable) energy magnitudes for the same moment magnitude may be useful when simulating scenarios for future earthquakes, as this could show the range of possible ground motions.

Finally, I estimate the simulated variability of ground motion in a quantitative way. In the presented study, I concentrate on the parametric uncertainty, due to parameters not known prior to an earthquake or parameters which we cannot observe with sufficient precision. Here, I focus on the variance caused by the source variability. Simulations of different source scenarios, with an alteration of diverse source parameters result in a sensitivity study of the dependence of ground motions and ground motion variability on source characteristics.

1.4 Structure of this work

This work starts with a review of some of the already established ground motion modelling approaches in Chapter 2. Here, I concentrate only on simulations which result in complete waveforms. I show the relation of my approach to the known methods and point out for what purposes my simulation is especially appropriate. In Chapter 3 I introduce a method which combines a kinematic source description including several stochastic components

with a purely deterministic waveform propagation. The simulation steps are described in detail. I apply the approach to the Wenchuan (2008) earthquake, the Tokachi-Oki (2003) earthquake, and the Northridge (1994) earthquake in Chapter 4. Chapter 5 elaborates on the influence of different source parameters on the resulting ground motions. It shows which ground motion variability is caused by the observed range of source parameters. Finally a conclusion and suggestions for future work are given in Chapter 6.

Chapter 2

Ground motion modelling

The modelling of seismic waveforms at the surface following an earthquake rupture has to deal with two key aspects: the description of the source process and the wave propagation. Both points may be addressed in different ways, each having its specific advantages and disadvantages. Figure 2.1 summarises the ground motion modelling approaches I will introduce here. It shows that the benefit of increasingly physical consistent and realistic results comes at the cost of higher computational power and time and requires a more detailed knowledge of the model parameters.

Already several different methods for modelling ground motions exist. A detailed review of techniques for predicting earthquake ground motions can be found in the survey of Douglas and Aochi (2008). In the following two sections I will give a rough overview over the most commonly used source description and wave propagation methods. Given the respective benefits and drawbacks of the individual methods, this shows which gap my approach is going to close. Here, I concentrate on waveform modelling only and do not describe methods that estimate only certain parameters of the seismic motion such as ground motion prediction equations (GMPE) estimating response spectra.

2.1 Source description approaches

When simulating ground motions the first challenge is the description of the rupture process. As with every natural process there is trade-off between a physically realistic and consistent description, and the computational cost this causes. Moreover, we face the problem that we do not know all the details of natural rupture processes: (i) the distribution of slip is unknown at small scales; (ii) the exact form of the rupture plane is unknown; (iii) the time-dependence of each point's slip in the fault is unknown. These uncertainties are present in every description of a rupture process.

Kinematic models of earthquakes prescribe the slip as a function of space and time without explicit consideration of the physical causes of the rupture process. Usually they

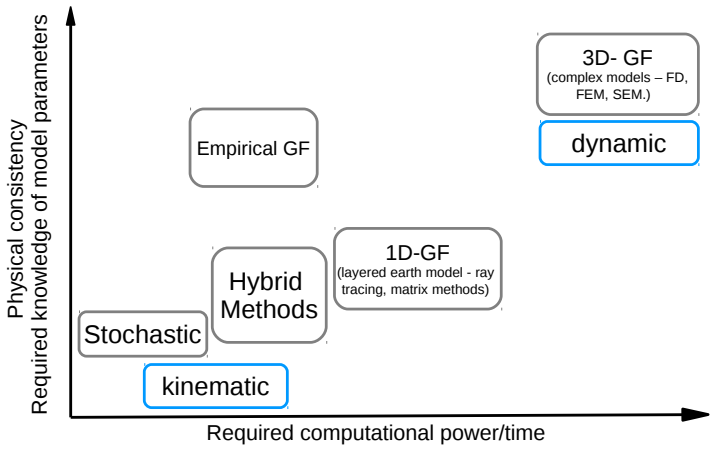

Figure 2.1: Illustration of the benefits and requirements of the different methods used for the simulation of seismic waveforms (with GF short for Green's Functions). Positions of the different methods show their qualitative relation to computational cost, required model parameter knowledge and physical consistency. Grey encircled keywords refer to wave propagation approaches, blue encircled ones to source descriptions.

discretise the fault plane into evenly spaced subfaults and assume a certain moment release function, source mechanism, and rupture velocity for each subfault. Using the respective Green's functions, the seismogram at the receiver is calculated via the representation theorem[1]. The special case of composite source models (e. g. Zeng et al., 1994) distributes subevents randomly on a fault plane and sums up the contributions of all subevents. Computationally, kinematic models are easy to handle, the limiting factor being the discretisation step. Therefore, complex fault planes can be modelled (e. g. multiple fault segments), different slip distributions and rupture velocities may be tested, and single rupture simulations run in shorter time than with the respective dynamic models. One disadvantage is that the predescribed parameters may be physically inconsistent. However, Guatteri et al. (2003) showed that the lack of physics in kinematic descriptions can be compensated by introducing physically consistent slip distributions and rupture pro-

[1]Following Aki and Richards (2002) the representation theorem can be described via

$$u_n(x,t) = \int_{-\infty}^{\infty} d\tau \int\int_{\Sigma} u_i(\xi,\tau) \cdot c_{ijpq} \cdot \nu_j \cdot \frac{\partial}{\partial \xi_q} G_{np}(x, t-\tau, \xi, 0) d\xi$$

(using the Einstein summation convention). It says that the n-th component of the observed displacement field at the location x at time t, $u_n(x,t)$, is represented by the ith component of the displacement discontinuity (slip) at the source as a function of position ξ on the fault plane and time τ, $u_i(\xi,\tau)$, and the Green's function $G_{np}(x, t-\tau, \xi, 0)$, which is the system's response in n-direction due to unit impulse in direction p on the fault plane at (ξ,τ). c_{ijpq} is the elasticity tensor and ν_j the normal to the fault plane.

cesses. Another point is that seismological observation shows that the source radiation and the wave propagation tend to become stochastic at high frequencies (Hanks and McGuire, 1981). We are not able to resolve source characteristics at small scales from data inversion. Hence it is questionable whether kinematic modelling of source processes at high frequencies is appropriate. As a solution stochastic methods are introduced when generating the source properties at small scales (Hisada, 2001; Graves and Pitarka, 2010)

Dynamic models (e. g. Olsen et al., 1997; Ripperger et al., 2008) usually satisfy the elastodynamic equations with a prescribed fracture criterion on a predetermined fault plane which is loaded with a certain shear stress. Seismic waves are radiated by a dynamically running shear crack. The passing rupture front causes a certain shear stress drop. Generally the evolution of the rupture (the static slip, the rupture velocity and corresponding rupture times) depends on the initial conditions and the failure criterion, i. e. the conditions under which a fault patch is supposed to slip. Therefore, the rupture evolution is physically consistent. However, dynamic descriptions are computationally expensive. Hence, it is difficult to perform them in short times or to run several simulations in order to investigate certain parameter ranges or model different scenarios. Usually they also cover only a limited frequency range (Ripperger et al., 2008; Inoue and Miyatake, 1998), because higher frequencies would need more resources for the calculation. Again the limiting factor is the discretisation step. However, dynamic simulations are computationally much more demanding than kinematic simulations with the same discretisation. Studies that compare dynamic simulations to observed ground motion are rare (Olsen et al., 1997), due to the stress field on the fault prior to the earthquake being unknown but a requirement for simulation of past earthquakes. On the other hand the dynamic simulation can be of special value for the simulation of future earthquakes, as they cover the possible source scenarios in a physically consistent way.

2.2 Wave propagation methods

What applies to the source description is equally valid for the simulation of the wave propagation: we have to make a compromise between the necessity to produce ground motions consistent with the underground structure and the time and computational resources at our disposal. In the end it also depends on whether we know the subsurface structure and topography in enough detail to use complex models or we have to use a simpler model reflecting our missing knowledge of the region of interest.

Stochastic methods do not make use of Green's functions. They assume that each source radiates an ω^{-2} displacement spectrum and use empirical distance-dependent duration, geometric spreading and attenuation models to describe path effects (e. g. Boore, 1983; Boore and Atkinson, 1987). In the most basic approach, the kinematic source description is reduced to a point source. The source as well as path effects are simulated by

calculating a deterministic point source spectrum for the given magnitude and stress drop and multiplying it with the Fourier transform of a windowed random noise signal. More recent approaches (Beresnev and Atkinson, 1998; Motazedian and Atkinson, 2005) apply the method to extended faults, where contributions from multiple point subsources are summed up with according time delays, thereby allowing to include a simplified kinematic source description. Stochastic simulations usually perform well at predicting amplitude and frequency content at large distances over a wide frequency range. Estimates of the ground motions can be derived from them at a much lower cost than they can from other modelling approaches. However, they do not provide correct phase information or good representation of near-fault ground motion in the time domain. Moreover, stochastic models in general calculate seismograms for one wavetype only (Boore, 2003) - mostly the shearwave. They neglect the contribution of other wavetypes, such as surface waves, the influence of which increases with increasing distance from the fault. The method does not consider a specific underground model, which makes it easy to use even in poorly known areas but also reduces the value of its results in cases where structural and topographic effects have a major influence on the ground motion.

Deterministic simulations calculate ground motions of dislocation point sources (i. e. Green's functions) by numerical (e. g. discrete wavenumber/finite element technique, Hartzell and Helmberger, 1982) or semi-analytical methods (e. g. ray theory, Heaton and Helmberger, 1979). The wavefield is then calculated using the representation theorem (Aki and Richards, 2002). Those deterministic methods result in correct phases and amplitudes as long as the subsurface structure is appropriately modelled. They reproduce the full wavefield and directivity effects. However, they need a dense grid of Green's functions along the fault to correctly model of high frequencies. Furthermore, the parameters describing the rupture process have to be prescribed on this fine grid at scales for which we often do not have sufficient knowledge. The Green's functions themselves come either from a 1D- or 3D-model. **1D-Green's functions** are calculated in a layered halfspace for different fault-depth-receiver pairs. Once calculated they are saved in a database and can be reused for different faults and receivers, as long as the same layered halfspace applies. This is their most important advantage, as the same database is applied to the whole region of interest. With this approach, the mean velocity model is correctly represented. However, 1D-Green's function cannot represent geological structures and topography. Unfortunately, site effects like sedimentary basins and topography can significantly influence the resulting ground motions. To include this effects in the simulation, we have to rely on **3D-Green's functions**. Those can include essentially all the available subsurface and topography information. Their disadvantage is the high computational effort and the fact that they have to be calculated explicitly for each fault-receiver pair as they depend on the exact fault and receiver location. If the fault is shifted by only a few kilometres, different Green's functions have to be calculated.

Empirical Green's functions (EGF) approaches use observations from smaller earthquakes in the region of interest as Green's functions (Hartzell, 1978; Irikura and Kamae, 1994; Frankel, 1995). This approach gives reasonably good results for a broad frequency spectrum, as the frequency content is constrained such that the results satisfy the ω^{-2} law. The frequency range is limited by the bandwidth of the EGF record having a sufficiently high signal to noise ratio. The subsurface structure mainly influencing the low-frequency ground motion is already represented in the observations of the small events resulting in synthetics with approximately correct low-frequent pulsing and phasing. The EGF approach is probably the one with the best balance between cost and benefit. Since the Green's functions are not calculated but chosen from the database of small events, the computational costs are rather small. On the other hand the obtained frequency spectrum is broad and the real 3D-structure and topography are already included. For this reason, EGF forms an outlier in Figure 2.1 where the other approaches form a line with higher accuracy implying higher computational costs. Unfortunately, records of earthquakes with the needed magnitude and spatial distribution are not always available, making it difficult to apply the method in regions with infrequent earthquakes. Also, variations in the focal mechanism cannot be modelled by empirical Green's functions.

Hybrid simulations finally use a deterministic approach to model the low-frequency part of the ground motion and a stochastic approach to model the high-frequency part (Graves and Pitarka, 2010; Pitarka et al., 2000; Mena et al., 2010; Gallovič and Brokesova, 2007). Thus, they capture the advantages of each method. This makes them a very good tool for broadband modelling of ground motions, even for large earthquakes. The main disadvantage of hybrid methods is that the combination of the two simulation results is not trivial. Often the cross-over frequency range is between 0.5 and 3 Hz, a range of the ground motion spectrum which is of rather high importance for the final broadband seismogram, as the eigenfrequencies of buildings with several stories lie in that frequency band.

2.3 Synopsis

The choice for the best method to fit the specific concerns of ground motion modelling depends on a number of points:

- The information available on the source process and the state of the fault prior to the earthquake
- The computational costs affordable
- The physical consistency which needs to be ensured
- The number of different scenarios which need to be investigated

For example, if the response of a building to possible earthquakes in the surrounding areas should be investigated, one would need broadband seismograms. As only few things about the rupture are known beforehand (such as fault size), a number of scenario simulations is needed to investigate the possible range of ground motions. Hence one should choose a low-cost approach which anyway gives broadband solutions. Another case would be a microzonation study to asses the site amplification due to a specific geological setting in an area where only one distant fault contributes to the seismic hazard. It would require only a small number of scenarios, but in a highly resolved 3D-underground model. Consequently, single simulations have to be computationally more expensive.

In the following chapters I introduce a ground motion simulation approach that uses a kinematic source description combined with a semi-analytical method to calculate 1D-Green's functions. In the source description I include a stochastic distribution of slip. This helps to introduce the natural variability of ground motions close to the earthquake fault. In contrast, the wave propagation is purely deterministic, even at high frequencies.

The usage of deterministic wave propagation for modelling high-frequency ground motion is unusual. Most often deterministic approaches are used in hybrid modelling schemes together with stochastic approaches at high frequencies. However the stochastic component of my approach is found in the source description. My supposition is that it is sufficient to include stochastic effects in the source description to reproduce realistic ground motions. The kinematic properties of the source are determined such that they are physically consistent. For example I use self-similar slip at high wavenumbers and mimic rough fault surfaces.

As seen in Figure 2.1 the combination of a kinematic rupture description with deterministic 1D-Green's functions is computationally easy to manage but does not take the 3D-velocity structure and the topography into consideration. The approach is therefore only useful in the cases when 3D-effects are of minor importance or when the 3D-structure is not known. However, the simplicity makes it very suitable for investigation of the influence of source effects on the ground motions. The uncertainties in ground motion simulation coming from the source description can be investigated and quantified. Among the physics based ground motion modelling approaches this combination is certainly a computationally low-cost one, making it especially attractive for scenario simulations.

Chapter 3

Method

In this chapter I describe the developed ground motion modelling approach. The method consists of four steps: the kinematic description of the source, a rise time scaling to the radiated seismic energy, the Green's function modelling and finally the convolution of the Green's functions with their respective source time function and the superposition of the waveforms for each receiver. I validate the Green's function calculation and the convolution and superposition by comparing the results for a simple fault plane with homogeneous slip to the calculation of Käser and Gallovič (2008). A further example shows inaccuracies coming from insufficient discretisation and ways to improve this behaviour with techniques which are affordable in terms of computational costs.

Major parts of this chapter are based on an article published in the Bull. Seis. Am. Soc. Kieling et al. (2014). The software GENSO , which I implemented for the generation of random or refined slip distributions, has also been used by other researchers recently, e.g by Cattania et al. (2014) and Bach (2013).

3.1 Kinematic description of the rupture process

The source description is the first step needed to simulate ground motions. I chose a kinematic approach since the computation is much faster than for the dynamic equivalent. This also gives the possibility to perform multiple scenario simulations with different kinematic sources.

The input parameters needed for the description of the source are:

- moment magnitude M_w
- location of the hypocentre (latitude, longitude, depth)
- fault segments, each defined by its geometry (position and extension) and focal mechanism (strike, dip, rake)
- rupture velocity v_r

- distribution of slip along the fault

Those parameters are either known from the observation and inversion of teleseismic or geodetic measurements of the earthquake, if a past event is modelled, or have to be chosen from the possible range, if a scenario simulation is performed. For past earthquakes, the hypocentre, the moment magnitude and the overall focal mechanism are generally constrained quite well, depending on the size of the earthquake and the quality of seismic records. They can be available approximately 25 minutes after the origin time (Hayes et al., 2009). However the geometry of the fault segments, is more difficult to obtain. Usually this requires an inversion of seismic or geodetic data for the slip distribution (e. g. Ji et al., 2002), but there are also alternative methods. For example, Krüger and Ohrnberger (2005) use array methods for rupture tracking to obtain rupture length and velocity. Heimann (2010) inverts teleseismic data for source geometry, moment tensor and rupture velocity by introducing the eikonal source. The distribution of slip along the fault as well as variations of the rupture mechanism and velocity can either be chosen randomly, or can be obtained from the inversion of seismologic or geodetic data. The variety of data included in inversions is large, leading from field observations of fault scarps to strong ground motion time series and teleseismic data to GPS and InSAR measurements. However, one should keep in mind that different data sets and different inversion methods can lead to very different results for the same earthquake. For example there are at least six different slip models published for the Northridge, 1994 earthquake (Hudnut et al., 1996; Hartzell et al., 1996; Shen et al., 1996; Wald et al., 1996; Zeng and Anderson, 1996; Dreger, 1994), which show rather large disagreements for the distribution of slip.

To obtain correct seismograms even for high frequencies, the source has to be discretised fine enough. Heimann (2010) found that the main error for roughly discretised faults comes from the fact that the temporal shifts of the signal radiated by different parts of the fault patch are neglected during the simulation. In order to correctly model frequencies up to $f_{\max}$, the discretisation step Δx is given by

$$\Delta x = \frac{1}{2}\left(\frac{1}{v_r} + \frac{1}{v_{s_{\min}}}\right)^{-1} \frac{1}{f_{\max}}, \tag{3.1}$$

where v_{r} and $v_{s_{\min}}$ denote the rupture velocity and the minimum shear wave velocity along the fault. Basically, this means that the spatial discretisation has to be fine enough to avoid aliasing effects. Eqn. 3.1 is valid not only for the method presented here, but for any deterministic wave propagation approach which is based on the summation of discrete point sources. It should be stressed that the discretisation is independent of earthquake size, but mainly dependent on the considered frequency range. Indeed scientists are probably interested in higher frequencies in the case of smaller earthquakes and, therefore, a finer discretisation is needed. Assuming $v_{s_{\min}}$=3.0 km/s and $v_{\mathrm{r}} = 0.8 \cdot v_{s_{\min}}$, for a maximum frequency of 10 Hz the discretisation step should be 67 m. Obviously this discretisation is very fine and inversions of seismic or geodetic data are never able to resolve the kinematic

properties of the rupture process on such a small a scale. Depending on the size of the earthquake and the available data, slip is usually resolved for a discretisation of 1 to 10 km. To use a finer discretisation I refine the slip distributions such that a fractal slip distribution is obtained.

3.1.1 Small scale variabilities in the kinematic description

From the published slip distributions, it can be seen that coseismic slip is spatially variable at all scales. Mai and Beroza (2002) showed that the power spectrum of slip distributions obtained from inversion is well approximated by a power law decay. This means that slip can be characterised by a fractal distribution. They also found that the fractal dimension D is scale invariant. A fractal distribution with fractal dimension $D = 2$ is equivalent to the k-square model, where the slip amplitude u is dependent on the wavenumber k:

$$u(k) \propto \begin{cases} 1 & : k < 1/L \\ \left(\frac{1}{kL}\right)^2 & : k > 1/L. \end{cases} \tag{3.2}$$

L is a characteristic length which is related to the size of the earthquake. As was demonstrated by Herrero and Bernard (1994), the k-square model combined with a constant rupture velocity and a wavenumber dependent rise time, results in ground motions which follow the ω^{-2} decay for far-field displacements.

For the presented approach the k-square model is adopted in the high-wavenumber part of our slip distribution. For the low wavenumber part, the algorithm depends on the availability of a slip distribution inverted from the observed data. When a slip distribution for the earthquake of interest is already available, I keep its low wavenumber part and add the high-wavenumber part of a random distribution. If no slip distribution is available, the low-wavenumber part is also generated following the k-square model.

The generation of the slip model starts with the smoothing of the original slip distribution (Fig. 3.1). A 2D-Fourier Transform is performed to obtain the slip spectrum. In the wavenumber domain a 2D-Filter is applied, which has the form:

$$f_1(k) = \begin{cases} 1 & : |k| < k_{\mathrm{co}} - \Delta k_{\mathrm{co}} \\ 0 & : |k| > k_{\mathrm{co}} + \Delta k_{\mathrm{co}} \\ \frac{1}{2}\left(1 - \sin\left(\frac{\pi(|k| - k_{\mathrm{co}})}{2\Delta k_{\mathrm{co}}}\right)\right) & : \text{elsewhere} \end{cases} \tag{3.3}$$

k_{co} denotes the *combination wavenumber*, i. e. the wavenumber at which the original distribution is combined with the random distribution generated in the second step. To make sure that the main asperities are sufficiently visible, it is set to $k_{\mathrm{co}} = 1/(4 \cdot dx_{\mathrm{old}})$ with dx_{old} being the discretisation of the original slip distribution. Δk_{co} is a fraction of k_{co}, set to $\Delta k_{\mathrm{co}} = 0.8 k_{\mathrm{co}}$. The resulting slip field is smoothed, such that the edges of the former discretisation step are no longer visible (3.1b). Unfortunately this filter also introduces

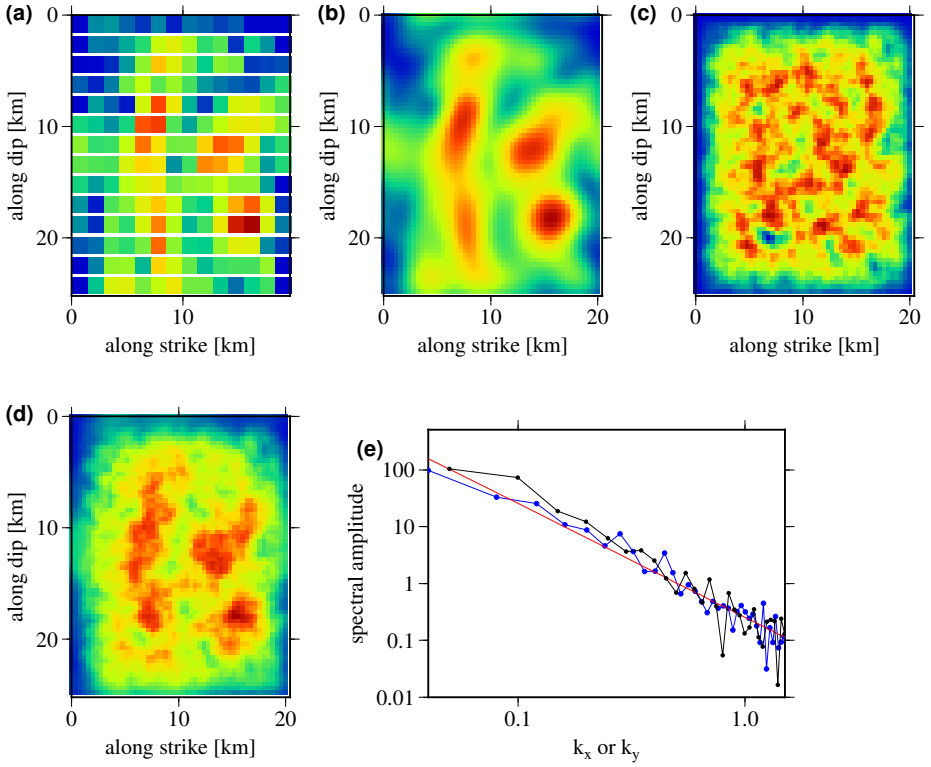

Figure 3.1: Example of a slip distribution generated with a wavenumber filtering approach and random phasing. Upper left **(a)**: A slip distribution obtained from inversion by Hartzell et al. (1996) for the Northridge 1994 earthquake. The discretisation step is 1.4 km × 1.8 km. Upper middle **(b)**: Smoothed slip distribution obtained by resampling and applying a smooth low pass filter. Upper right **(c)**: Random slip distribution obtained by generating a field with random phase but an amplitude spectrum proportional to the inverse wavenumber squared. Lower left **(d)**: Final slip distribution obtained by a combination of the two fields (b) and (c). Lower right **(e)**: Profiles of slip amplitude spectrum along k_x=0 (blue) and k_y=0 (black). The red line indicates a function proportional to k^{-2}.

periodicity in the resulting slip distribution. The effect is negligible if the original slip distribution has low values at its borders. However in case of surface ruptures there is often significant amount of slip at the upper edge of the slip distribution. The filter hence introduces high slip values at the lower edge. I correct this with a taper at the lower limit of the smoothed distribution if the upper fault edge is in a depth lower than 2 km.

Second, a random distribution is created. A random field of numbers with the same dimension as the original distribution is transformed to the Fourier domain. The spectral amplitude is then modified such that the k-square model is obtained:

$$u(k) \propto \begin{cases} 1/k_c^{\alpha} & : |k| < k_c \\ 1/|k|^{\alpha} & : |k| > k_c \end{cases} \tag{3.4}$$

with $u(k)$ being the spectral slip amplitude at wavenumber k, and k_c the corner wavenumber. Causse et al. (2010) established an empirical relation between the moment magnitude M_w and the corner wavenumber of the slip distribution based on 152 different distributions for 80 earthquakes. According to their results the along-strike corner wavenumber k_{cx} (in km) is linked to the moment magnitude by

$$k_{cx} = 10^{1.82-0.5M_w}.$$

Here, I assume that $k_c = k_{cx}$, neglecting that they found slightly different results for the along-dip corner wavenumber. For the slip distribution, the fractal dimension α equals 2.0; i. e., above the corner wavenumber we obtain a field, the amplitude of which decreases with the squared wavenumber, but has a random phase. Next, we apply a similar 2D-filter as for the original distribution, but as a high-pass:

$$f_2(k) = \begin{cases} 0 & : |k| < k_{\mathrm{co}} - \Delta k_{\mathrm{co}} \\ 1 & : |k| > k_{\mathrm{co}} + \Delta k_{\mathrm{co}} \\ \frac{1}{2}\left(1 + \sin\left(\frac{\pi(|k|-k_{\mathrm{co}})}{2\Delta k_{\mathrm{co}}}\right)\right) & : \text{elsewhere} \end{cases} \tag{3.5}$$

The inverse Fourier transform is applied to this filtered random field. Next, I add a constant to make sure that all slip along the fault is positive and then apply a taper, such that the slip decreases to zero towards the edges of the fault. The taper forms a plateau at the centre of the distribution and decays to 0 at the borders in form of a quarter cosine function as described by

$$t(x) = \begin{cases} \cos\left(\frac{\frac{\pi}{2}|(|x-L/2|-\eta L/2)|}{(1-\eta)L/2}\right) & : |x - L/2| \geq \eta L/2 \\ 1 & : |x - L/2| \leq \eta L/2 \end{cases} \tag{3.6}$$

This is similar to a Tukey-window but with a quarter cosine function instead of the half cosine function usually used. The parameter η defines the width of the taper and is chosen to be 0.5. The resulting random slip distribution has a k-square decay of amplitude in the

wavenumber domain, a random phase and decays to zero at the border of the distribution (Fig. 3.1c).

The smoothed original distribution is then added to the random distribution to obtain a final distribution (Fig. 3.1d). This final distribution contains the essential information from the inverted slip model in the low-wavenumber part and random components in the high-wavenumber part. Its Fourier amplitude spectrum still shows a k-square decay at high wavenumbers (Fig 3.1e).

3.1.2 Fault roughness

Another phenomenon observed at natural surfaces is fault roughness. Renard et al. (2013) and Candela et al. (2012) both investigated rupture surfaces and traces of surface ruptures and confirm that fault roughness is self-similar over a wide range of scales. They find a mean Hurst exponent of 0.8 for the investigated faults. Käser and Gallovič (2008) showed that fault roughness has a significant effect on ground motion, especially by increasing the complexity of the waveforms. They demonstrated that this does not only effect the high-frequency ground motion, but can influence the whole frequency band, depending on the receiver location. Following these findings, I introduce fault roughness in the kinematic description. However, in my model, there are no real deviations from the fault plane, but they are replaced by local variations in strike and dip. That means that the geometry variations are projected on the fault plane. Käser and Gallovič (2008) demonstrate that this procedure has similar effects on the simulated ground motions as true deviations from the plane.

These deviations are characterised by a distribution proportional to $k^{-\alpha}$ in Fourier space. α is the fractal dimension. The maximum offset of the deviation is $\beta \cdot L$ with L the shorter dimension of the fault plane and β the aspect ratio. In the following applications I use $\alpha = 1.8$ (corresponding to a Hurst exponent of $H = 0.8$ (Renard et al., 2013) with $\alpha = H + 1$) and $\beta = 0.02$. The choice of β is somewhat arbitrary. Candela et al. (2012) show that the factor defining the roughness amplitude is strongly variable for different earthquakes while the Hurst exponent is rather stable 0.8 ± 0.1. Presumably, the value of β is dependent on the maturity of the fault. It is a parameter which could be varied to perform different scenario simulations. Figure 3.2 shows an example of a rough fault plane which was calculated for the Northridge, 1994, earthquake.

Again, if information on the variation of the focal mechanism along the fault plane exist from data inversion, the low-wavenumber part of the distribution is kept and random high-wavenumber variations are added in the same way as for the slip.

3.1.3 Correlation between slip and rise time

The stress drop $\Delta\sigma$ is assumed to be the main factor influencing the ground acceleration. Since ground acceleration is connected to the acceleration along the fault via the repre-

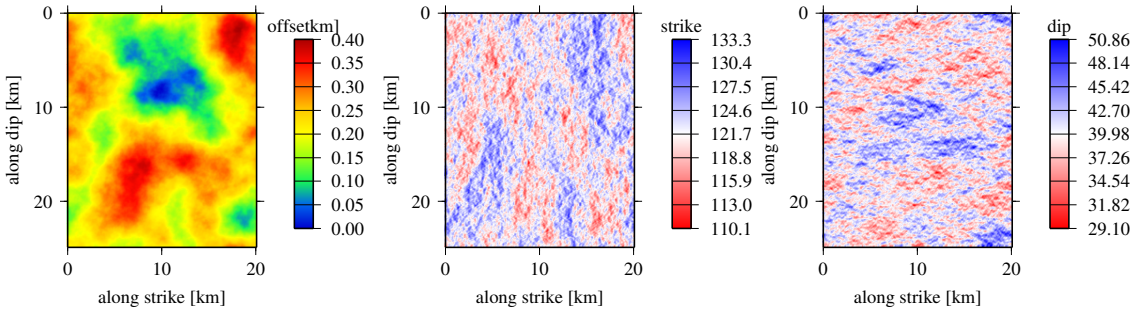

Figure 3.2: Example of projected deviations for a rough fault plane. **Left:** Offset of the deviation from the planar fault. The surface of the fault is fractal with a Hurst exponent of 0.8 and an aspect ratio of 0.02. **Middle:** Strike variations calculated for the rough fault. **Right:** Dip variations calculated for the rough fault.

sentation theorem, I assume that stress drop is proportional to the slip u divided by the squared rise time τ,

$$\ddot{u} \propto \Delta\sigma \propto \frac{u}{\tau^2}. \tag{3.7}$$

As a first order approximation I assume constant stress drop along the fault to constrain the relation between rise time and slip. In this case, the rise time of each fault patch τ_i should be related to the slip u_i along this patch by

$$\tau_i \propto \sqrt{\frac{u_i}{\Delta\sigma}} = \sqrt{\frac{u_i}{\text{const.}}}. \tag{3.8}$$

For this reason I make the patch rise time proportional to the square root of the patch slip. This is a compromise between the two end-members of constant rise time and constant slip velocity, where the rise time would be proportional to the patch slip. From dynamic rupture simulations, there is also evidence that patches of high rise time tend to experience high slip (Schmedes et al., 2010). This strongly positive correlation is reproduced by the relation between slip and rise time assumed here.

3.1.4 Determination of the rupture velocity

In my approach, the rupture velocity v_r is proportional to the S-velocity v_s of the earth model at the according fault depth with γ the proportionality factor to be fixed. Up to now the factor is chosen by best guess for each earthquake to approximately match the observed rupture velocity. If no information about the approximate rupture velocity is available, I will assume $\gamma = 0.8$, the mean value found from kinematic inversions (Somerville et al., 1999) and close to the median 0.85 found by Schmedes et al. (2010) from dynamic rupture simulations.

The rupture velocity, v_r, in the shallow depth is additionally reduced, but again related to the surrounding S-velocity v_s, with

$$v_r(z) = \begin{cases} 0.6 \cdot \gamma \cdot v_s & : z < 5\,\mathrm{km} \\ \gamma \cdot v_s & : z > 8\,\mathrm{km} \end{cases} \tag{3.9}$$

and a linear transition between 5 and 8 km. This definition of Eqn. (3.9) follows approximately the approach of Graves and Pitarka (2010) who argued that the reduction in velocity for the upper 5 km represents the shallow weak zone in surface rupturing events (Pitarka et al., 2009).

Another option would be to infer the rupture velocity from observations. However, I encountered the problem that often the mean rupture velocity is estimated for the whole fault area, only. If the fault spans over several depth layers of the earth model, this mean rupture velocity can be higher than the S-velocity. Therefore, one would introduce supershear effects in the simulations, which significantly change the resulting ground motions. For this reason I rejected this option and the examples shown in this work are all calculated with a rupture velocity proportional to the surrounding S-velocity. An example of a supershear rupture velocity simulation is given in section 4.2.1.

3.2 Rise time scaling to the radiated seismic energy

In this section I show how the energy magnitude can be used to calibrate the rise time of the modelled earthquake. Here, rise time is defined as the time when the slip rate function reaches its maximum or, in other words, the time between rupture initiation and the peak moment release rate. The purpose of this procedure is to make as few assumptions as possible and only to use parameters which can be obtained from the observation of the earthquake or which are empirically well constrained from former earthquake observations.

3.2.1 Joint consideration of energy and moment magnitude

For the simulation of an earthquake process the desired goal is the characterisation of the "source spectrum", i. e. the spectrum of the energy being transported by seismic waves. If far-field ground motion is corrected for attenuation and geometric spreading as well as site effects, the corrected ground motion spectrum can be considered as respresentative for this "source spectrum". From the observation of many earthquake spectra, it is known that the displacement spectra is characterised by a flat plateau at low frequencies and a decay proportional to the squared frequency for frequencies higher than the corner frequency (Fig. 3.3 a). For the simulation of ground motions caused by an earthquake, there is a need for observables which can describe the source spectra of this individual earthquake.

The most widely known and used parameter for the characterisation of an earthquake is the magnitude, which is a logarithmic measure of the energy released by an earthquake based on instrumental measurements. Historically, magnitude was determined from the

maximal amplitude of a velocity seismogram recorded at a certain distance from the epicentre after correction for attenuation and geometric spreading. However, the resulting magnitude is in this case strongly dependend on the position of the pass-band of the seismometer with respect to the corner-frequency of the source spectrum. This is due to the magnitude being related to the ground velocity spectrum which is maximal at the corner frequency, as shown in Figure 3.3 b. If the corner frequency does not fall into the pass-band of the seimometer, the strength of the earthquake is usually underestimated by the determined magnitude. The same applies to magnitude scales which rely on the same principle, like the surface wave magnitude M_S or the body wave magnitude m_b - taking advantage of different phases of the wavefield and their characteristics, but still measuring maximum amplitudes. The surface-wave magnitude measures the ground motion caused by Rayleigh-waves at a period of 20 s, and is therefore most suitable in the range $5 < M_S < 7$, as indicated in Figure 3.3 b. The body-wave magnitude is in practice determined from body-wave records of the WWSSN-short-period 1 s-seismometer. It is therefore most suitable for earthquakes with a corner frequency around 1 Hz, i. e. $2 < m_b < 5$ (Fig. 3.3 b). All of these magnitude scales face the problem that the maximal amplitude does not increase linearly for earthquakes stronger than a certain level. Therefore the scales tend to underestimate the strength of the earthquakes above this level and saturate at a certain magnitude.

The need for a non-saturating magnitude scale is met by the moment magnitude, which is an estimate on the seismic moment, i. e. the amount of slip occuring along a fault of a given size. Physically it is a measure of the irreversible inelastic deformation in the rupture area. Therefore, the moment magnitude is related to the final static displacement and an estimate of the tectonic consequences of an earthquake. It is determined from the low-frequency plateau of the source displacement spectrum shown in Figure 3.3 a. However, there is no temporal information in this parameter. Slow slip earthquakes may have a significant moment magnitude but rarely radiate seismic waves. Consequently, a second parameter is needed to characterise the earthquake.

The energy magnitude quantifies the amount of kinetic energy radiated by seismic waves. It follows more closely the original definition of a magnitude to measure the energy released by an earthquake and is, therefore, more suitable to estimate the seismic potential for damage. The energy magnitude is related to the radiated seismic energy, the energy which has been radiated from the source by seismic waves. To compute the radiated energy, squared velocity records are corrected for attenuation and integrated over time. Recalling that the ground displacement $u(t)$ depends on the moment rate $\dot{M}(t)$ (Aki and Richards, 2002), it is equally true that ground velocity is proportional to the time derivative of the moment rate function $\ddot{M}(t)$. Applying Parseval's theorem of the power of a signal in the time domain being equal to the power of it in the frequency domain, we can graphically illustrate the radiated seismic energy by the area under the far-field acceleration spectrum corrected for attenuation and geometric spreading. The size of this area is defined by the seismic moment, and two corner frequencies - the first

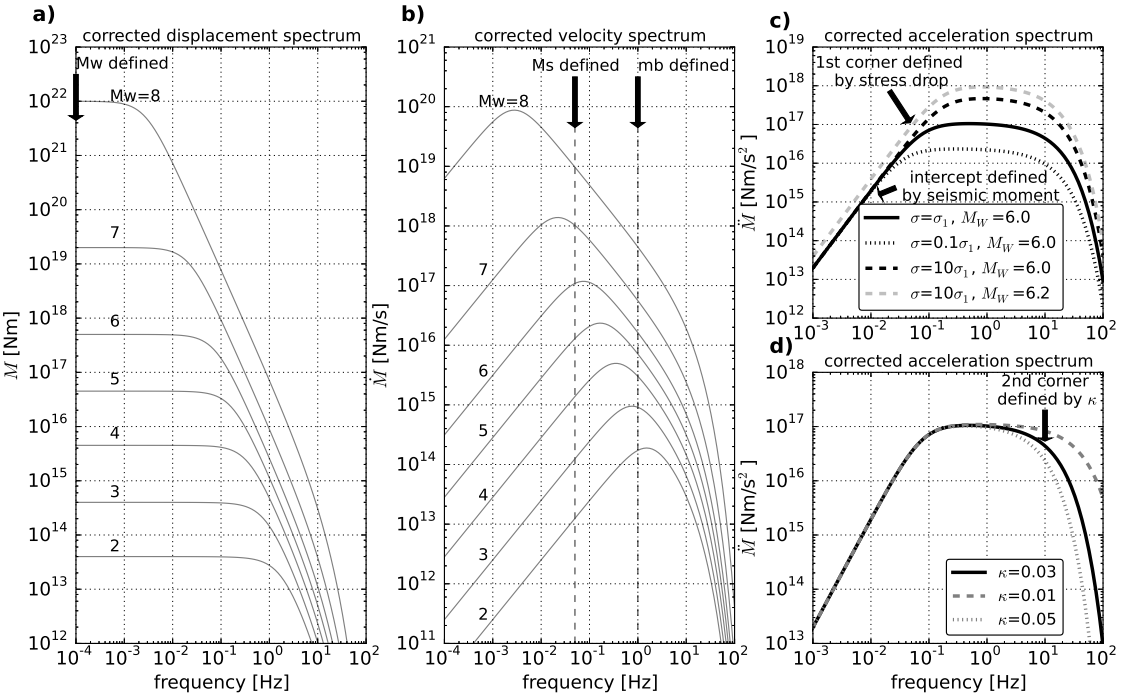

Figure 3.3: **(a)** Far-field displacement spectrum corrected for attenuation and geometric spreading and scaled to seismic moment, displayed for different moment magnitudes. The plateau towards the low frequencies of the spectrum is determined by the seismic moment and defines the moment magnitude. The transition from the plateau to the f^{-2}-decay occurs at the *corner frequency*, which is related to the size of the fault and the stress drop. **(b)** Corrected far-field velocity spectra scaled to seismic moment rate. Dashed lines at 1 Hz and 0.05 Hz indicated the frequencies at which body- and surface-wave magnitudes are defined, respectively. **(c)** Corrected far-field acceleration spectra scaled to the derivative of the seismic moment rate for a magnitude 6 earthquake (black line) and a magnitude 6.2 earthquake (grey dashed line). Dashed lines indicate earthquakes with stress drop 10 times higher than the stress drop σ_1 (arbitrary number as example) of the reference earthquake, dotted lines with stress drop 10 time lower than the reference earthquake. The area under the curve is related to the radiated seismic energy. **(d)** Same as (c) but for different values of high-frequency attenuation κ.

mainly defined by the stress drop, the second imposed by the high-frequency attenuation parameter κ. For a given level of seimic moment, a larger stress drop corresponds to an increased energy release and is visualized by a larger corner frequency and therefore increased area under the source acceleration spectrum in Figure 3.3 c. Similarly, a larger high-frequency attenuation parameter κ results in a smaller second corner frequency and would suggest a smaller amount of released seismic energy due to the decreased area under the acceleration spectrum as shown in Figure 3.3 d. That is why the usage of the energy magnitude as a source parameter is not entirely correct, as the high-frequency attenuation is supposed to be mainly a site and path-specific quantity. When integrating over the acceleration spectrum to obtain the energy magnitude, high κ values may lead to an underestimation of the energy. This is especially crucial for small earthquakes, where the amount of radiated energy is dominated by the high-freqeuncy part of the spectrum. As an improvement, seismic spectra could be corrected for the effects of κ before calculating the energy magnitude.

As the energy magnitude is integrating over a larger frequency range than body- or surface-wave magnitude, it is less effected by band-limited observation and suitable for a large magnitude range. On the other hand, from the energy magnitude as a stand-alone, it is not possible to distinguish between an increase in magnitude being caused by a increased level of seismic moment or by a high stress drop. For this reason, it has to be evaluated with regard to the moment magnitude in order to fully describe the source spectrum of radiated energy.

In practice the energy magnitude is determined by integrating the power spectrum of teleseismic waveforms (Di Giacomo et al., 2010). The waveforms have to be corrected for geometrical spreading and frequency dependent attenuation along the path from the source to the receiver. Dependent on the algorithm, waveforms are either corrected for the radiation pattern (e. g. Boatwright and Choy, 1986), or they have to be well distributed around the fault in order to average out the radiation pattern effects (e. g. Singh and Ordaz, 1994). The integration limits have to be chosen, such that, indeed, a major part of the wave-energy is integrated (e. g. Singh and Ordaz, 1994; Ide and Beroza, 2001).

Figure 3.4 shows the estimated values of M_w (determined by GCMT, Global Centroid-Moment-Tensor Project) and M_e (determined by GFZ, German Research Centre for Geosciences) for 990 events which where published by Di Giacomo (2010). The left figure shows the linear regression between these two magnitude measures. The linear relationship is given by $M_e = 0.95M_w + 0.38$ with the standard deviation of the energy magnitude of $\sigma_{M_e} = 0.237$. However, in general a direct relation is assumed. That is why in the right picture I also show the 1:1 line and calculated the standard deviation of M_e in this case, which amounts to $\sigma = 0.239$. As the difference in standard deviation is so small, the assumption that M_e is on average equal to M_w is justified. On the other hand the plot shows that for a single earthquake the energy magnitude can differ from the moment magnitude by up to 1 magnitude unit. The difference in energy magnitude is mainly caused by the different amount of stress drop during the earthquake. As mentioned before and

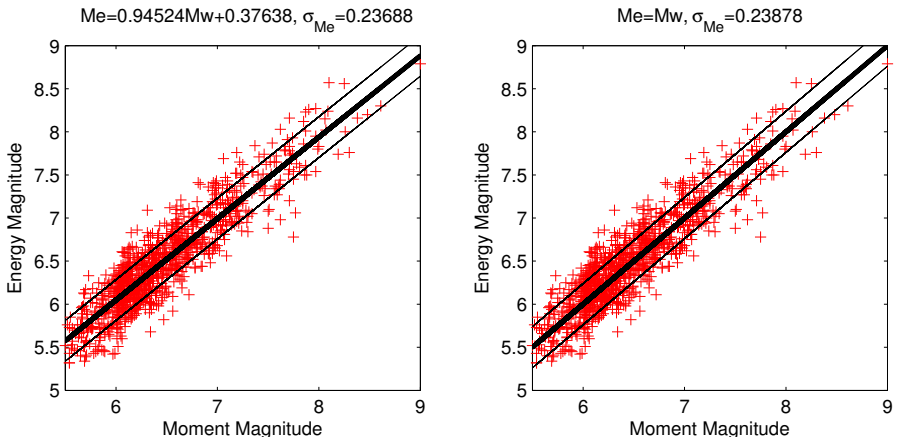

Figure 3.4: Relation between M_w (determined by GCMT, Global Centroid-Moment-Tensor Project) and M_e (determined by GFZ, German Research Centre for Geosciences) for 990 events. Data are obtained from Di Giacomo (2010). **Left:** The bold line shows the linear regression for the case $M_e = p_1 M_w + p_0$ with regression coefficients $p_1 = 0.95$ and $p_0 = 0.38$. The thin black lines indicate one standard deviation $\sigma = 0.237$. **Right:** The bold line shows the 1:1 line for $M_e = M_w$. The thin black lines show one standard deviation $\sigma = 0.239$ to the $M_e = M_w$ line.

illustrated in Figure 3.3 c, high stress drop causes an increased energy magnitude. This can also be seen from equation (30) in Bormann and Di Giacomo (2011), who combined various empirical relationships describing M_w and M_e:

$$M_e = M_w \left[\log\left(\Delta\sigma/2\mu\right) + 4.7\right]/1.5, \tag{3.10}$$

with $\Delta\sigma$ the stress drop and μ the average rigidity of the medium in the source area. Since the rigidity of the medium is not dependent on the earthquake parameters and therefore constant, one can see, that the two magnitudes are linked via the stress drop. Hence, the stress drop, which is an often used parameter in strong motion modelling, is fixed by given energy and moment magnitudes. An exception are slow slip or silent earthquakes, which can have a significant moment magnitude and may also release a considerable amount of stress, but rarely radiated any seismic waves. In this case, the energy magnitude cannot be related to the moment and the stress drop via Eqn. 3.10. However, M_e is probably more appropriate to calibrate the ground motion, as no or very low amplitude seismic waves will be radiated by a slow-slip earthquake and hence the associated energy magnitude is very small.

The clear advantage of the energy magnitude over the stress drop is that it can be measured. As said before, the energy magnitude is determined from observations of seismic waveforms. Its calculation can even be performed in near-real-time. In contrast, the stress drop occurring during an event cannot be measured but is generally fixed by an educated guess or by fitting the source spectrum with a Brune ω^{-2} model and using an empirical

relationship between moment, corner frequency and stress drop (Baltay et al., 2011). By using the energy magnitude, the calibration of the rise time is based on an observable parameter which indirectly also leads to a calibration of stress drop for the simulated earthquake.

To conclude, in order to describe an earthquake, the energy magnitude and the moment magnitude should be determined separately and considered jointly for the forward modelling and estimation of shaking.

3.2.2 Adjusting the radiated seismic energy

The observed energy E_{obs} is related to the energy magnitude M_e by the definition

$$E_{\text{obs}} = 10^{1.5 \cdot M_e + 4.4} \tag{3.11}$$

(Bormann et al., 2002). Using some basic formulae given by Haskell (1964) and following the derivation in Venkataraman and Kanamori (2004), the energy radiated from the modelled source E_{model} can be described via

$$E_{\text{model}} = \left(1 + \frac{2}{3}\frac{v_s^5}{v_p^5}\right) \frac{1}{10\pi\rho v_s^5} \int_0^\infty \ddot{M}^2(t)dt. \tag{3.12}$$

Here, v_p and v_s denote the P- and S-velocities, ρ the density, t is the time since the earthquake origin and $\dot{M}(t)$ is the moment release rate and is usually called source time function. Except for $\dot{M}(t)$ all parameters are determined by the earth model. Generally, E_{model} does not equal E_{obs} and thus we have to adjust the source time function. I am using Brune's source time function:

$$\dot{M}(t) = M_0 \frac{t}{\tau^2} e^{\frac{-t}{\tau}} H(t) \tag{3.13}$$

(Brune, 1970), with $H(t)$ the Heaviside function, M_0 the seismic moment, and τ the rise time, the time when the slip rate function reaches its maximum. Then, for a fault consisting of one single patch the following relation holds for the integral in Eqn. (3.12):

$$\int_0^\infty \ddot{M}^2(t)dt \propto \frac{M_0^2}{\tau^3}.$$

Since we assume that the seismic moment is also fixed by the observation, the only parameter to adjust the energy is the rise time. Finally, I scale the rise time by multiplying it with the third root of the ratio of modelled and observed energy,

$$\tau* = \tau \cdot \left(\frac{E_{\text{model}}}{E_{\text{obs}}}\right)^{\frac{1}{3}},$$

and recalculate the source time function with the modified rise time $\tau*$.

For a fault consisting of N_s patches, the radiated energy can be estimated via

$$E_{\text{obs}} \stackrel{!}{=} E_{\text{model}} = \int_0^\infty \left\{ \sum_i^{N_s} \sqrt{\left(1 + \frac{2}{3}\frac{v_{s_i}^5}{v_{p_i}^5}\right) \frac{1}{10\pi\rho_i v_{s_i}^5}} \frac{d}{dt} \left(M_i \frac{t - t_i}{\tau_i^2} e^{\frac{-(t-t_i)}{\tau_i}} H(t - t_i) \right) \right\}^2 dt. \tag{3.14}$$

with M_i and τ_i the seismic moment and the rise time of the ith patch, respectively. The scaled rise time τ_i^* is still determined in the same way as for a single patch, but it does not lead to an exact agreement between E_{obs} and E_{model}. Therefore, the procedure is applied iteratively. Adjusting the source time function in this way results in seismic energy radiation which is in agreement with the observed energy magnitude M_e. However, in the rare case in which the energy magnitude is significantly higher than the moment magnitude, it may be impossible for E_{model} to converge to E_{obs}. The approach would lead to decreasing rise times, and hence to increasing corner frequencies in order to achieve higher radiated energy. If the corner frequency is higher than the maximum modelled frequency, a further increase will not change E_{model} and agreement with E_{obs} may not be achieved. In my experience this never happened when using observed magnitudes but only in synthetic examples when energy magnitudes where chosen from a random distribution.

An alternative approach would be to scale the rupture velocity instead of the rise time. As the rupture velocity also determines the duration of seismic moment release, it directly influences the moment rate and can therefore be used to achieve a certain seismic energy given a fixed seismic moment. However the rupture velocity also influences the signal length, while scaling the rise time keeps the signal length approximately constant. Furthermore, the mean rupture velocity is easier to determine from the data (e. g. from the signal duration of teleseismic records) than the patch rise time. These are the reasons why, in this study, I fix the rupture velocity and constrain the rise time by the energy magnitude.

3.3 Calculation of Green's functions

The wave propagation used in the presented approach is purely deterministic. The software for Green's functions calculation is QSGRN by Rongjiang Wang. A layered earth model without horizontal heterogeneities is used. Each layer is characterised by its P- and S-velocity, v_p and v_s, the material density ρ and the quality factors Q_p and Q_s, which determine the attenuation of seismic waves. The synthetic Green's functions are calculated using an ortho-normalising propagator algorithm. It is based on the Thomson-Haskell propagator algorithm, which calculates the displacement vector in the frequency-wavenumber domain from layer to layer via chain rule. A simple matrix operation accounts for the numeric instabilities which occur in the Thomson-Haskell procedure when the waves become evanescent. An additional procedure in the propagation loop makes all fundamental vectors in situ orthonormal and thereby avoids an otherwise occurring loss-of-precision problem. Details of the calculation are described by Wang (1999). The

algorithm delivers full solutions with correct phase arrivals and is applicable to the whole frequency range, including the static deformation. The user has to provide the distance range as well as the depth range of seismic sources of which Green's functions are to be calculated. Additionally it requires some parameters considering time and space sampling.

This is the most time-consuming part of the calculation. However, for given velocity model and source-receiver distances, the Green's functions have to be calculated only once. They can be saved in a Green's functions database and may be accessed for different scenario calculations. This is also the big advantage of 1D-Green's functions over 3D-Green's functions: in a 3D-scenario the Green's functions are also dependent on the lateral position of the fault. Therefore, one needs much more computation time and storage to establish the full Green's function database. To my knowledge, this has not been done yet, but Green's functions are calculated for a specific fault only and have to be recalculated for each fault. In a 1D-scenario the Green's functions are independent of the lateral position of the fault. One only has to make sure that all needed the source-receiver distances are calculated.

There are a number of parameters influencing the results. In order to minimise the effects of signals from the end of the Green's function which reappear at the beginning of the time window, an aliasing suppression factor may be specified. This factor damps signals at the end of the time window such that their contribution at the start of the time window is reduced. To reduce the influence of numerical artefacts on the simulation the correct seismogram length for a given source-receiver distance should be estimated. The Green's function are padded with zeros after this time to avoid artefacts at the end of the Green's function. A demonstration of the influence of these two effects is given in Appendix A. For very large distances, a flat-earth-transformation may be applied, to account for the increasing effect of the surface curvature. However, for the distances shown in this work, no earth-flattening was used.

3.4 Convolution and superposition

In the last step, the seismograms have to be computed. For each receiver, the moment rate functions of all patches of the kinematic source are convolved with their corresponding Green's functions and the waveforms of all patches are summed up for each receiver. The software for the convolution and superposition is named QSCMP. The code was developed initially by Rongjiang Wang and improvements were added during the course of this PhD work. These include the approximation of moment rate functions for extended patches and the implementation of the observed high-frequency attenuation.

3.4.1 Approximation of finite patch moment rate functions and convolution

Te most simple technique for the convolution would be to convolve the moment rate function of each small fault subpatch with its Green's function. However, due to the

high number of fault subpatches needed to avoid spatial aliasing, the huge number of convolutions led to a very high computation time. To avoid this, the fault subpatches are binned in larger fault patches and moment rate functions for those extended patches are determined. The moment rate function of each of the resulting fault patches is convolved with the respective Green's function, thus giving rise to a decrease in the number of required convolutions.

The moment rate function is calculated for each subpatch-receiver pair and the functions of all subpatches binned in one fault patch are summed with their according time shift related to their rupture time and their relative position with respect to the receiver. It is important to note that the shape of the resulting moment rate function of the large patch depends on the receiver position. This dependence makes the important difference between a simple coarse discretisation and the refined discretisation used here.

An example using different discretisations for the Green's function grid and the source is given in section 3.5, and the limitations are shown.

3.4.2 Implementation of observed high-frequency attenuation

From observations it is known that at high frequencies seismic waves are attenuated in a way which is not explainable with the simple attenuation implemented in the velocity model. This effect at high frequencies is nowadays most often accounted for by a site specific attenuation model with parameter κ. Van Houtte et al. (2011) investigated κ at Japanese stations where seismic sensors are co-located at the surface and in a borehole. They found that surface-κ is higher than borehole-κ (in their study approximately twice as high), showing that a significant part of κ originates from the shallow station subsurface. However the borehole-κ was still significant, which suggests that part of the κ value arises from deeper than the borehole sensor. The study also finds a significant source contribution to κ as well as a moderate distance dependence. It seems likely that κ is an effect arising from the station subsurface. Different κ values for multiple records at the same seismic station may be caused by the heterogeneities surrounding the station location and, hence, an azimuthal variance of the effects determining the amplitude of κ.

To summarise, it is not yet clear whether κ is a local effect and even less what its physical causes are. Consequently it is implemented in ground motion modelling suing an empirical functional form: an exponential fall-off of the amplitude spectrum. Therefore, the Fourier spectrum is multiplied by $e^{-\pi\kappa f}$. If a mean station-κ is known from preceding observations, one would use this as the best value for the simulation.

3.4.3 Superposition

Finally, the contributions of all patches are superposed, which results in the time series of ground velocity at the receiver. To obtain ground acceleration and ground displacement, the derivatives and integrals of the seismograms are calculated in the time domain, respectively. For an overview, I have summarised all input parameters of the simulations in

Earth model (layered half-space)	v_{p_i}, v_{s_i}	P- and S-wave velocity
	ρ_i	density
	Q_{p_i}, Q_{s_i}	Quality factors
	for $i = 1, \dots N$	for N different layers
	κ	regional κ value
Source model	M_0	moment magnitude
	M_e	energy magnitude
	$\vec{x}_h$	hypocentre
	v_r	rupture velocity
	L, W	fault length and width
	ϕ, λ, δ	strike, rake, dip
	d_i $(i = 1, \dots N_s)$	slip distribution for N_s patches

Table 3.1: Summary of all input parameters used in the simulations.

Table 3.1. All the examples shown are calculated on a desktop PC with a CPU running at 3.4 GHz and 8 GB RAM. The computation of the large earthquakes (see Secs. 4.1 and 4.2) took approximately one day, the smaller earthquake (see Sec. 4.3) roughly one hour, and the very small synthetic example (see Sec. 3.5) 7 minutes.

3.5 Code validation

3.5.1 Comparison to a wave propagation simulation using a finite element scheme – A layer over a halfspace

In order to make sure that the algorithm for determining the Green's functions and calculating the convolutions and superpositions is correct, I compare the results of our approach to the results of Käser and Gallovič (2008) who apply a Discontinuous Galerkin scheme using Arbitrary high order DERivatives (ADER-DG). This method, which is based on a Finite Element scheme, was proven to be highly accurate (de la Puente et al., 2007; Käser and Dumbser, 2006). I calculate seismograms for a Layer-Over-Halfspace problem (LOH.2) as proposed by Day (2001). The model setup is specified in Figure 3.5. The source with homogeneous slip strikes and dips 90° . Right-lateral slip occurs with a constant rupture speed of v_r=3 km/s. The seismic moment is $1.04 \cdot 10^{18}$ Nm.

For comparison I show here 4 seismograms and spectra at the stations shown in Figure 3.6 a. Figure 3.7 shows the seismograms calculated with QSGRN/QSCMP with exactly the same settings as the simulation in the work of Käser and Gallovič (2008). In this first case I calculated Green's functions with a grid spacing of 0.067 km. The extended fault was discretised in the same way and the rise time was set manually to $\tau = 0.01$ s. The figure compares velocity seismograms as well as velocity spectra calculated with the two different simulation approaches. The resulting waveforms are very similar. The differ-

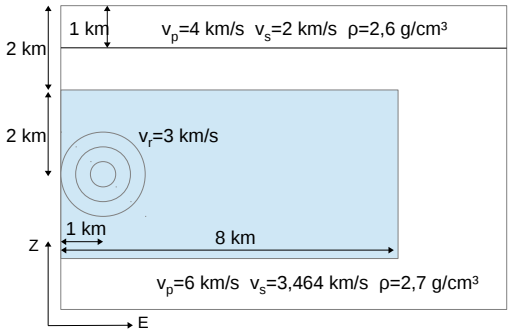

Figure 3.5: Model setup for the LOH2-Test case. The station positions relative to the westernmost edge are given in Fig. 3.6.

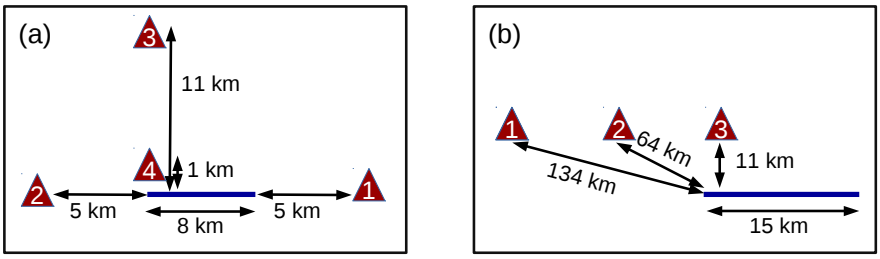

Figure 3.6: Relative position of the stations discussed **a)** in Section 3.5.1 and **b)** in Section 3.5.2. Station numbers refer to **a)** the numbers in Table 3.2 as well as Fig. 3.7 and **b)** to the station numbers in Figure 3.9.

ences between the two simulations are almost not visible in the time-domain. The Fourier spectra show minor differences for all stations.

To compare them quantitatively, I used the relative seismogram misfit energy, defined as

$$E = \sum_{j=1}^{n} (s_j^{\text{QSCMP}} - s_j^{\text{ADER-DG}})^2 / \sum_{j=1}^{n} (s_j^{\text{ADER-DG}})^2, \tag{3.15}$$

with the number of samples n=299, s_j^{QSCMP} the jth sample of the QSCMP-seismogram and $s_j^{\text{ADER-DG}}$ the jth sample of the ADER-DG-seismogram. For the comparison the seismograms were low-pass filtered at 5 Hz and resampled with 20 Hz. The seismogram misfit energy is given in Table 3.2. The values are close to zero, meaning a fairly good agreement between the seismograms modelled with the two different approaches.

The same procedure was performed for a Green's function spacing of 1 km, with the fault itself still being discretised in 0.067 km subpatches. As described in Section 3.4 the subpatches are binned in patches with the same spacing as the Green's functions and moment rate functions are calculated for these large patches depending on the receiver position. Figure 3.8 shows the simulation results for this setting. Some differences are

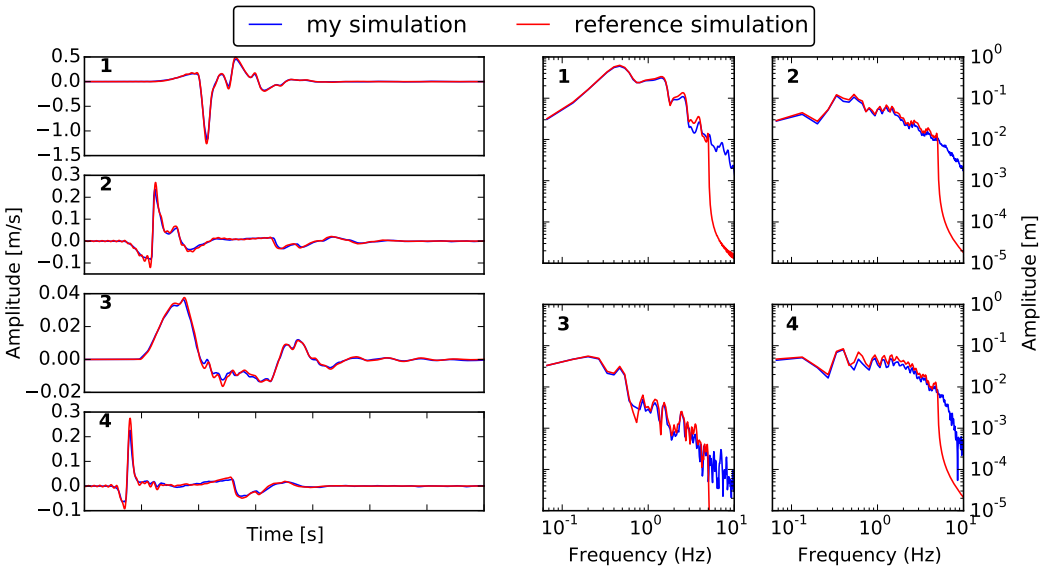

Figure 3.7: Velocity seismograms (left) and spectra (right) for the LOH-2 test case at the four stations specified in Table 3.2. The method proposed in this thesis is shown in blue, the reference method (ADER-DG) in red. Seismograms of the reference simulation were low-pass filtered with a corner-frequency at 5 Hz, hence the mismatch at higher frequencies.

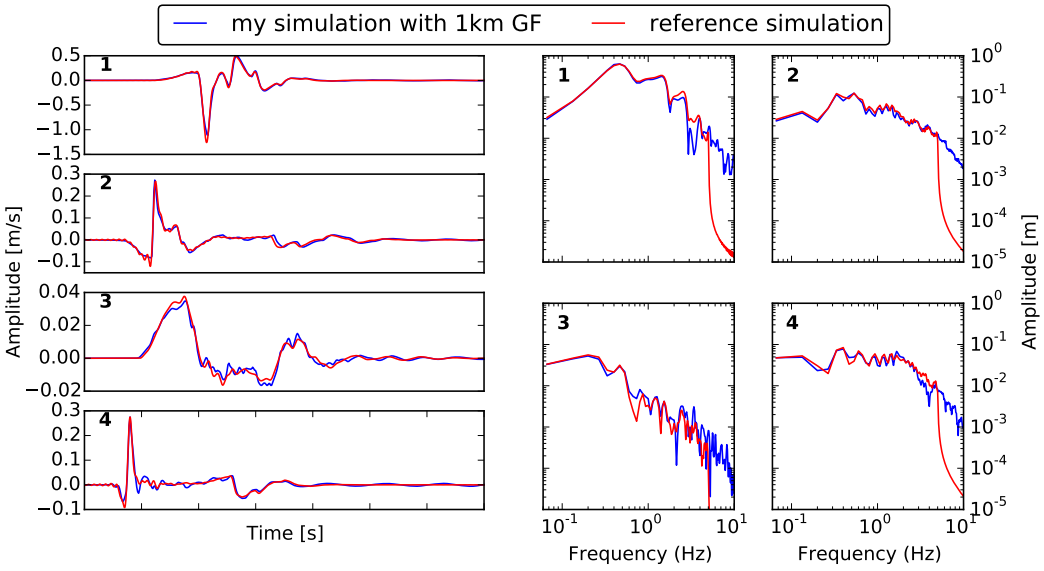

Figure 3.8: Same a Fig. 3.7, but for a Green's function spacing of 1 km used for the method proposed in this thesis.

station	misfit energy	
	0.07 km	1 km
1	0.1067	0.148
2	0.0068	0.026
3	0.0320	0.045
4	0.0098	0.023

Table 3.2: The relative misfit energy of the seismograms with 0.07 km and 1 km Green's functions spacing compared to the ADER-DG approach for the four considered stations.

now visible, especially for the stations in the backward direction. Deviations from the simulation with the fine Green's function spacing are due to the fact that the Green's functions belonging to the two different edges of a patch are only shifted in time, but should be stretched in reality. Additionally the time shift is calculated for the S-wave velocity, while a different time shift for P-waves would be appropriate. Comparing the seismogram misfit energy, the values are also increased. Still, the major features of the waveforms are sufficiently well reproduced, such that in this case the use of 1 km spaced Green's functions is acceptable.

3.5.2 Inaccuracy arising from insufficient discretisation – A fault in a layered halfspace

Unfortunately the approach is only truly valid for the case of the fault being placed in a halfspace with some overlying layers. If one or multiple interfaces are placed underneath the fault, which is definitely the case in nature, before the convolution a different time shift would have to be applied to downgoing and upgoing waves. The take-off angle is different for waves reflected at an underlying layer. Hence, each reflected wave would require a different time shift.

I tested the influence of the discretisation effect on the simulated ground motion with a simple fault of 15 km length and 1 km width placed in a layered earth model. The adopted earth model is the one used for the simulation of the 1994 Northridge earthquake in Section 4.3 and is specified in Table 4.3. The east-west striking fault dips 90° and right-lateral slip occurs with a constant rupture speed of v_r=2.3 km/s. The fault is placed in 4 km depth, such that several velocity interfaces are placed underneath the fault. Seismic receivers are positioned along a line running parallel to the fault with an offset of 11 km to the north.

Figure 3.9 shows the simulation result at 3 stations of 3 different discretisation settings compared to a reference simulation with fine discretisation. The stations are placed in 134, 64 and 11 km distance from the surface projection of the fault and their positions relative to the fault are shown in Figure 3.6 b. The reference simulation was performed with a Green's function spacing of 60 m and a source discretisation of 60 m. Hence, it should give correct results up to a maximum frequency of 10 Hz (Eqn. 3.1). For each

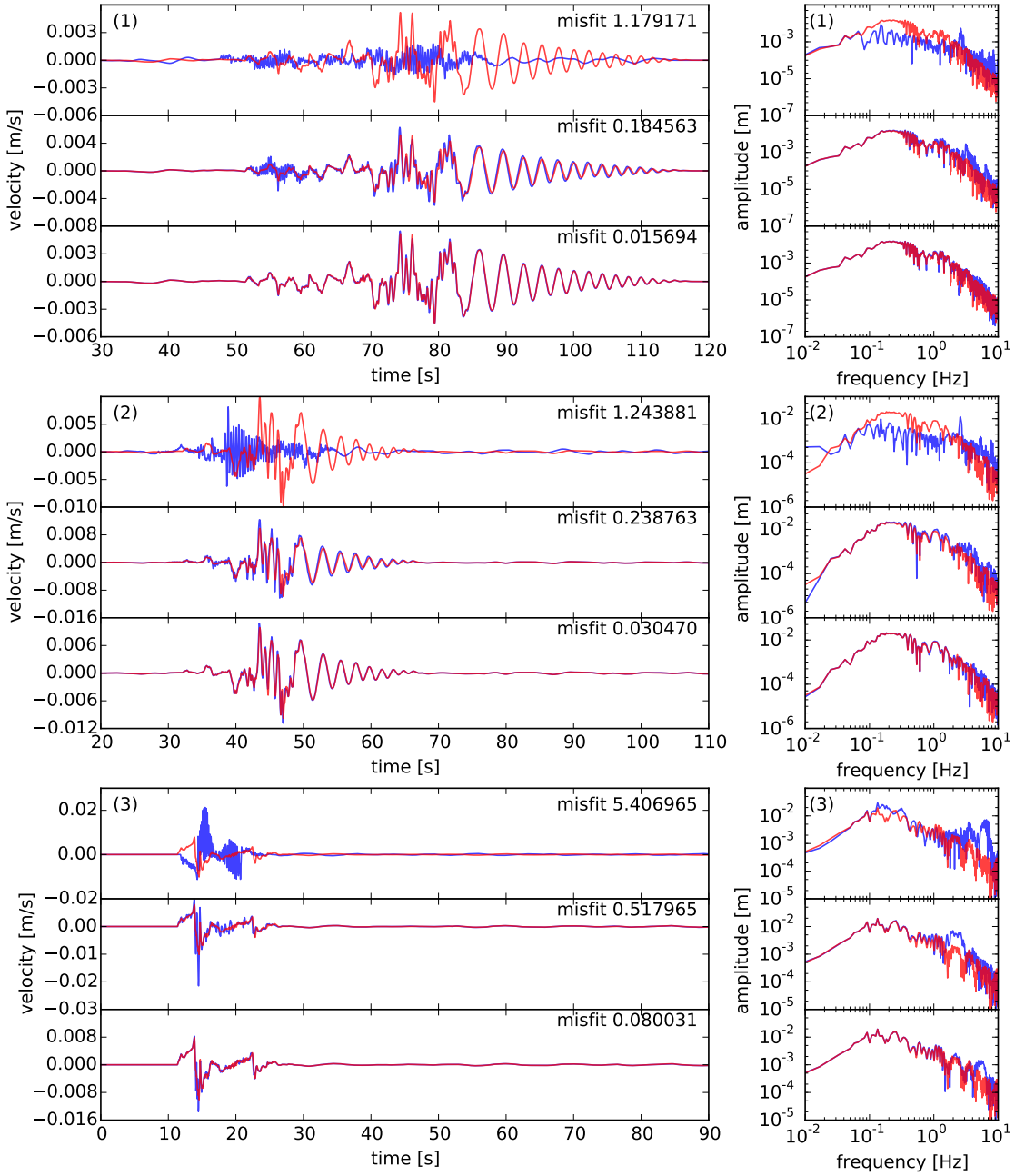

Figure 3.9: Velocity seismograms (left) and spectra (right) of the north-component for the layered test case at the three stations placed at 134, 64 and 11 km distance from the fault (from top to bottom). The red trace shows the reference simulation with a Green's function spacing of 60 m and a source discretisation of 60 m. For each station, I show three different simulations in comparison to this: At the top, a simulation with a Green's functions spacing of 1 km and a source discretisation of 1 km. In the centre, the Green's function spacing is 1 km and the source discretisation 60 m. At the bottom, the Green's function spacing is 200 m and the source discretisation 60 m. The misfit value given in the top right corner of the seismograms specifies the misfit energy calculated by means of Eqn. 3.15.

station I show at the top the simulation with a Green's function spacing of 1 km and a source discretisation of 1 km. The resulting waveforms are significantly different from the reference simulation. The aliasing effects resulting from the insufficient discretisation are entirely masking the true waveform. Also, the velocity spectrum is deformed and does not agree with the spectrum of the reference simulation. The centre plot shows the results using a Green's function spacing of 1 km but a source discretisation of 60 m and receiver dependent finite patch moment rate functions. The waveforms are now much closer to the reference simulation, the low-frequent signal and the general form of the velocity spectrum are reproduced. However, peak ground velocity (PGV) is only matched at the far-field stations. For the station close to the fault, PGV is overestimated by a factor of 2. At the far-field station there are artefacts at the beginning of the seismogram, which can be explained mainly by the correction of the time shift being made with the S-velocity instead of the P-velocity. These artefacts are not visible at the near-field station and less clearly visible when considering stations in forward direction, which are not shown here. Finally, a simulation was performed with a Green's function spacing of 200m and a source discretisation of 60m. In this case, the agreement with the reference simulation is satisfying. The artefacts at the signal onset of the far-field stations are removed. Still, PGV is overestimated at the near-field station. For each of the simulations I calculated the misfit with respect to the reference simulation and display it in the top right corner of the plot. The fine source discretisation combined with the coarse Green's function spacing leads to a misfit energy which is ten times smaller than for the coarse source discretisation. A Green's function spacing of 200 m again reduces the misfit energy by a factor 6.

This test demonstrates that only a fine Green's function spacing results in correct waveforms at high-frequency. However, the approximation of finite patch moment rate functions also provides realistic waveforms with nearly correct frequency content and phasing. In contrast, simulated peak values should be regarded with caution at near-field stations, as this approximation might introduce spurious spikes in the waveforms. On the other hand, it leads to a significant reduction of the computation time as Green's functions have to be calculated on fewer points and a smaller number of convolutions has to be performed.

3.6 Discussion

In this section I presented a ground motion modelling technique which combines a kinematic source description with a deterministic, semi-analytical wave propagation based on a layered velocity model. This method has the advantage of being computationally easy to manage. The generation of different source models can be achieved by either varying some of the less well constrained parameters such as the rupture velocity (or the respective proportionality factor γ) or the roughness of the fault, or by performing multiple simulations with the same parameter set, but different realisations of the random fields. Pre-computed Green's functions can easily be used to investigate different source scenarios.

The main criticism of kinematic source descriptions is that they enforce correlations between different parameters which may result in scenarios that are not physical. I tried to overcome this issue by introducing some constraints on the simulated parameters such as the fractal distribution of slip, the relation between slip and rise time and the mimicked fault roughness. However, it would be desirable to include limits to certain values or cross-correlations of parameters in future simulations. For example Song and Somerville (2010) investigated 2D spatial coherence patterns between fault slip and rupture velocity and fault slip and slip velocity for some source models obtained from dynamic rupture simulation and a number of kinematic source models obtained from inversion of seismic data. They found that high slip velocities usually occur in regions of high slip. In contrast, they observed that the correlation maximum between slip and rupture velocity is often shifted in forward rupture direction. However, those findings are still based on limited numbers of source models and there is no clear definition on how much the correlation maximum is shifted for a certain slip value. For the source descriptions from dynamic modelling it would also be necessary to test several assumptions on the distribution of stress along the fault and several frictional parameterisations. Once more mature studies on those cross-correlations are finished, it would be desirable to include those in the description of the kinematic source model.

Further investigations of dynamic simulations or observed source characteristics should also be considered for the moment-rate function. Guatteri et al. (2003) point out that the complexity of the moment-rate function obtained from dynamic simulations strongly influences the waveforms and frequency content at near-fault stations. This also highlights a specific drawback of the presented method: the form of the moment-rate function is identical for each subpatch, only rise time and maximal amplitude are variable. So far, I did not implement any features that account for the fact that in dynamic simulations the moment-rate functions tend to be more elongated close to the hypocentre and shorten towards the edges of the fault (Guatteri et al. (2003)). Also, each patch is allowed to rupture only once. Therefore, slip reactivation or similar effects are not included.

The adoption of constant stress drop and the derived relation between slip and rise time can only be a first approximation. Indeed, for large earthquakes stress drop along the fault may be highly variable and the assumption made would be too simplistic.

Finally, the scenarios with supershear rupture velocity require additional consideration. As of now, supershear velocities are excluded, as the proportionality factor γ between rupture velocity and S-velocity is constrained to be smaller than 1. However, supershear rupture velocities have been observed and could be reproduced in dynamic simulations. For a complete investigation of possible rupture scenarios, the possibility of supershear should be considered.

The usage of the energy magnitude as a parameter to fix the amount of energy radiated from the source at high frequencies provides a mean to calibrate the source spectrum by another observable quantity. Unfortunately, the site-specific parameters such as κ or path-specific anomalies in the attenuation function may influence the determined energy

magnitude, such that it may not reflect the actual seismic energy radiated from the source. This may especially influence results at low magnitudes, where most of the energy is radiated at high frequencies. On the other hand, if station specific characteristics are well known, one could apply corrections to the recorded seismograms before calculating energy magnitudes in the future. For example, Di Giacomo et al. (2011) determined inter- and intra-station errors for M_e. They were able to show that path specific residuals occur for particular earthquake regions at a single station. By doing this on a global scale, one could develop site- and path-dependent corrections for the determined energy magnitudes.

Regarding the wave propagation, I could demonstrate that the presented approach results in very similar seismograms compared to the ADER-DG scheme of Käser and Gallovič (2008). However, coarse Green's function grids may only be applied with caution, as they can lead to overestimated peak ground velocity at near-fault stations and some high-frequency noise in the P-wave-part of the seismogram. As approximations with coarse Green's function spacing nevertheless provide a good representation of the general form of the seismogram and spectrum, and the computation time is largely reduced, several examples in the following section make use of this simplification.

Chapter 4

Application

The comparison of modelling results to observed records from past earthquakes provides the possibility to check to what extent the simulations can reproduce the natural waveforms. In this chapter I will show the application of the introduced modelling approach to three past earthquakes in order to demonstrate the performance of the method. I present applications of the methodology for the cases of the 2008 Wenchuan, the 2003 Tokachi-Oki, and the 1994 Northridge earthquake. I also show how the scaling of the rise time is performing under changes of the rupture velocity for the 2008 Wenchuan earthquake. Making use of the example of the Tokachi-Oki earthquake, I demonstrate that simulations with constant rupture speed along the fault may lead to unreasonable estimations of ground motion. Finally I show the influence of a very thin low-velocity layer for the example of the Northridge earthquake. Additionally I compare a simulation making use of a 1D-velocity model to results from a simulation with a 3D-velocity model but the same kinematic source description by Graves and Pitarka (2010).

Simulations of the 2008 Wenchuan earthquake and the 2003 Tokachi earthquake have been published in Kieling et al. (2014). However, here, I additionally implement the high-frequency site attenuation with parameter κ.

4.1 Application to the 2008 Wenchuan earthquake

On 12 May 2008, the $M_w = 7.9$ Wenchuan earthquake occurred in the region of Sichuan in China (Fig. 4.1). The rupture extended about 300 km along the Longmen Shan thrust belt and was one of the most devastating intraplate thrust earthquakes. Just before the earthquake, the installation of the National Strong Motion Observation Network System (NSMONS) of China was completed (Li et al., 2008) and ensured many near-field observations of the event. This allows for the comparison of the observed strong motion records at 95 stations shown in Fig. 4.1 with the corresponding time series obtained by my simulation.

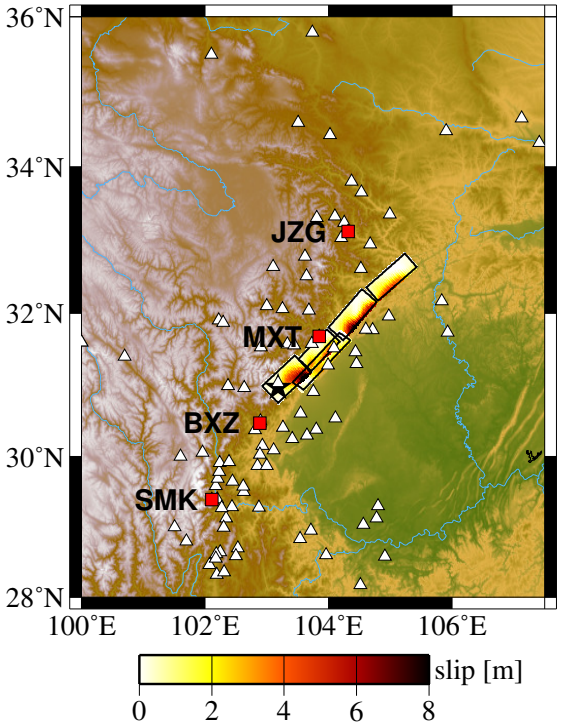

Figure 4.1: Map view of the 2008 Wenchuan earthquake. Triangles indicate the strong motion stations. Stations to which simulations are compared in Fig. 4.2 are marked by filled squares. The black star marks the hypocentre.

Green's functions were calculated on a grid of approximately 1 km for the layered velocity model given in Table 4.1, which is similar to the IASP91 model (Kennett, 1991) but accounts for slightly smaller S-velocities in the upper crust as suggested by Xu et al. (2010b). I use the source geometry and slip model obtained by Xu et al. (2010a) from joint inversion of GPS and InSAR coseismic displacement. Their model consists of 5 fault segments, which are further discretised to patches of 1.5 km size. The dip of the segments at depth is smaller than the dip close to the surface. From field observations Liu-Zeng et al. (2009) found that two parallel faults, the Beichuan fault and the Pengguan fault were active during the earthquake, which is consistently included in the slip model. According to the model of Xu et al. (2010a), high slip mainly occurred close to the surface with the maximum slip on the southernmost fault segment, close to the hypocentre. The moment magnitude of 7.9 provided by Global CMT solution (see www.globalcmt.org) corresponds to a seismic moment of $0.9 \cdot 10^{21}$ Nm. The source model is rediscretised to 100 m, leading to a maximum frequency of around 7.5 Hz. The simulated and observed seismograms shown in the following are lowpass-filtered at 7.5 Hz because of this frequency limit. In this example the energy magnitude of 7.9 (USGS) equals the moment magnitude and leads to a mean subpatch rise time of 0.022 s. According to my definition (Eq. 3.13, the rise time

depth(km)	v_p(km/s)	v_s(km/s)	density(g/cm^3)
0.0 - 5.1	5.50	3.20	2.6
5.1 - 18.0	6.00	3.46	2.7
18.0 - 34.5	6.70	3.87	2.8
34.5 - 40.0	7.50	4.33	3.0
$>$ 40.0	8.04	4.47	3.4

Table 4.1: Crustal velocity model used for the calculation of the Green's function for the 2008 Wenchuan earthquake. Here, a constant Q_S factor of 600 was used.

being the time from the slip onset till the moment rate reaches its maximum) , 36% of the energy are radiated over this period. For a 90% energy release, which is an alternative definition of the rise time, this value has to be multiplied by 2.4. The rupture velocity is related to the S-velocity by Eqn. (3.9) with γ=0.8, which in combination with the used velocity model results in a rupture speed of 2.8 km/s for most of the fault as found by the inversion of teleseismic data by Wen et al. (2012). Sun et al. (2013) report κ-values of 54 seismic receivers for all three components for the data obtained during the Wenchuan earthquake. I averaged their values over all stations and components and found a mean of 0.017, which is applied in the subsequent simulation.

In the following the results of the simulation are compared to the observed waveforms, PGA, spectral acceleration at 1 Hz, and response spectra. PGA and spectral acceleration at different frequencies are often used as measures for engineering purposes. Furthermore they are usually used in empirical studies, so they are appropriate to compare the outcomes of the presented approach to empirical relationships. PGA is proportional to the integral over the Fourier spectrum of the signal and, therefore, also sensible to the high-frequency components of the ground motion. Spectral acceleration at 1 Hz is less sensitive to the higher-frequency components of the shaking and describes the likely response of buildings with multiple stories.

Figure 4.2 shows modelled and observed waveforms at 4 selected stations at different distances from the fault. The example shows that observed and simulated seismograms exhibit similar characteristics in terms of amplitude and signal duration at the near-fault stations (MXT and BXZ), even though peak accelerations and the east-west component are somewhat overestimated. This is improved at the remote stations (JZG and SMK), where the simulated peak ground acceleration (PGA) approximately agrees with the observed one, although amplitudes are still overestimated when considering only the low-frequent part of the ground motion. The simulated signal duration is too short at the very distant station SMK. This is probably due to the scattering by material heterogeneities, which is not accounted for by the presented method. Figure 4.3 shows the observed average horizontal PGA compared with the predicted values. Here, average horizontal means the geometric mean of the peak values of the individual components. The maps of PGA show

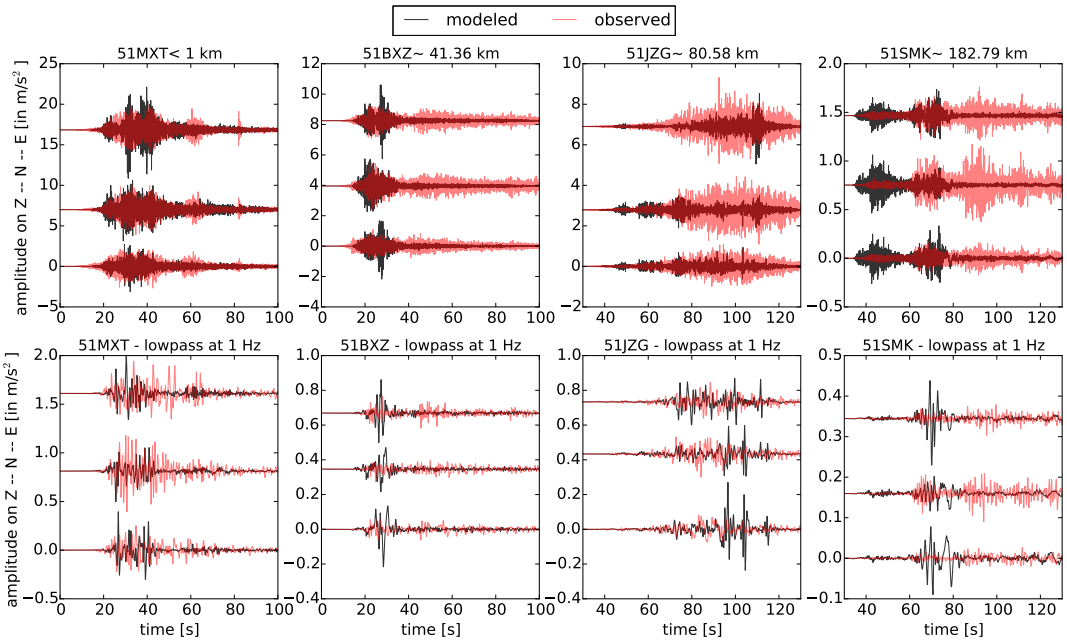

Figure 4.2: Comparison of recorded (red) and simulated (black) three-component ground-velocity waveforms at three selected sites for the Wenchuan earthquake. **Top:** Broadband ground velocity waveforms. The title gives the station name and closest distance to the surface projection of the fault. **Bottom:** Waveforms low-pass filtered at 1 Hz. Station locations are indicated in Fig. 4.1.

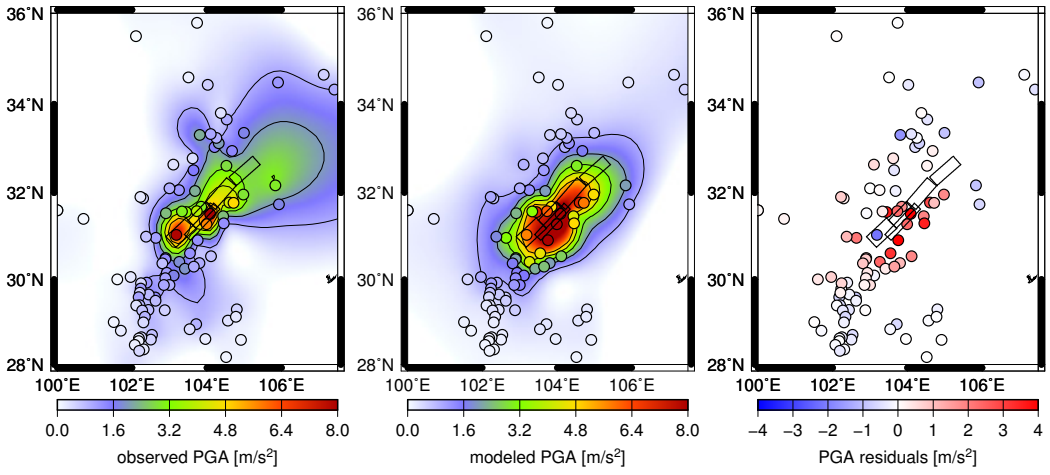

Figure 4.3: Comparison of interpolated observed (left) and modelled (centre) average horizontal PGA for the 2008 Wenchuan earthquake. The circles show the observed and simulated PGA at the strong motion stations. Right: Residuals at the stations.

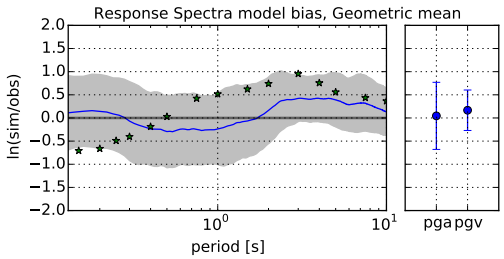

Figure 4.4: Model bias for response spectra using 95 sites for the Wenchuan earthquake. The continuous line denotes the model bias, the gray shades show ± the rms error . Stars indicate the model bias for spectral response estimate with the GMPE of Boore and Atkinson (2008) for a Vs30 value of 320 m/s. On the right, the biases related to the PGA and PGV values are shown.

certain similarities in terms of directivity, but also that the simulation overestimated the observed values in several areas. Additionally, residuals are plotted to explicitly show differences at individual stations. For most of the stations, PGA is matched and no general over- or undershooting is observed. Large discrepancies occur mainly for stations close to the fault, but predominantly on the footwall side. For these locations, PGA is significantly overestimated. This might be attributed to too strong forward and backward directivity effects which are caused by the unperturbed rupture velocity (Kurahashi and Irikura, 2010). In order to consider relative differences of PGA compared to the amplitude of observed PGA, the logarithmic difference might be considered. Logarithmic difference of PGA is also large at the hanging wall site, west of the fault plane, while logarithmic differences are less pronounced north and south of the northernmost and southernmost edge of the fault, respectively. The reader should remember that the regional near-surface structure is not included in the simulation. Hence, the local characteristics of the earth model may largely influence energy radiation from the source at shallow depth and the site amplification at the stations. I will elaborate on that in the discussion of this chapter.

I also compare the model bias for response spectra, PGA and PGV, in a manner similar to the approach of Graves and Pitarka (2010). For station j, the residual between the simulated response spectra $S_j(f_i)$ and the observed response spectra $O_j(f_i)$ at a frequency f_i is given by

$$r_j(f_i) = ln[S_j(f_i)/O_j(f_i)]. \tag{4.1}$$

The model bias is defined as the average residual of all stations. Positive model bias indicates overestimation of amplitude spectra while negative model bias indicates underestimation. Model biases for PGA and PGV are calculated similarly. Figure 4.4 shows the model bias for response spectra of mean horizontal components for all 95 simulated stations and the corresponding root-mean-square(rms) error. It highlights that on average spectral amplitudes are best matched at periods between 0.1 and 2 s. The model tends to

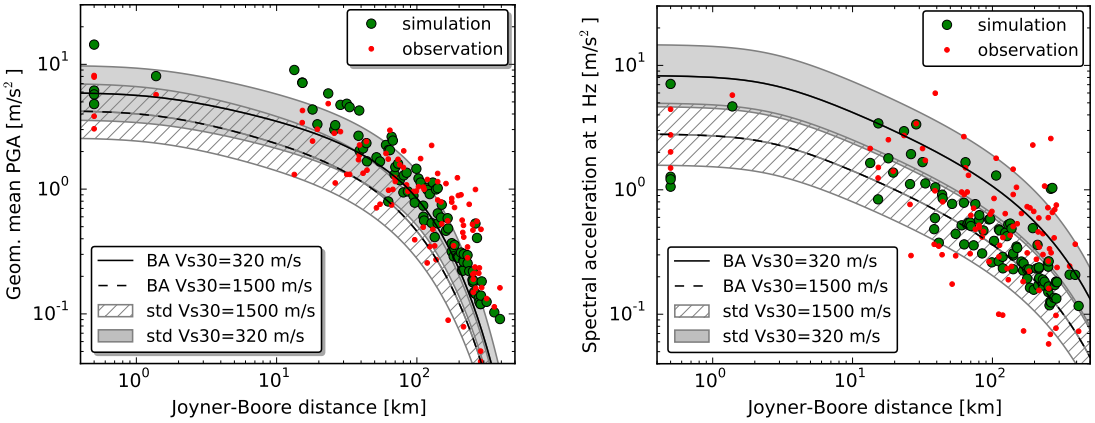

Figure 4.5: Left: Comparison of recorded (small circles) and simulated (large circles) PGA plotted as functions of closest distance to surface projection of the fault for the Wenchuan earthquake. Stations on the surface projection of the fault are plotted at a distance of 0.5 km. Estimated PGA from Boore and Atkinson (2008) is shown as a broken line for Vs30=1500 m/s with hashed area showing one standard deviation and as continuous line for Vs30=320 m/s with grey shade showing one standard deviation of the within-event variability. **Right:** Same for spectral acceleration at 1 Hz (SA1) with 5% damping.

overshoot at periods higher than 2 s. Additionally, the model bias concerning the PGA and PGV values is analysed (see right plot in Fig. 4.4). Both are slightly overestimated.

To compare my simulation results to values from a Ground Motion Prediction Equation (GMPE) I additionally calculated results for the model of Boore and Atkinson (2008). Since Vs30 information is not available to me, I use Vs30 = 320 m/s as representative for soil environment and an upper limit of Vs30 = 1500 m/s for stiff rock. The resulting model bias for a uniform Vs30 value of 320 m/s is also plotted in Fig. 4.4. The model bias for the GMPE is calculated according to Eqn. 4.1 with $S_j(f_i)$ the predicted response spectral acceleration at a frequency f_i for station j. It shows underestimation at small periods and overestimation at high periods. The same observation was made by Lu et al. (2010) who made a detailed comparison of the spectral amplitudes estimated by different GMPE and the observed values during the 2008 Wenchuan earthquake.

Figure 4.5 shows the relation between Joyner-Boore-distance (the distance to the surface projection of the fault) and geometric mean PGA for the observed and simulated values. Overall, the level and trend of the observations are matched by the simulation for distances greater than 40 km. For smaller distances, the simulation tends to exceed the observed level of ground motion. Values predicted by the GMPE of Boore and Atkinson (2008) match the observation well for a uniform Vs30 value of 320 m/s. They fall slightly below the observations at larger distances. However the level of the GMPE estimates is strongly dependent on the chosen value for Vs30. The underestimation becomes significant if higher Vs30 values are used. The variability of my simulation is comparable to the

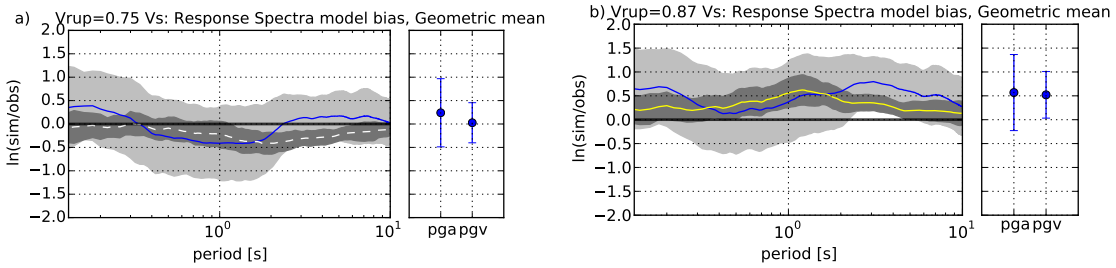

Figure 4.6: (a) Same as Fig. 4.4 but now for a rupture velocity of $0.75 \cdot v_s$ instead of $0.8 \cdot v_s$. The continuous line denotes the model bias regarding the observations while the broken line shows the model bias to the reference simulation shown in Fig. 4.4. Light gray denotes the rms error with respect to the observations. Dark gray shows the rms error with respect to the reference simulation shown in Fig. 4.4. (b) same as (a) but for an increased rupture velocity of $0.87 \cdot v_s$.

one standard deviation given by the GMPE, for which I show the within-event variability (Atik et al., 2010) of the GMPE only, while excluding between-event variability.

The same plot is also shown for spectral acceleration at 1 Hz (SA1) in Figure 4.5, which is defined as the maximal acceleration a single-degree-of-freedom oscillator with a natural frequency of 1 Hz would experience if subjected to the acceleration time series. A damping of 5% is employed. For the spectral acceleration at 1 Hz no overestimation is recognised at small distances. The simulated values are following the trend of the observed values at all distances. Compared to PGA, the distribution of SA1 shows a larger spread. At least for distances larger than 100 km the variability of the observation is larger than the variability of the simulation, which is equally true for the distribution of PGA.

Validation of rise time scaling

One major advantage of my method is that there is no parameter which has to be tuned manually in order to achieve ground motion simulations with approximately correct high-frequency content. To demonstrate this, I conduct simulations in which the rupture velocity is changed in the case of the Wenchuan earthquake, while still applying the rise time scaling to the energy.

I perform two additional simulations with rupture velocities decreased to $0.75 \cdot v_s$ and increased to $0.87 \cdot v_s$, as compared to $0.8 \cdot v_s$ used so far. For the main part of the fault this leads to rupture velocities of around 2.6 km/s and 3.0 km/s respectively.

As a lower rupture velocity results in a larger overall fault rise time and because the signal is extended, without energy related rise time scaling we expect the ground motion amplitudes to be smaller than in the previous cases. However, after fixing the rupture times of each fault patch, again the rise time is adjusted, such that the radiated seismic energy is reproduced. Fig. 4.6a shows that thereby it is possible to match the observed energy level almost equally well for a smaller rupture velocity. The model bias for the medium spectral periods changes due to the change in rupture velocity. Compared to the previous

depth(km)	v_p(km/s)	v_s(km/s)	density(g/cm^3)	Q_S
0-4	3.80	2.19	2.2	150
4-8	5.50	3.18	2.6	250
8-18	5.80	3.34	2.7	250
18-28	6.50	3.74	2.9	300
>28	7.80	4.50	3.2	600

Table 4.2: Crustal velocity model used for the calculation of the Green's function for the 2003 Tokachi-Oki earthquake, adopted from Yagi (2004).

simulation less energy is radiated for periods ranging between 0.5 and 10 s. However, the small periods, i. e. the high frequency ground motion, are almost unchanged. The same is true for the increased rupture velocity (Fig. 4.6b). Again, the changes in rupture velocity cause changes in the medium frequency range. However, the high frequency content is fixed due to the adjusting of the rise time and is very similar to that of the previous simulation. This demonstrates that the energy scaling works as expected. Changes in the kinematic rupture model influence the simulation outcome, but with approximately correct input parameters, the observation can be satisfactorily reproduced.

4.2 Application to the 2003 Tokachi-Oki earthquake

On 25 September 2003, the Tokachi-Oki earthquake occurred off the Japanese coast, south-east of Hokkaido. The large thrust event along the upper boundary of the subducting pacific slab had a seismic moment of $1.7 \cdot 10^{21}$ Nm (Yagi, 2004) corresponding to $M_w = 8.1$.

Thanks to a dense network of strong motion records provided by KiK-Net of the National Research Institute for Earth Science and Disaster Prevention (NIED) (Aoi et al., 2004), we are able to compare simulations to 145 strong motion stations. Throughout this section I use KiK-net borehole data for the comparison. Moreover, 1-Hz GPS data are provided by the Japanese Geographical Survey Institute (GSI) which established the permanent GPS observation station network GEONET covering all the Japanese islands. The GPS measurements also permit to compare the results of my simulations to the recorded displacements. Locations of strong ground motion and GPS stations are shown in Fig. 4.7.

For the simulation of the 2003 Tokachi-Oki earthquake I calculated Green's functions in a layered earth on a grid of approximately 1 km. The 1D-earth model is adopted from Yagi (2004) and given in Table 4.2. Again, no station-specific near surface information was included in the simulation, i. e. all stations share the same velocity model. The source geometry, the slip distribution and a seismic moment of $2.2 \cdot 10^{21}$ Nm are obtained from the inversion of static GPS displacements by Mingpei Jin (pers. communication). Note that also in this case the slip model was constrained only by static displacement and no kinematic information about the rupture process is included. The hypocentre is situated at

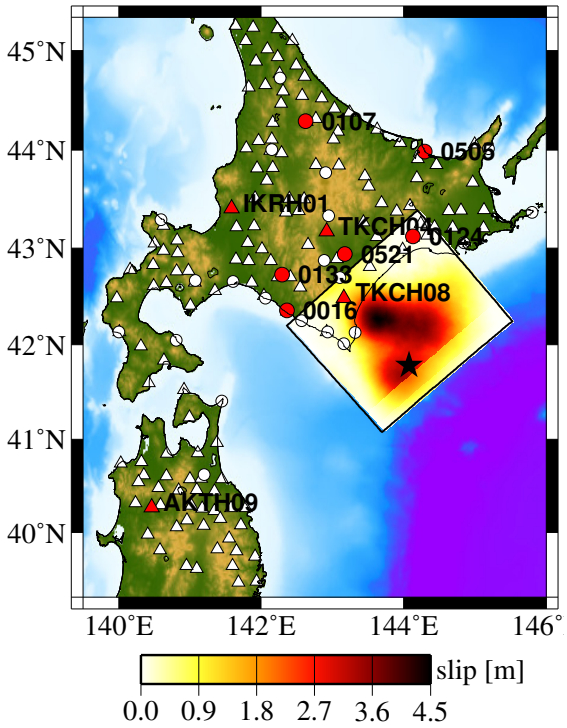

Figure 4.7: Map view of the 2003 Tokachi-Oki earthquake. Triangles and circles indicate the strong motion and GPS stations, respectively. Stations to which simulations are compared in Fig. 4.8 and Fig. 4.12 are marked by filled triangles and circles, respectively. The black star marks the hypocentre.

latitude 41.78° N and longitude 144.08° E, resulting in an down-dip propagating rupture. We use a rupture velocity of $v_{\text{rup}} = 0.7 \cdot v_s$, which is close to the 2.6 km/s for the shallow parts of the rupture, similar to the value inferred by forward modelling by Nozu and Irikura (2008). Proportional to the velocity model, the rupture speed increases to 3.15 km/s for the deeper parts of the fault. The assumed energy magnitude is $M_e = 8.0$ (USGS). Using a discretisation of 200 m this leads to a rise time of 0.05 s.

Figure 4.8 shows modelled and observed waveforms at 4 selected stations at different distances from the fault. For these examples similar characteristics in terms of amplitude and signal duration are found for simulations and observations at the near-fault stations (TKCH09 and TKCH04) and also at greater distances from the fault (station IKHR01). At IKHR01 the simulation appears to have stronger high-frequency ground motion at the beginning of the shaking than the observation. The same is true for AKTH09, where the simulation as a whole exhibits too strong shaking compared to the observation, especially on the vertical component. In Fig. 4.9, I compare observed and simulated peak ground accelerations. On Hokkaido, the general level of PGA values is well matched. The simulated values tend to fall short of the observations at the coast, especially at the south-

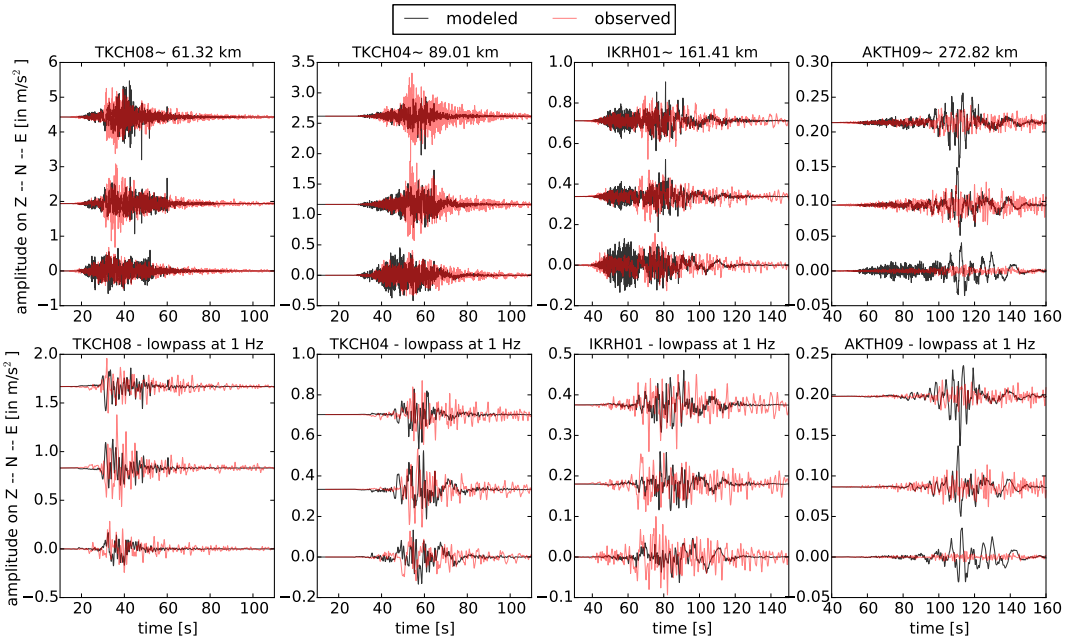

Figure 4.8: Comparison of recorded (red) and simulated (blue) three-component ground-velocity waveforms at three selected sites for the Tokachi earthquake. **Top:** Broadband ground velocity waveforms. The title gives the station name and closest distance to the surface projection of the fault. **Bottom:** Waveforms low-pass filtered at 1 Hz. Station locations are indicated in Fig. 4.7.

eastern part of the island. The PGA values at the western part of the island are slightly overshooting the observations. Logarithmic difference show that PGA is overestimated at larger distances from the fault, in the northern part of Hokkaido and for stations on Honshu south of 40° latitude. On average, the simulation matches the observation well as shown by the model bias in Fig. 4.10. For response spectra, PGA and PGV the model bias is close to zero. However, the root-mean-square (rms) error is still up to 1.0 natural log unit, resulting from large differences between observations and simulations for some of the stations. Here, I also compare the observations to the GMPE of Zhao et al. (2006). This comparison should be regarded with care, as the regression was not made for borehole but for surface stations. We show its results under the assumption, that borehole stations behave similarly as hard rock stations with high Vs30. In this case the general ground motion level is met by the prediction for stiff rock (Vs30=1500 m/s). The GMPE tends to overpredict the observations at small periods, while the predicted ground motion at large periods is too weak. The prediction works well for periods between 1 and 4 s. Figure. 4.11 shows that the observed PGA seems to decrease more rapidly with increasing distance to the fault than predicted by Zhao et al. (2006). My simulation matches this decrease with distance better than the GMPE, even though the simulated attenuation is

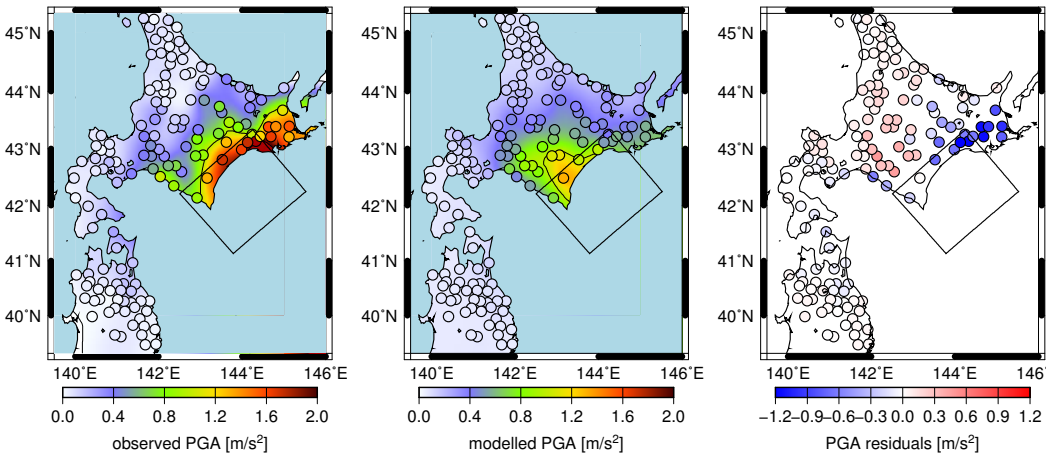

Figure 4.9: Comparison of interpolated observed (left) and modelled (centre) average horizontal PGA for the 2003 Tokachi earthquake. The circles show the observed and simulated PGA at the strong motion stations. Right: Residuals at the stations.

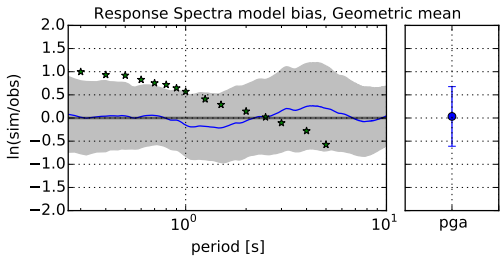

Figure 4.10: Model bias for Fourier spectra using 145 sites for the Tokachi-Oki earthquake. The continuous line denotes the model bias, the gray shades show ± the rms error. Stars indicate the model bias for spectral response estimate with the GMPE of Zhao et al. (2006) using a Vs30 value of 1500 m/s. On the right, the bias related to the PGA value is shown.

still weaker than the observed. Again, the variability of my simulation is comparable to the one standard deviation of within-event variability of the GMPE. Also, the variability of the observation is of the same order of magnitude. Figure 4.11 also shows the attenuation with distance for the spectral acceleration at 1 Hz. The relation between simulated and observed values is similar: the simulation seems to show a slightly weaker attenuation with distance. Simulated SA1 tends to underestimate the observations. The difference to the empirical equations is more significant here. While the prediction of Zhao et al. (2006) with Vs30=1500 m/s matches the observation quite well at small distances, the prediction are too large at larger distances. For a Vs30 of 320 m/s almost all values of SA1 are overestimated.

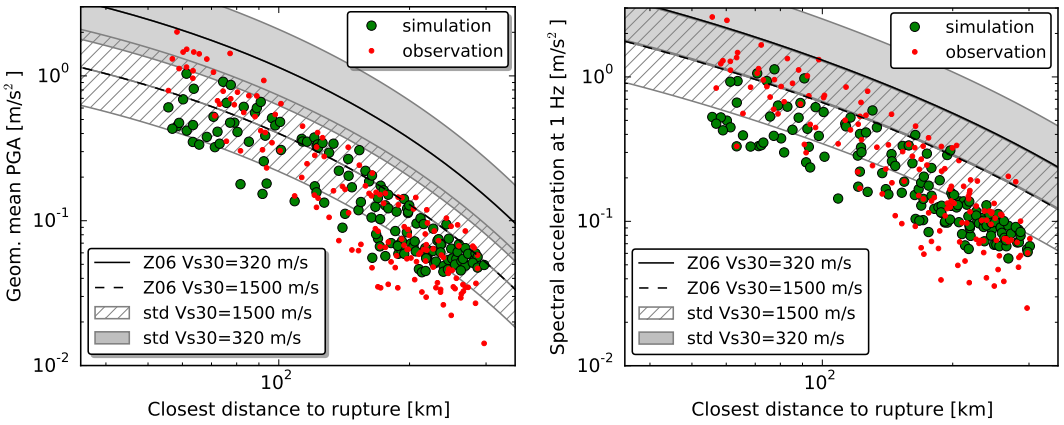

Figure 4.11: Left: Comparison of recorded (small circles) and simulated (large circles) PGA plotted as functions of closest distance to the rupture for the Tokachi-Oki earthquake. Estimated PGA from Zhao et al. (2006) is shown as a broken line for Vs30=1500 m/s with hashed area showing one standard deviation and as continuous line for Vs30=320 m/s with grey shade showing one standard deviation. Here, only within-event variability is used for the empirical ground motion prediction. **Right:** Same for spectral acceleration at 1 Hz (SA1) with 5% damping.

As the observations of the GEONET 1 Hz GPS data are available for this earthquake, I compare the results of my simulations to the recorded displacement time series. Fig. 4.12 shows the comparison of the simulated and observed displacements after low-pass filtering at 0.05 Hz suppressing noise at higher frequencies in the GPS data. We are able to approximately reproduce the maximal displacement amplitude. Since the slip distribution was inverted from the permanent displacement, for most stations and components the permanent displacement is reproduced. But also the alignment with the waveforms is fairly good. This shows that my approach is able to simulate the low-frequency displacement data up to the permanent displacement.

4.2.1 Constant rupture velocity introducing supershear effects

In Section 3.1.4 I stated that the modelling with constant rupture velocities along the fault bears the risk of introducing areas of supershear. In those areas the rupture propagates at a speed faster than the S-wave velocity. This leads to extreme directivity effects on the ground motion.

The Tokachi-Oki earthquake provides a good case to demonstrate this behaviour. Published observed rupture velocities go up to 4.5 km/s (Yagi, 2004). Figure 4.13 shows simulated PGA values for constant rupture velocities of 4.0, 3.6 and 3.2 km/s. The simulation with the high rupture velocity of 4.0 km/s shows everywhere an overestimation of PGA. The values are too high at all simulated stations. Extremely high ground motions are simulated on the north-eastern part of Honshu, even though these locations are much more distant from the fault than the coastal stations on Hokkaido. This extreme over-

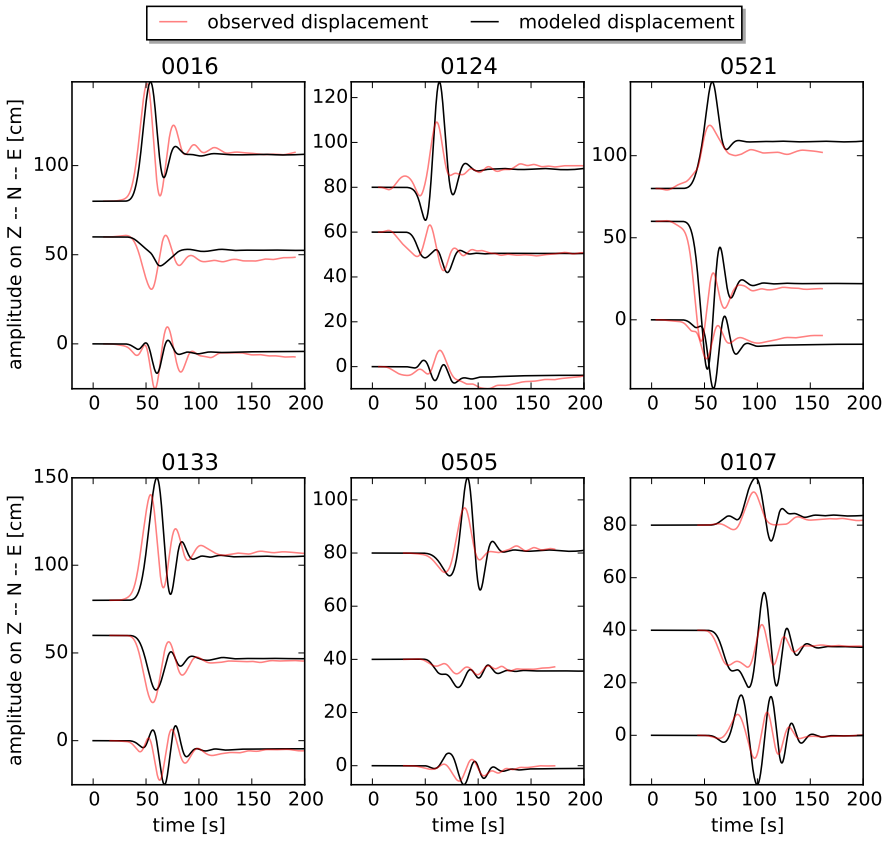

Figure 4.12: Comparison of modelled displacement time series to observations. All time series are low-pass filtered at 0.05 Hz. Displacements are given in cm. The baselines of the N and E component are shifted to increase visibility.

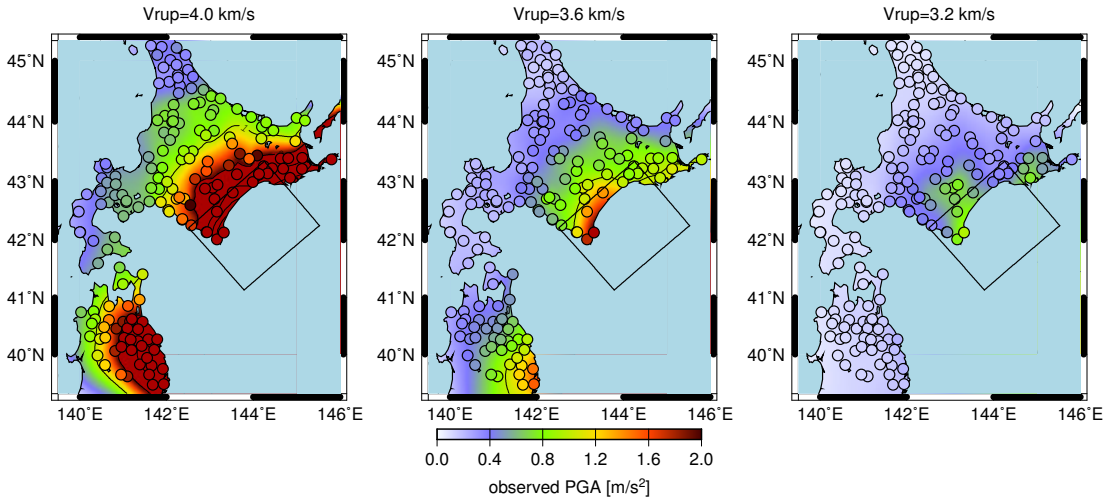

Figure 4.13: PGA distributions for the Tokachi-Oki earthquake simulated with different constant rupture velocities (left 4.0 km/s, middle 3.6 km/s and right 3.2 km/s).

estimation comes from the fact that at a rupture velocity of 4.0 km/s major parts of the fault rupture at supershear velocity. A smaller rupture velocity of 3.6 km/s (Fig. 4.13) significantly reduces this effect as most of the fault ruptures at subshear velocities. However, due to supershear still occurring on the shallower parts of the rupture plane, the simulation still overshoots PGA values at the north-east coast of Honshu. Those PGA values at stations in a distance of more than 200 km from the fault are as high as the PGA at stations at 70 km from the rupture plane. Only at a rupture velocity of 3.2 km/s, when the whole fault ruptures at speeds well below the S-wave velocity, simulated PGA in the north-eastern part of Honshu is similar to the observed PGA. However in this case, the PGA is undervalued at the southern coast of Hokkaido. Compared to the simulation with a rupture velocity proportional to the depth-dependent S-velocity presented in Section 4.2, all scenarios with a constant rupture velocity perform worse.

Constant rupture velocities can be appropriate, if the fault does not rupture across strong velocity gradient of the earth model. In contrast, if multiple layers with strong wave velocity variations are ruptured, a depth-dependent rupture speed is clearly recommended.

4.3 Application to the 1994 Northridge earthquake

On January 17th, 1994, an earthquake with moment magnitude $M_w = 6.7$ (USGS,NEIC) struck the San Fernando Valley region of Southern California. The hypocentre was located in Northridge, a neighbourhood of Los Angeles, in a depth of 17 km. The rupture occurred on a blind thrust fault – a fault that did not rupture the surface layer and is buried under the uppermost layers of rock. It generated extreme ground motions in the surrounding urban area, thereby causing immense damage and loss of life. Due to the large amount of

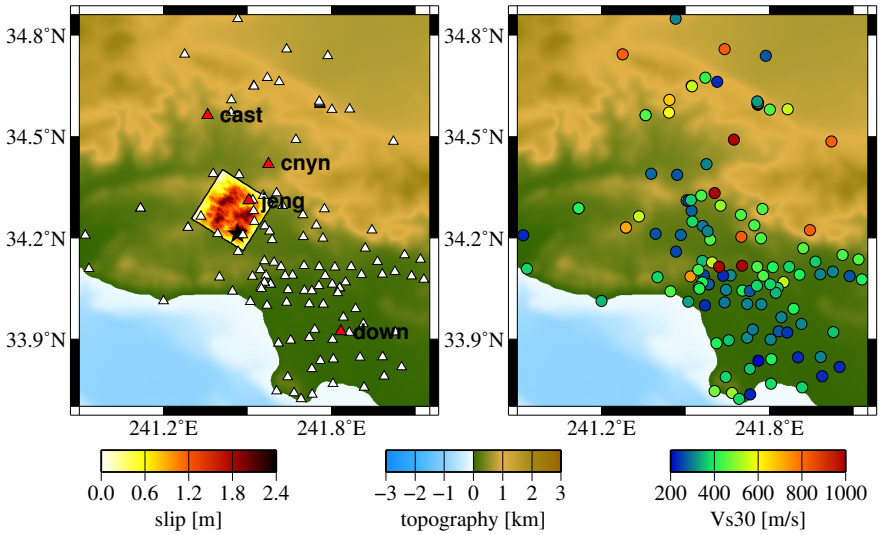

Figure 4.14: Left: Map view of the 1994 Northridge earthquake. Triangles indicate the strong motion stations. The black star marks the hypocentre. **Right:** Vs30 values of the stations.

strong motion sensors in the California region, a lot of ground motion data were recorded and are available for comparison. The location of the rupture plane and of the stations used in the simulations are shown in Fig. 4.14. This figure also shows Vs30 values as published by Graves and Pitarka (2010) who retrieved those mainly from the NGA dataset (http://peer.berkeley.edu/nga). For the simulation the velocity model was adopted from Graves and Pitarka (2010), who designed this 1D-profile by averaging the velocity profiles of the version 4 of the Southern California Earthquake Center (SCEC) Community Velocity Model (CVM4) sampled at each of the strong-motion recording sites. However, I averaged the velocities of the most shallow layers, such that the thickness of the uppermost one is 100 m. The velocity model is listed in Tab. 4.3. The slip distribution used originates from an inversion of strong motion data by Hartzell et al. (1996), as well as the seismic moment M_w of $1.4 \cdot 10^{19}$ Nm. Their result shows a 20 km long and 24 km wide fault with a strike of 122° and a dip of 40° to the southwest. The rupture velocity is fixed by the coefficient $\gamma = 0.8$, resulting in rupture velocities close to the rupture speed of 2.8 km/s at the beginning and 2.5 to 2.0 km/s at the termination as reported by Hartzell et al. (1996). The hypocentre is located at latitude 34.21° and longitude -118.54° . The energy magnitude determined by Di Giacomo (2010) is M_e =6.7. The κ used for this simulation is 0.035 s, which is in the range of values found by Kilb et al. (2012) for stations in southern California and the mean estimate of Boore and Joyner (1997).

Figure 4.15 shows four example waveforms of the simulation compared to the observed ground motion, for the broadband ground velocity (top row of Fig. 4.15) as well as for waveforms filtered with a low-pass at 1 Hz. The sites are indicated on the map in Fig. 4.14

depth(km)	v_p(km/s)	v_s(km/s)	density(g/cm^3)	Q_S
0.0-0.1	2.40	1.20	2.20	200
0.1-0.3	2.80	1.40	2.30	200
0.3-0.5	3.10	1.60	2.40	200
0.5-0.7	3.40	1.80	2.45	300
0.7- 1	3.70	2.10	2.50	500
1- 3	4.40	2.40	2.60	500
3- 5	5.10	2.80	2.70	500
5- 6	5.60	3.15	2.75	500
6-11	6.15	3.60	2.83	1000
11-16	6.32	3.65	2.85	1000
16-21	6.55	3.70	2.90	1000
21-31	6.80	3.80	2.95	1000
>31	7.80	4.50	3.20	1000

Table 4.3: Crustal velocity model used for the calculation of the Green's function for the 1994 Northridge earthquake, adopted from Graves and Pitarka (2010).

and were chosen to show waveforms directly on top of the fault, in the very near field and in a larger distance from the fault. For the three stations closest to the fault the peak ground velocity is approximately matched, while the observed seismogram at the remote station exhibits larger values than simulated. The low-pass filtered waveforms also show that some of the most prominent features of the low-frequency ground motion are well reproduced. For the station directly on the surface projection of the fault (JENG) and the very close distance station (CNYN), the duration of the shaking is also matched by the simulation. However, the stations at further distance (CAST, DOWN) show longer shaking than simulated, probably reflecting the influence of the horizontal heterogeneity of the subsurface. This is true for a lot of stations in this simulation: the observed waveforms at the onset of the ground shaking are often well reproduced, but the data shows longer-lasting shaking than the simulation, which is probably due to the 3D-velocity structure.

Figure 4.16 illustrates observed and simulated PGA as well as the residuals for the 1994 Northridge earthquake. Largest PGA is simulated at the upper edge of the fault, due to the smallest distance from the rupture plane and the up-dip rupture propagation. Observed PGA is also large in this area, but the highest observed PGA is found at the south-eastern corner of the surface projection of the fault. For this example, the map to the right shows logarithmic PGA residuals, which stronger emphasise the relative differences for the small PGA values. It shows pronounced overestimation at stations close to the up-dip edge of the fault and strong underestimation of PGA values south of the fault, in the lowlands east of the Santa Monica Bay. Differences are most likely caused by the 3D-structure not being included in the simulation. Fig. 4.14 shows that stations in the lowlands are placed on sediments with Vs30 smaller than the one used in the velocity model and that stations to the north are placed on mountainous grounds, which is more

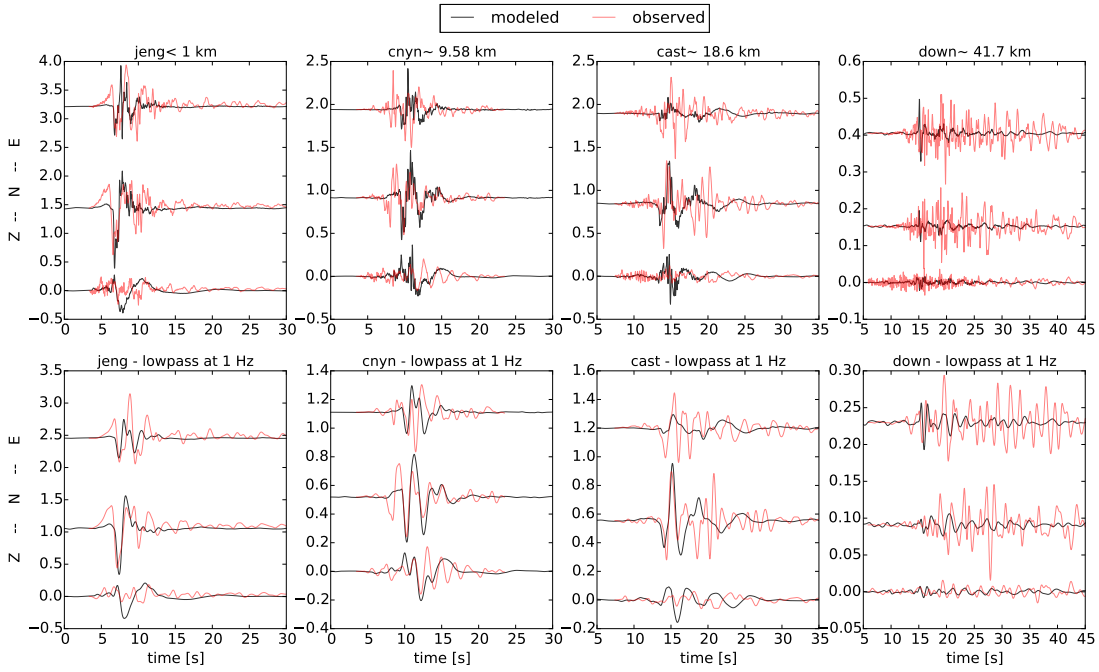

Figure 4.15: Comparison of recorded (red) and simulated (blue) three-component ground-velocity waveforms at four selected sites for the Northridge earthquake. **Top:** Broadband ground velocity waveforms. The title gives the station name and distance to the surface projection of the fault. **Bottom:** Waveforms low-pass filtered at 1 Hz. Station locations are indicated in Fig. 4.14.

likely to exhibit the characteristics of the simulated rock model. Hence, site effects due to amplification in the sedimentary basin are leading to increased ground motions in the south of the considered region. The model bias for the response spectra is plotted in Fig. 4.17. For almost all periods the spectral acceleration is underestimated by the simulation. Only for the long-period ground motion, the observed and simulated ground motion agree on average. Interestingly, the predicted response spectral accelerations from the GMPE of Boore and Atkinson (2008) show the same behaviour as our simulation. They equally underestimate the short-period ground motion while spectral acceleration is predicted approximately correct for long periods. The assumed Vs30 for the GMPE is 1200 m/s, which is just the same as the S-velocity in the shallowest layer of the velocity model used for the simulation. For a smaller value of Vs30 = 320 m/s, which are probably more appropriate for the station in the lowlands, the model bias of the GMPE is shifted towards higher values, such that it is very close to zero at most periods, but spectral accelerations at long periods tend to be overestimated.

The attenuation of observed PGA with distance is shown in Figure 4.18. Both, simulated and observed peak ground acceleration decrease in a similar way with distance. At

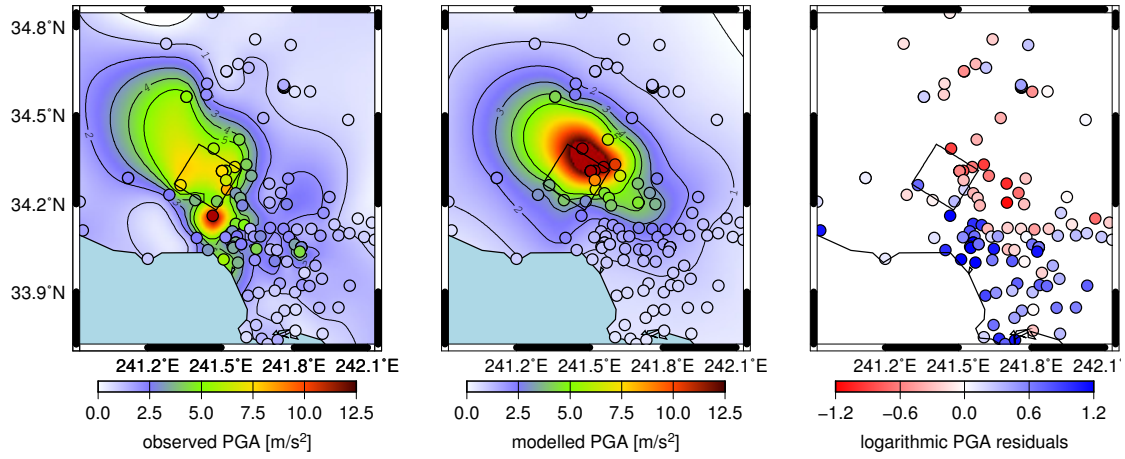

Figure 4.16: Comparison of interpolated observed (left) and modelled (centre) average horizontal PGA for the 1994 Northridge earthquake. The circles show the observed and simulated PGA at the strong motion stations. Right: Logarithmic PGA residuals, $\ln(\mathrm{PGA_{obs}}/\mathrm{PGA_{sim}})$, at the stations.

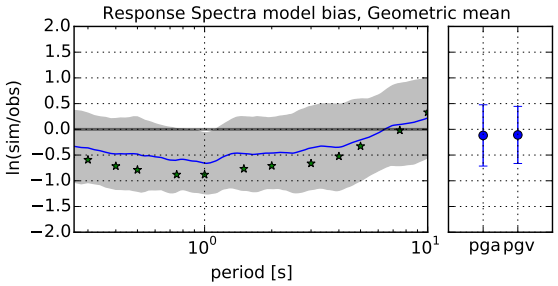

Figure 4.17: Model bias for response spectra of geometric mean horizontal components using 118 sites for the Northridge earthquake. The continuous line denotes the model bias, the gray shades show the model bias ± the rms error. Stars indicate the model bias for spectral response estimate with the GMPE of Boore and Atkinson (2008) for a Vs30 value of 1200 m/s. On the right, the biases related to the PGA and PGV values are shown.

the second glance the attenuation of the observations seems smaller than simulated: In the near-field, several of the simulated values overshoot the measurements, while at the remote stations the observations exceed the simulations. The attenuation curve from the ground motion prediction equation of Boore and Atkinson (2008) is plotted for comparison for Vs30 values of 320 and 1200 m/s. For the higher Vs30 the observation clearly exceeds the prediction, especially at large distances. For Vs30=320 m/s, the prediction of PGA is closer to the measurements. Especially at the stations in the far-field, the variability of the observations is higher than the one standard deviation of within-event variability predicted by the GMPE. In contrast, the variability of the simulation is higher at small distances and decreases with distance.

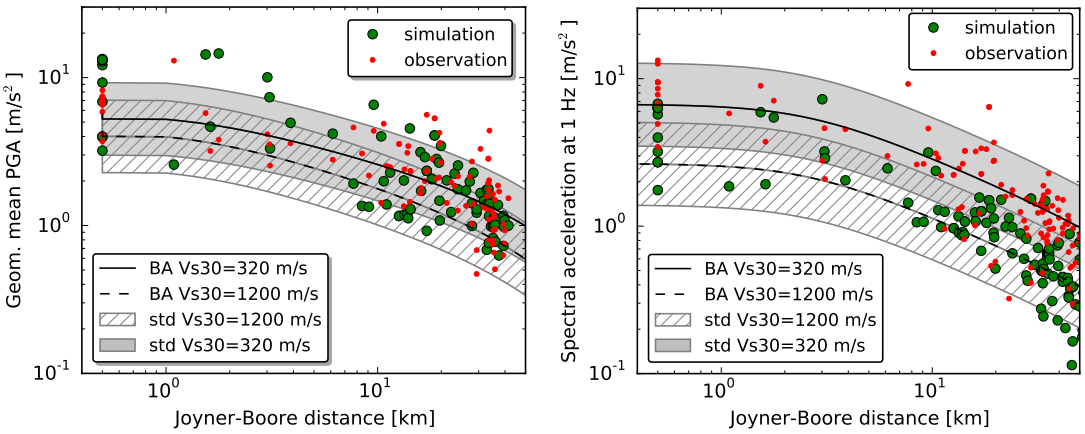

Figure 4.18: Left: Comparison of recorded (small circles) and simulated (large circles) PGA plotted as functions of closest distance to the surface projection of the fault for the Northridge earthquake. Stations on the surface projection of the fault are plotted at a distance of 0.5 km. Estimated PGA from Boore and Atkinson (2008) is shown as a broken line for Vs30=1200 m/s with hashed area showing one standard deviation and as continuous line for Vs30=320 m/s with grey shade showing one standard deviation. **Right:** Same for spectral acceleration at 1 Hz (SA1) with 5% damping.

As can be recognised from the model bias of response spectra in Fig. 4.17, the spectral acceleration at 1 Hz (SA1) is underestimated by the simulation. This is also visible in Figure 4.18, showing SA1 depending on the Joyner-Boore distance. The spectral acceleration resulting from the simulated time-series is smaller than the one from the observed time-series at all distances. However, the empirical relation by Boore and Atkinson (2008) for a Vs30 value of 320 m/s seems to reproduce the observed values quite well.

4.3.1 Simulation using a Vs30 of 320 m/s

Given the good performance of the ground motion prediction equation of Boore and Atkinson (2008) with a Vs30 value of 320 m/s, I modified the velocity model for the calculation of the Green's function. The uppermost 50 m are now constrained to an S-velocity of 320 m/s. The velocities of the following shallow layers are also slightly smaller than in the previous model, leading to a gradual increase in S-velocity. The velocity structure of the modified layers is given in Table 4.4.

Figure 4.19 shows that the model bias for the response spectra is much closer to zero for this modified simulation. The model bias does not exceed 0.5 anywhere and the standard error varies between 0.5 and 0.7. For the GMPE the model bias is also significantly reduced for small periods and only for long periods the GMPE tends to predict too high spectral accelerations. In contrast, simulated PGA and PGV are now significantly higher than the observed values, leading to a positive model bias for both.

This is equally visible in Figure 4.20, where simulated and observed PGA are plotted against the Joyner-Boore distance. Especially close to the fault, PGA is overestimated

depth(km)	v_p(km/s)	v_s(km/s)	density(g/cm^3)	Q_S
0.0-0.05	0.64	0.32	2.20	150
0.05-0.1	1.80	0.90	2.20	200
0.1-0.3	2.40	1.20	2.30	200
0.3-0.5	3.00	1.50	2.40	200
0.5-0.7	3.40	1.80	2.45	300
0.7- 1	3.70	2.10	2.50	500
>1		see Tab. 4.3		

Table 4.4: Modified crustal velocity model used for the calculation of the Green's function for the 1994 Northridge earthquake with a Vs30 of 320 m/s. The modified layers for the uppermost 1 km are given. Layers deeper than 1 km are identical with the velocity model given in Tab. 4.3.

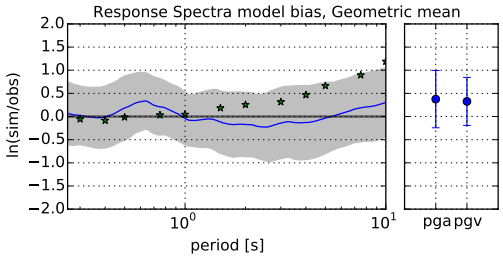

Figure 4.19: Model bias for response spectra of geometric mean horizontal components using 118 sites for the Northridge earthquake and the modified earth model with Vs30 = 320 m/s. The continuous line denotes the model bias, the gray shades show the model bias ± the rms error. Stars indicate the model bias for spectral response estimate with the GMPE of Boore and Atkinson (2008) for a Vs30 value of 320 m/s. On the right, the biases related to the PGA and PGV values are shown.

by the simulation, but also at remote distances PGA tends to be too high. However, this overestimation is not seen for the spectral acceleration at 1 Hz. SA1 is approximately matched at all distances and the variability of the simulations seems to be similar to the variability of the observations.

These results show, that for the 1994 Northridge earthquake a velocity model with smaller S-velocities for layers shallower than 1 km depth seems more appropriate. The overall model bias could be significantly reduced. However, the peak values of the ground acceleration are matched worse with this velocity model. This demonstrates that different characteristics of the waveforms are not necessarily matched equally well by the same simulation and that good agreement between observation and simulation for one key fiugre, does not mean the same agreement for another quantity.

The simulation also points out the importance of the most shallow layers. Although only the uppermost 1 km of the velocity model was modified, the simulation results differ

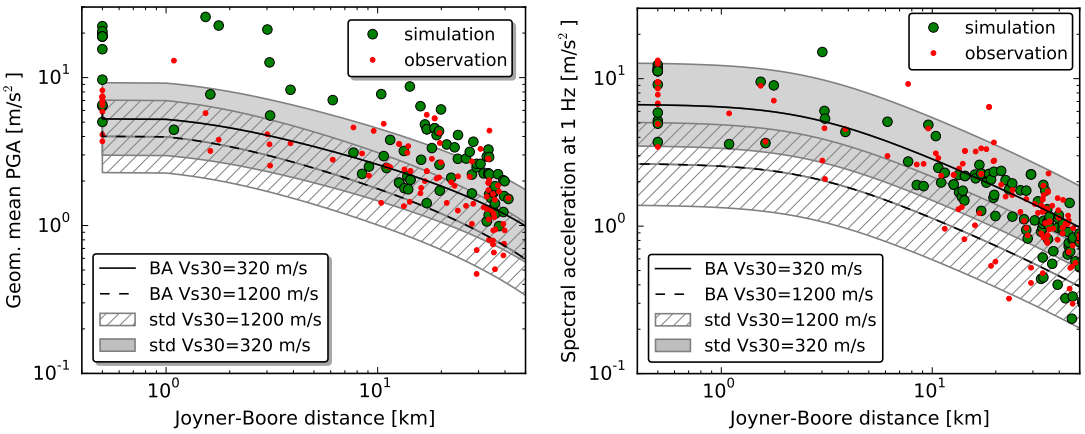

Figure 4.20: Left: Comparison of recorded (small circles) and simulated (large circles) PGA plotted as functions of closest distance to surface projection of the fault for the Northridge earthquake and the velocity structure in Tab. 4.4. Stations on the surface projection of the fault are plotted at a distance of 0.5 km. Estimated PGA from Boore and Atkinson (2008) is shown as a broken line for Vs30=1200 m/s with hashed area showing one standard deviation and as continuous line for Vs30=320 m/s with grey shade showing one standard deviation. **Right:** Same for spectral acceleration at 1 Hz (SA1) with 5% damping.

significantly from the previous waveforms. It clarifies that knowledge of the local velocity structure is a necessity for the successful modelling of seismograms.

4.3.2 Comparison to 3D-simulation

The performance of the method is strongly connected to the velocity model used. For the region of Southern California not only a detailed 3D-velocity model has been established (SCEC CVM4, 2014), but also a kinematic modelling approach has been tested with this model by Graves and Pitarka (2010). Since the full kinematic source description and the results are available from their publication, the identical rupture scenario can be combined with my wave propagation in a layered medium and the simulated waveforms can be compared.

The description of the source is similar to the presented procedure for the slip and the rupture velocity. The largest difference is found in the patch rise time τ_i, which is proportional to the patch slip u_i

$$\tau_i = \begin{cases} 2 \cdot k \cdot u_i & : z < 5\,\text{km} \\ k \cdot u_i & : z > 8\,\text{km} \end{cases} \tag{4.2}$$

with the parameter k being fixed by the condition, that the average rise time over the entire fault τ_A is determined by

$$\tau_A = \alpha_\tau \cdot 1.6 \cdot 10^{-9} \cdot M_0^{1/3}. \tag{4.3}$$

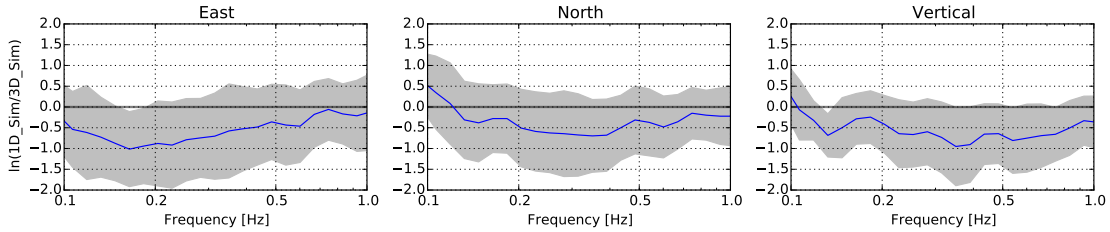

Figure 4.21: Model bias for Fourier amplitude spectra between the 1D-simulation and the 3D-simulation of Graves and Pitarka (2010) using 118 sites for the Northridge earthquake. The two simulations use identical kinematic sources but different approaches and velocity models for the wave propagation. The continuous line denotes the model bias, the gray shades show ± the rms error.

The constant α_τ scales the average rise time depending on the dip of the fault

$$\alpha_\tau = \begin{cases} 1 & : \delta > 60° \\ 0.82 & : \delta < 45° \end{cases} \tag{4.4}$$

with a linear transition between dips of 60° and 45° .

Additionally the moment rate function assumed by Graves and Pitarka (2010) with this rise time has the functional form proposed by Liu et al. (2006), which has a more pronounced peak at the onset and a slower decreasing ending than Brune's source time function. This source time function results in equally strong ground motions at high-frequencies when using larger rise times than in the previous simulations.

I used the identical kinematic description of the source and combined it with previously calculated Green's functions with Vs30 of 320 m/s. Graves and Pitarka (2010) use the deterministic approach for frequencies up to 1 Hz so that, here, I only compare the simulations for the frequency range between 0.1 and 1 Hz. Before the calculation of response spectra, the timeseries of both simulations are bandpass filtered between 0.1 and 1 Hz. Figure 4.21 shows the model bias of Fourier amplitude spectra of the 1D-simulation with respect to the 3D-simulation. For all three components, the model bias reveals that the 3D-simulation exceeds the 1D-simulation at almost all frequencies. Seen that the two simulations use the same source model, the smaller ground motions of the 1D-model are fully caused by the different earth model. In order to enable a comparison to the previously shown model bias for response spectra, the bias between the two simulations is also shown for the response spectra in Figure 4.22. There is almost no model bias between the two different simulations for periods between 1 and 2 s. Low-frequent ground motion at periods between 2 and 10 s is on average smaller when using the layered earth model than for the 3D-velocity model. The root mean square difference between the two simulations is comparable to the rms difference between the observation and simulation shown in subsection 4.3.1.

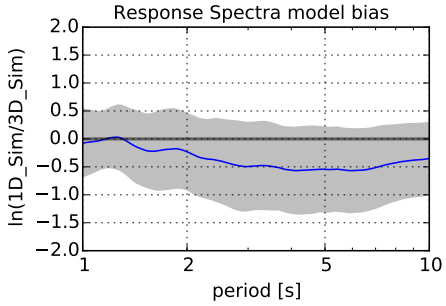

Figure 4.22: Model bias for response spectra between the 1D-simulation and the 3D-simulation of Graves and Pitarka (2010) using 118 sites for the Northridge earthquake. The two simulations use identical kinematic sources but different approaches and velocity models for the wave propagation. The continuous line denotes the model bias, the gray shades show ± the rms error.

The model bias for both Fourier amplitude spectra and response spectra show that the ground motions simulated with the layered earth model are significantly smaller than those obtained using the 3D-model. Figure 4.23 reveals that those differences are indeed connected to the lateral heterogeneity of the velocity model. It shows spectral acceleration at a period of 2 s (SA2) for the two different simulations and the residual when subtracting the SA2 of the 1D-simulation from the SA2 of the 3D-simulation. The residuals form regional clusters with a positive cluster north and north-east of the fault and negative residuals north-west and south-east of the fault. The topography shown in Fig. 4.14 reveals that the positive residuals are observed at stations in mountainous regions, while the negative residuals are found at stations in the low-lands. The velocities of the 1D-models are smaller than those of the 3D-model at the stations placed on hard-rock in the mountains and too high in the sedimentary basins in the flatland.

The comparison between the two simulations shows, that the velocity model has a strong influence on the resulting ground motion over a broad frequency range. According to the model bias for Fourier spectra shown here, ground motion simulations including lateral heterogeneities can be on average more than twice as high as simulations using the layered earth model. Part of these differences can surely be accounted for by using different layered earth models for hard rock stations than for stations placed in sedimentary basins. However, there are geometric effects caused for example by basin structures or topography, which cannot be reproduced by a layered earth model, but which contribute to the site effects.

4.4 Discussion

Although it is often stated that deterministic wave propagation approaches are not suitable for modelling of high frequencies (Graves and Pitarka, 2010), the simulations show that

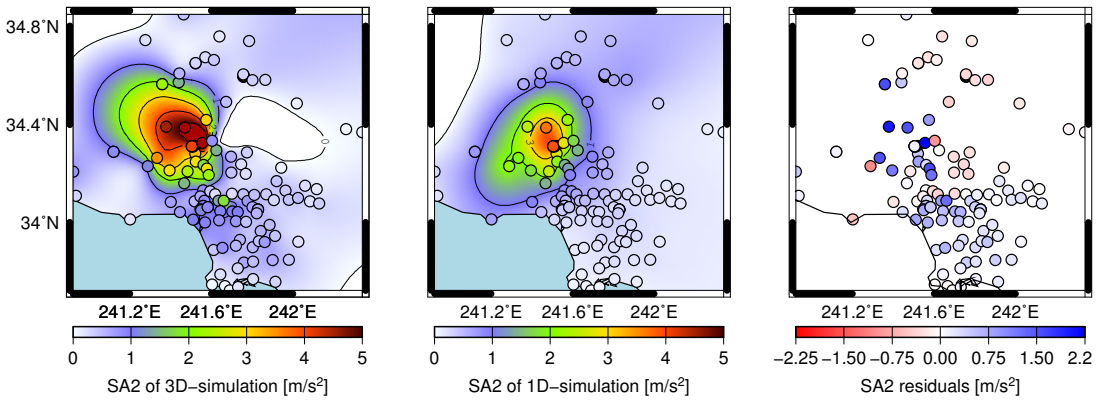

Figure 4.23: Map of spectral acceleration simulated for the Northridge earthquake using two identical kinematic source descriptions but a 3D-velocity model for the wave propagation for the leftmost map and a 1D-velocity model for the centre map. The map to the right displays the residuals when subtracting the results of the 1D- form those of the 3D-simulation.

the outcomes are nevertheless reasonable. It is usually thought that the source and wave propagation phenomena are not sufficiently known at high frequencies and that stochastic simulations are the natural approach considering the stochastic character of natural high-frequency ground motion. However, here I tested the assumption that high-frequency ground motion follows the same rules as low-frequency ground motion, and use the same modelling approach for both frequency ranges. The inclusion of stochastic features in the slip distribution and rupture geometry ensures the natural variability of the seismic source. In particular, I do not account for scattering effects at high frequencies during the wave propagation, but project all variabilities to the fault. As it is not yet possible to distinguish between effects coming from the propagation path or from the rupture process, the inclusion of variability in one feature seems sufficient. For the simulation of the Wenchuan as well as for the Tokachi-Oki earthquake the variability of PGA and spectral acceleration at 1 Hz at large distances is smaller for the simulations than for the observations. I suspect that this is a result of the missing scattering and site effects. At the near-fault stations, the lack of wave scattering is compensated by the small scale variabilities in the source process. At remote stations, the source variability has less influence and the variability in the observations stems from path effects which are not modelled.

I did not yet permit variations of the rupture velocity along the fault. A detailed investigation of the influence of variable slip, fault geometry, rupture velocity and rise time will be a subject of the next chapter.

The approach has general advantages compared to simpler methods such as the application of attenuation laws:

- The approach is in principle applicable to every region of the world where we know the mean underground velocity model.
- There is no limitation concerning the distance range.
- It reproduces directivity effects (requiring the fault geometry and the hypocentre to be correctly determined from data inversion).
- It produces broadband ground motion, i. e. the outcome is the seismic ground motion in a broad frequency band including PGA, but also with approximately correct duration and phasing.

The results of the simulations show that the approach performs well, keeping in mind that it is neither designed for a specific tectonic setting nor does it use the regional velocity model, but only a layered earth model. The influence of the lateral velocity variations are evident in the example of the Northridge earthquakes, as the simulated ground motions deviated strongest from the observation in the lowlands, where strong effects of the sedimentary basin are expected. However, the usage of a layered earth makes the model design very easy and fast, as only a few parameters are needed to start the simulation; this is a major advantage of the method. Alternatively, one could think of using empirical Green's functions instead of numerical ones (Kurahashi and Irikura, 2010; Nozu and Irikura, 2008), as this would be an approach to include path and site effects without detailed knowledge about the local and regional earth structures.

Another influence which might cause deviations of the simulations from observations is a different rupture velocity or seismic moment. For the Tokachi-Oki example Honda et al. (2004) report that the seismic moments obtained from data inversions span a wide range from $0.8 \cdot 10^{21}$ to $3.5 \cdot 10^{21}$ Nm and also the rupture velocity obtained from different inversions range from 2.6 (Nozu and Irikura, 2008) to 4.5 km/s (Yagi, 2004).

Regarding the overprediction for several stations in the Wenchuan case a possible explanation would be an inappropriate modelling of shallow parts of the source. In reality, the rupture is most likely decelerating towards the surface because stress drop is decreasing with decreasing depth. Hence, the shallow part of the fault radiates less energy. As I neglect this behaviour, my approach overestimates the energy radiated from parts of the fault close to the surface. Kagawa et al. (2004) found from kinematic slip inversion that stress drop at shallow asperities is lower than stress drop from deep asperities and that the slip velocity is smaller, which would result in a larger patch rise time. They confirmed this by numerical simulations of ground motions. Additionally Brune and Anooshehpoor (1998) observe longer rise times and slower particle velocities in a rubber foam experiment when introducing a weak layer. According to their arguments, a significant reduction of the radiated seismic energy at high-frequencies could originate from a low value for effective accelerating stress in the shallow weak zone and the velocity-strengthening frictional characteristics of the weak zone. In my simulation I would have to account for that reduction in rise time by, for example, relating the rise time directly to the seismic moment,

which is itself related to the S-wave velocity and therefore smaller in layers of low-velocity. Consequently, an introduction of low velocities at the surface causes much less energy radiated from the shallow parts of the fault and mainly affects the near-field ground motion. On the other hand it causes strong amplifications at all stations with site characteristics of soil or alluvium, such that a simulation including this effect would show even stronger overestimations. Overall, in a simulation implementing soft sedimentary layers the effects of site amplification and rise time reduction would oppose each other and it is difficult to say which contribution would dominate. The method is limited by the usage of the simple layered halfspace. In future investigations, the rise time scaling and the refined source model can be combined with more complicated earth models, such that their performance can be tested in more realistic environments.

The limited knowledge of the earth model also plays a role when considering simulations at large distances. At long distances the factors determining the wave propagation have increasing influence on the ground motion, and probably out of those Q is least known. On the other hand, the waves also travel increasingly larger distances through the deep layers, the parameters of which are globally more constant, and hence, better known on average, as for example the upper mantle. As the aim of this study was merely to demonstrate the performance of the scaling of the rise time by the observed energy magnitude and the possibility of a deterministic wave propagation at all frequencies, I considered a simple Q-model as sufficient.

The scaling of the rise time to the observed energy magnitude provides means to control the rise time without adjusting it manually for each simulation. I showed that the simulations may be realised with changes in parameters (such as rupture velocity) without any interaction with the algorithm. Hence, the proposed rise time scaling can be used to adjust the energy content radiated at high frequencies by using only parameters which can be observed or are obtained by inversions.

A drawback of the rise time scaling is that it does lead to unrealistically high slip velocities. In the example of the Northridge earthquake, the mean rise time of 0.015 s leads to a mean slip velocity of 19 m/s. Maximum observed slip velocities vary between 0.4 to 0.6 m/s (Peyrat and Olsen, 2004) and dynamic rupture simulations confirm this parameter range (Song and Somerville, 2010 and therein reference to Dalguer and Day, 2007). Slightly higher slip velocities of up to 2 m/s have been obtained by kinematic inversion of seismic data by Wald and Heaton (1994). The high slip velocities inferred by the rise time adjustment are probably due to the shape of the moment rate function. Brune's source time function has a rather smooth form, thus very small rise times are required for implementing high frequencies. Other simulation approaches make use of moment rate functions which show more pronounced peaks, for example Liu et al. (2006) and Tinti et al. (2005), or even employ source time functions with the functional form of triangles (Graves and Pitarka, 2004). The mean slip velocity of the simulation using the source description of Graves and Pitarka (2010), which makes use of the moment rate function of Liu et al. (2006), is 1.4 m/s. It is much smaller than the one used with

Brune's source time function but both simulations result in a similar level of ground motion strength. The conclusion is that slip velocities along the fault resulting from the rise time scaling cannot be interpreted as realistic. On the other hand, they do not influence the final simulation results and therefore I did not further investigate this issue.

Chapter 5

Ground motion uncertainty due to rupture process uncertainties

Waveforms resulting from ground motion modelling are affected by a large number of parameters. Some of these parameters are uncertain because of imperfect measurements, others underly a natural variability. Since the method described in the previous chapters uses a deterministic wave propagation, it allows to investigate the influence of the source uncertainty on the resulting uncertainty in ground motion. In the following chapter I quantify which part of the observed ground motion uncertainty can be explained by variability in the source characteristics. On the other hand I also shed light on whether the observed variability in the energy magnitude can reproduce the variability of the observed ground motion. Likewise, I quantify how large the reduction in ground motion variability would be, if we were able to ultimately fix a source parameter or scenario.

5.1 Source uncertainties in kinematic ground motion modelling

Nowadays the method used most often to estimate seismic hazard is Probabilistic Seismic Hazard Analysis (PSHA), a key element of which is the prediction of the ground motion at a site of interest. The commonly used ground motion prediction equations (GMPE) estimate the level of ground motion due to an earthquake at a specific site as a function of various explanatory variables, such as magnitude, distance, fault mechanism and shear wave velocity at the site. Those equations are obtained from the regression of instrumentally recorded strong-motion data, as done, for example, by Abrahamson and Silva (2008), Boore and Atkinson (2008) or Zhao et al. (2006). Compared to the complexity of the physical processes during an earthquake, the functional form of the GMPE is simple. Yet, the predictions are compatible with the observations and, therefore, very useful. However, observed ground motions related to the same explanatory variables show a large scatter around the expected value. This causes residuals remaining after the regression analysis, the distribution of which is characterised by the uncertainty σ. The results of PSHA,

the hazard curves, are strongly influenced by these uncertainties coming along with the ground motion prediction equations, especially at low annual frequencies of exceedance. If the variability in ground motion is high, a destructive event is more likely to occur, hence buildings have to be designed to withstand stronger shaking.

In the context of ground motion simulation the uncertainty is a mixture of the model uncertainty and the parametric uncertainty. Parametric uncertainties may arise because of either model parameters which are not known prior to an earthquake, like the hypocentre location or the distribution of slip, or because of parameters which can not be measured precisely enough, such as the detailed velocity model. They can be estimated by performing simulations which span the possible parameter range. The model uncertainty occurs because we cannot be sure that the theoretical model we developed indeed represents the physical processes. Even if we had perfect knowledge of all model parameters, model uncertainties manifest themselves as bias with respect to the observed ground motions.

Uncertainty can be split up into aleatory uncertainty and epistemic uncertainty. Epistemic uncertainties can be reduced by gathering further knowledge, either about the physical laws and processes or by improving the observation. For instance, the uncertainties connected to the determination of the moment and energy magnitude can be reduced by improving the station coverage and thereby the amount of observations available for the magnitude calculation. Aleatory uncertainties reflect the intrinsic randomness of a phenomenon and cannot be reduced. When an experiment is repeated under the same conditions, with the same parameters, but the outcome is different anyway, the result is subject to aleatory uncertainties. The distinction of the two uncertainties is important for risk assessment and risk communication. For example, in terms of seismic hazard analysis, aleatory and epistemic uncertainties are treated differently. While the aleatory uncertainty is handled in the calculation of the exceedance rates and thereby influences the hazard curve, the epistemic uncertainties are usually handled with logic trees, resulting in a family of hazard curves.

At first sight, the natural variability of ground motions may seem to be an aleatory uncertainty. According to Strasser et al. (2009) several attempts have been made to reduce the uncertainty resulting from the regression of empirical data, including the usage of larger datasets, the inclusion of additional parameters in the predictive model, the development of site-specific attenuation models, and the usage of numerical simulations. Hutchings et al. (2007) conducted a PSHA based on synthetic ground motion for a given magnitude, location and site and found that the range of the Fourier amplitude and acceleration response spectra is comparable to the observed range. Their synthetics are based on several source parameters, the variability of which is constrained by the knowledge obtained from observations. Therefore, they claim that the epistemic uncertainty in ground motion resulting from this variability may be reduced if knowledge about those parameters and their correlations is increased. Although this approach considers the parametric uncertainty only and ignores modelling uncertainty (the uncertainty regarding the model used to calculate the ground motion) this still indicates a possible way to reduce

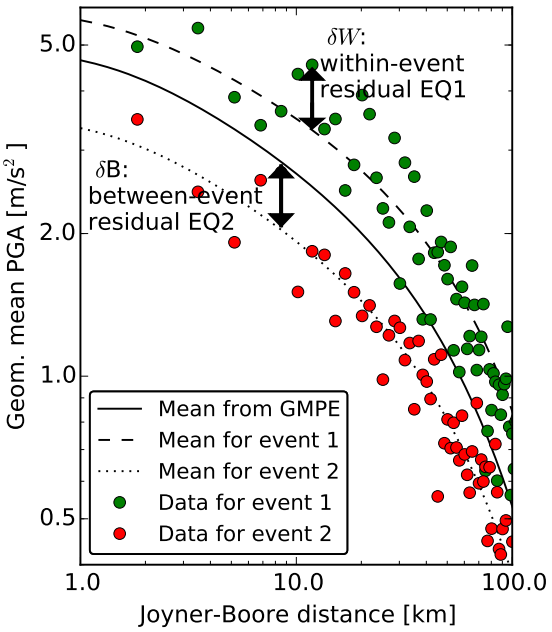

Figure 5.1: Between-event and within-event components of ground-motion variability (after Strasser et al., 2009). The data shown is for two events having the same magnitude, which is also the magnitude used to calculate the median of the predictive equation. The between-event variability, τ , characterises the scatter of the between-event residuals, δ_B (one residual per earthquake). Similarly, the within-event variability, ϕ , characterises the scatter of the within-event residuals, δ_W (several residuals per earthquake).

the aleatory uncertainty in ground motion prediction: researchers may identify variability which is repeatable rather than purely random, thereby moving it to the epistemic uncertainty.

Uncertainty in ground motion is usually distinguished into between-event and within event variability (Atik et al. (2010)). As illustrated in Figure 5.1 the within-event variability ϕ is calculated from the distribution of within-event residuals δW – the shift of the individual ground motion records from the mean ground motion level of a single earthquake. The within-event variability is determined as the standard deviation of all residuals of one earthquake. For the whole dataset with multiple earthquakes, it is the mean of those standard deviations. The between-event residual δB is the deviation of the mean ground motion level of a particular earthquake from the mean ground motion level for earthquakes of the same magnitude. Hence, there is only one residuum per earthquake and the between-event variability τ is calculated as the standard deviation of the distribution of all mean ground motion levels at a specific distance. The between-event and within-event residuals are not correlated, hence, the overall ground motion variability σ is defined as

$$\sigma = \sqrt{\tau^2 + \phi^2}. \tag{5.1}$$

Since the within-event residuals are due to the same rupture process but connected to ground motion at different sites, the within-event variability is dominated by varying site effects and wave paths, as well as the radiation patterns. The between-event residuals indicate differences in ground motion due to different rupture processes and hypocentre-station configurations. It should therefore be sensible to stress heterogeneities and different average stress levels for distinguished ruptures, and to different frictional properties along the faults.

Investigations on the influence of certain source parameters on the resulting ground motions have already been conducted. For example, Aagaard et al. (2001) studied the sensitivity of ground motion with respect to fault depth, rupture speed, maximum slip rate and average slip. Graves et al. (2008) showed that a reduction of rupture velocity along the San Andreas fault causes a significant reduction in ground motion amplitude. Olsen et al. (2008) displayed the influence of slip heterogeneity and the resulting incoherence of the wavefield, which led to a reduction of ground motion extremes. Only few studies systematically quantified the influence of uncertainties in source parameters on the ground motion variability. For example Ripperger et al. (2008) used dynamic rupture simulations to quantify the variability due to stress heterogeneity and variable hypocentre location. Ameri et al. (2011) showed the variability in ground motion resulting from a series of kinematic scenario simulations with variations of several source parameters. However they did not address the variability caused by single source parameters.

As suggested by Baumann and Dalguer (2014) the inclusion of source parameters in the source term of empirical relationships could reduce the standard deviation of GMPEs, as long as the source parameters are indeed observable. However, since various parameters are not observable and also not predictable (e. g. the position of the hypocentre on the fault), the ground motion variability due to this variability needs to be investigated and adequately incorporated in the hazard analysis.

In the following I will discuss the variability in ground motions due to different source parameters and scenarios. I will investigate which source uncertainties have the largest impact on the simulated ground motion and whether these reflect the natural observed variability of ground motions. Furthermore I will verify whether the variability in simulated ground motion due to the observed range in energy magnitudes is comparable to the observed ground motion variability. Using a simple halfspace model for all stations, the within-event variability shown is only dependent on the radiation pattern and directivity effect, while site and path effects do not add to it. On the other hand, the simple earth model allows for the investigation of between-event variability due to source variability without any influence of the variability due to propagation effects.

5.2 Model setup

For investigating the influence of different source parameters on the resulting ground motion, I performed scenario simulations for an arbitrary strike slip fault. The seismograms

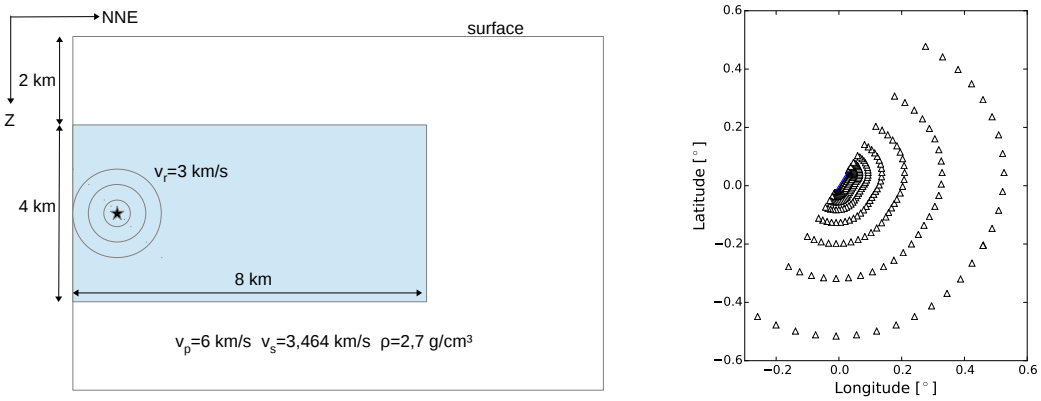

Figure 5.2: Model setup for the scenario simulations. **Left:** Halfspace with location of the fault. **Right:** Station distribution around the fault. 35 stations are placed at each distance for distances of 1.0, 1.6, 2.7, 4.5 and 7.4 km. At 12.3, 20.3, 33.6 and 55.5 km distance, there are 33, 31, 29 and 27 stations, respectively.

are calculated for a pure halfspace problem, such that the variability in the observations is generated by the source only. The model setup is specified in Figure 5.2. Green's functions are calculated on a grid of 70 m grid spacing. To avoid that one component of the ground motion shows a nodal plane, the fault is not aligned with one of the horizontal axes of the coordinate system, but rotated by 30° . The fault is vertical and right-lateral slip occurs with a constant rupture speed of v_r=3 km/s. The seismic moment is $1.0 \cdot 10^{18}$ Nm and the assumed energy magnitude $M_e = 6.0$.

This example of a rather small earthquake is chosen mainly because of the computation time, as larger rupture planes also require more computational resources. However, effects of an extended fault are already clearly visible, for example strong directivity effects. Seismograms are calculated at 9 different distances from the surface projection of the fault, with receivers approximately evenly distributed around the fault for each distance (station locations are shown in Fig. 5.2).

The influence of the following parameters on the ground motion and its variability are assessed:

- the energy magnitude M_e
- the hypocentre location
- the roughness of the fault surface (i. e. the variability of fault mechanisms along the fault)
- the slip distribution
- the rupture velocity v_{rup}.

5.3 Calculation of PGV variability

For each scenario series, 200 simulations are performed. Since the model is designed such that there are discrete distances, mean ground motion intensity measures and their variability can be estimated as a function of distance from the fault. For now I will refer to PGV as the ground motion intensity measure, but the principle can be equally applied to all other scalar measures. The total standard deviation σ will be calculated as the standard deviation of the PGV distribution of all scenarios per series at all stations at the same distance. The within-event standard deviation ϕ will be calculated separately for each scenario as the standard deviation of PGV at the same distance. Hence, for each scenario one within-event standard deviation at each distance is obtained. The overall within-event standard deviation is than computed as the mean of all those single-scenario within-event standard deviations. The between-event standard deviation is calculated from 200 between-event residuals, which are the differences between the mean PGV for all scenarios at one distance and the mean PGV for each single scenario at the same distance. This calculation is rather simple and may be compared to two-stage regressions formerly used for the development of GMPEs.

Relation to regression algorithms

During the regression of empirical data for GMPEs, the components of variability are also determined. Currently, random effects or mixed effects regressions are employed for the estimation of between-event variabilities and within-event variabilities or even station-to-station variabilities. Those algorithms are preferable over traditional regression approaches like the one introduced by Joyner and Boore (1981), as they avoid bias in case of unbalanced datasets. When several earthquakes are recorded at a very small number of locations, the two-stage regression (Joyner and Boore, 1981), which first tries to minimise the within-event-variability, will push more variability to the between-event term than to the within-event term. In the extreme case of one station per earthquake this approach would minimise the within-event term by setting it to zero and assign the whole residual to the between-event term. Hence it would overestimate the between-event contribution and underestimate the within-event contribution. Algorithms later described by Brillinger and Preisler (1984) and Abrahamson and Youngs (1992) use a one-stage approach which splits the total residual into within-event and between-event terms in a more meaningful way. Finally the most recent algorithms, e. g. Stafford (2014), make use of the mixed-effects model, in which each explanatory variable enters into a vector of fixed effects which describes the expected value but also into a vector of random-effects which explain the variability. These more complex models are less sensitive to the number of stations per earthquake and distribute the overall variability in ground motion more appropriately into its between- and within-event contributions.

Since the synthetic experiment shown here was designed to have a good spatial coverage and every event has the same large number of records, the results using the simple

calculation of variabilities should be approximately the same as for the more sophisticated mixed-effects calculation. For comparison, I additionally show the results from a mixed regression performed with the NLMER package of Bates et al. (2014) in one example in Fig. 5.7.

Choice of PGV as intensity measure

Although most existing empirical relationships are established for peak ground acceleration or spectral acceleration, here, I will show the results for peak ground velocity (PGV). Firstly, PGV as a scalar intensity measure is easy to analyse and the results can be compared to existing empirical relationships. Secondly, it has proven to be an intensity measure which is well correlated with damage. Boatwright et al. (2001) showed that on a regional scale PGV was better correlated with intensity than PGA or spectral acceleration at discrete frequencies for the Northridge (1994) earthquake, but equally well correlated as average pseudo-velocity response spectra. Best correlation of PGV with intensity was also found by Kaka and Atkinson (2004) and Akkar and Özen (2005) and at intensities higher than 7 by Wald et al. (1999).

Another argument for employing PGV is that the frequency range of the simulations is still limited. The cutoff-frequency, which determines the frequency after which the signal is low-pass filtered in order to avoid aliasing, will influence the maximal values reached in velocity or acceleration. In general, PGV is less strongly influenced by high frequencies than PGA. I tested this by performing simulations with different cutoff-frequencies and determining the resulting PGA and PGV values as shown in Figure 5.3. The figure shows the dependence of PGA and PGV on the cutoff-frequency for randomly selected stations. I found that, indeed, for a number of stations PGV reaches a stable level for smaller cutoff-frequencies than PGA. This seems to be more often the case for stations in forward directivity than for stations in backward directivity. At a cutoff-frequency of 10 Hz, PGV is almost always saturated. Therefore, I consider it acceptable to use PGV as the scalar intensity measure for the following analyses. Nonetheless, although PGA saturates generally at higher frequencies than PGV, it is also saturated around 10 Hz, here.

5.4 Ground motion variability due to source roughness

As described in Section 3.1.2, the topography of natural faults can be described as a self-similar fractal distribution with the amplitude of the topography increasing with the considered wavelength. According to Mai and Beroza (2002) the power spectrum $P(k)$ of a fractal medium in two dimensions can be written as

$$P(k) \propto \frac{1}{(k^2)^{4-D}} \tag{5.2}$$

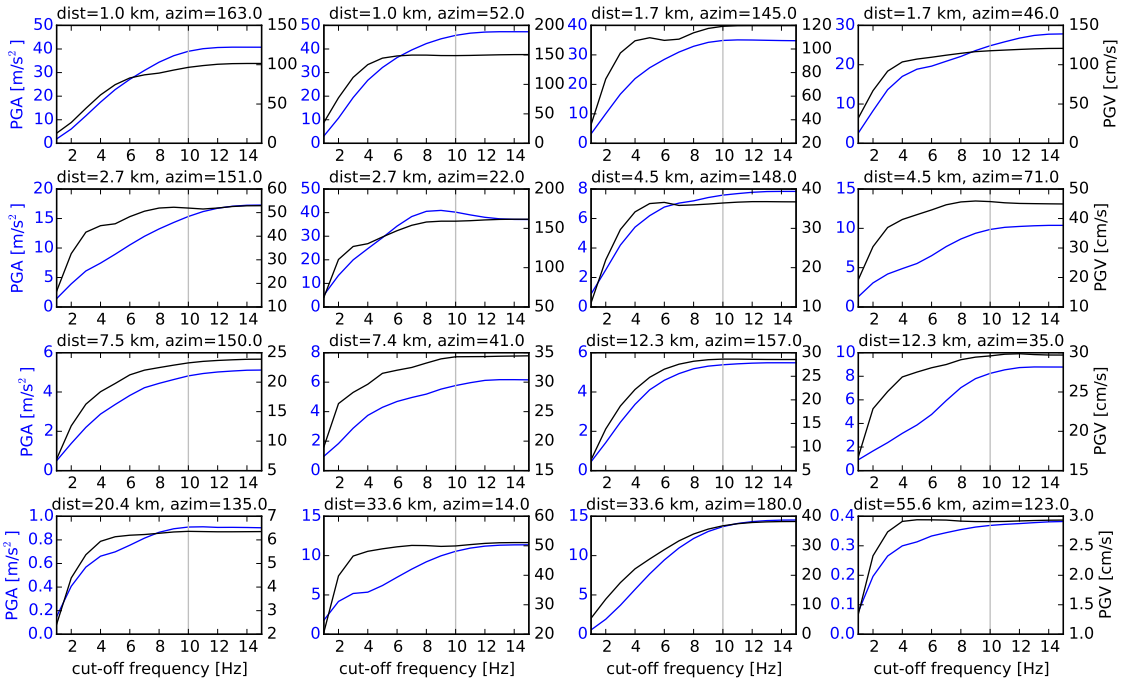

Figure 5.3: Dependence of PGA (blue, left Y-axis) and PGV (black, right Y-axis) on the cutoff-frequency used for the synthetic seismograms. The title specifies the Joyner-Boore distance of the station and the angle between the line connecting the station with the centre of the surface projection of the fault and the strike direction of the fault. This means small azimuths for stations in forward directivity and and large azimuths for stations in backward directivity. The grey vertical line at 10 Hz shows the cutoff-frequency used in the following simulations.

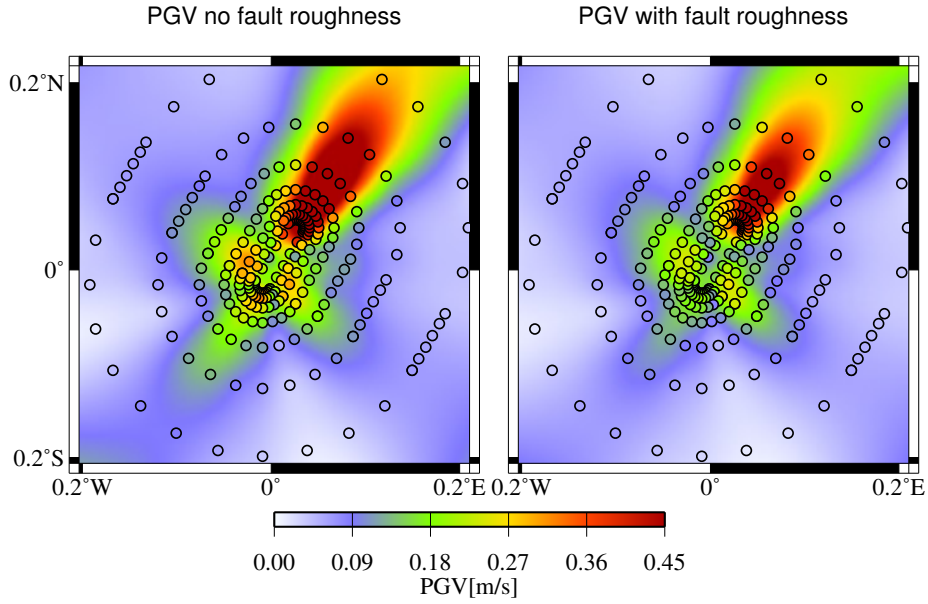

Figure 5.4: Left: Geometric mean of PGV modelled under the assumption of a planar fault with identical fault mechanism for all subpatches. Circles indicate positions at which ground motion was simulated. Colours indicate interpolated PGV. **Right:** Geometric mean PGV modelled assuming a maximum fault topography of $0.1 \cdot 4\,\text{km}$=400 m and projecting the resulting variations in strike and dip onto a planar fault.

with

$$D = E + 1 - H \tag{5.3}$$

where D is the fractal dimension, E is the Euclidean dimension of the fractal medium, and H is the Hurst exponent. In the case of a plane with $E = 2$, the fractal dimension is $D = 3 - H$, and the power spectrum of the measured fault roughness is proportional to $1/(k^2)^{1+H}$. Hence the Fourier Transform of the two-dimensional field of fault topography should be proportional to $k^{-(1+H)}$. Studies of Candela et al. (2012) and Renard et al. (2013), show that the parameter $\alpha = 1 + H$ is approximately 1.8, corresponding to a Hurst-exponent of 0.8. However the maximal height of the fault topography seems to be dependent on the maturity of the fault and is rather variable. Therefore I tested the variability of ground motions due to different topography height, which is defined by the aspect ration β – the ration between topography height and the width of the fault.

As stated in Section 3.1.2, in the approach presented here, there is no real topography on the fault plane but variations in strike and dip mimic the variations which would occur if the fault plane was indeed rough. Figure 5.4 shows the pattern of geometric mean of PGV resulting from a completely planar fault with identical source mechanisms for all subpatches compared to a fault with assumed aspect ratio of 0.1. In the two cases all

other parameters are identical. The hypocentre is placed at 2 km from the southernmost edge of the fault and 3 km from the top of the fault. The slip is uniform with constant rupture velocity. Consequently, the ground motion from the fault without roughness is only characterised by the radiation pattern and the directivity effect. For the rough fault, the radiation pattern as well as the directivity effect are still evident, but those are diminished. PGV for stations in the southwest and northeast of the fault is smaller than in the case without roughness. Stations placed northwest or southeast of the fault also experience a reduction in PGV, but not to the same degree. Hence the difference in PGV between stations at the same distance but in the northeast and northwest of the fault is smaller in the case of a rough fault. This causes within-event variability to become smaller with increasing roughness.

To quantify the variability due to the roughness of the fault, 4 different aspect ratios were tested, ranging from $\beta = 0.1$ to $\beta = 0.01$. For each aspect ratio 200 simulations with different topography distributions but otherwise identical source parameters have been performed. Figure 5.5 shows the mean and standard deviation of PGV versus Joyner-Boore distance. The mean of PGV is almost independent of the aspect ratio. The standard deviation of PGV however is slightly increased for lower aspect ratios. If this standard deviation is split up into its components of within-event and between-event standard deviations, the clear dominance of within-event variability is revealed, while the between-event variability contributes a minor part only. Smaller aspect ratios cause an increased within-event variability in PGV due to stronger effects of the radiation pattern. Larger aspect ratios smooth the radiation pattern and, therefore, reduce the within-event variability. For all simulation series, it is evident that the within-event variability is higher for larger distances while it is significantly lower at small distances to the fault. To compare the variability simulated through fault roughness to observed variabilities, I also plotted the results of four different GMPEs: The regression of Bindi et al. (2014) using Vs30, Derras et al. (2014), Campbell and Bozorgnia (2008) and Chiou and Youngs (2008). Bindi et al. (2014) and Derras et al. (2014) derived equations for geometric mean PGV and use the Joyner-Boore distance for the distance metric. Campbell and Bozorgnia (2008) and Chiou and Youngs (2008) use the orientation-independent ground motion measure GMRotI50 defined by Boore et al. (2006). However, Beyer and Bommer (2006) found that GMRotI50 does not result in a change of the aleatory variability of residuals. Therefore, the standard deviations found for GMRotI50 are shown here along with the results for the geometric mean of the two horizontal components. The standard deviation of all within-event PGV variability found by simulation series with different aspect ratios ranges between 0.45 and 0.55 for Joyner-Boore distances smaller than 5 km, which is close to the rather small values found by Campbell and Bozorgnia (2008) and Chiou and Youngs (2008). The within-event variability increases with increasing distance from the fault up to 0.7 to 0.75, which is close to the high values found by Bindi et al. (2014). The strong distance dependence of the within-event variability due to radiation pattern and directivity effect is not evident in the GMPEs due to the homoscedastic assumption, i. e. because the regression algorithms

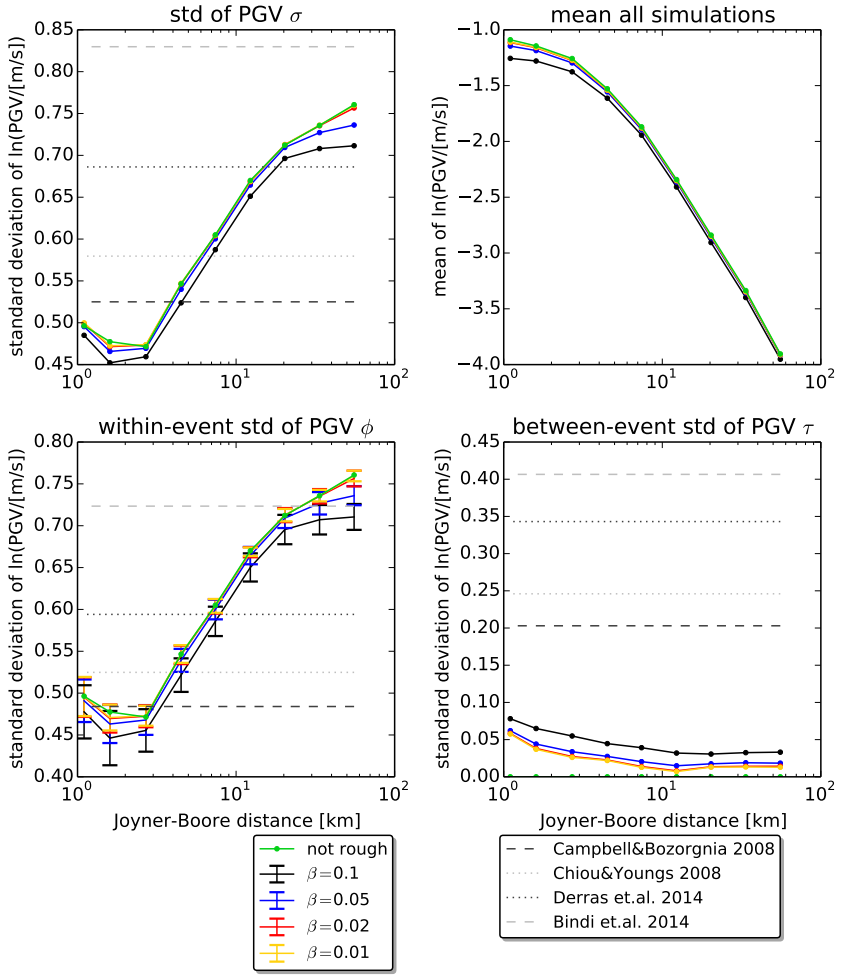

Figure 5.5: Top left: Standard deviation of all modelled PGV versus Joyner-Boore distance. Coloured lines show different aspect ratios. The green line indicates the standard deviation for a single simulation with no roughness. Grey dotted and dashed lines indicate the standard deviations obtained from the regression analyses of Bindi et al. (2014); Campbell and Bozorgnia (2008); Chiou and Youngs (2008); Derras et al. (2014). **Top right:** Mean PGV of all simulated events at all stations versus Joyner-Boore distances. **Bottom left:** Within-event standard deviation for different aspect ratios (coloured lines) compared to within-event standard deviation of GMPEs. Standard deviations for all records at one distance from the same event was calculated and the mean of those standard deviations from all events has been plotted. The error bars show the standard deviation of within-event standard deviations. **Bottom right:** Between-event standard deviation for different aspect ratios (coloured lines) compared to between-event standard deviation of GMPEs.

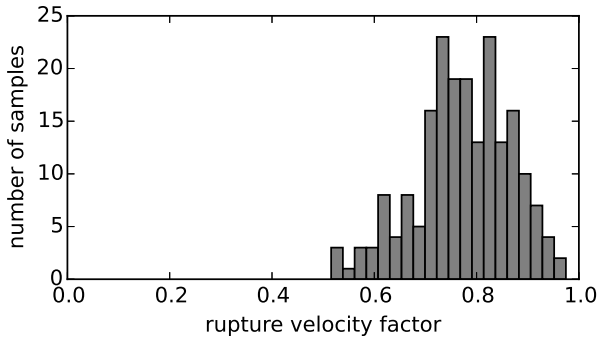

Figure 5.6: Histogram of ratios between shear wave velocity and rupture velocity.

assume that standard deviation is the same at for all distances. The influence on the between-event variability is less strong. However, there is also only limited data available for distances smaller than 5 km, such that empirical relationships cannot make reliable predictions at these near-fault distances. For all aspect ratios, the between-event standard deviation is very small and well below all values found by the regressions.

Overall, the roughness of the fault mainly effects the radiation pattern and thereby the within-event variability of ground motions. The difference in mean PGV between events with different fault topography is neglectable. Hence the between-event variability only gives a minor contribution to the overall standard deviation.

Unfortunately, from this study there is no indication, which aspect ratio is appropriate to simulate realistic fault roughness. The within-event variability decreases by a small amount for increasing aspect ratio. However its does not converge to a certain value and the differences in ground motion characteristics due to fault roughness are very small. The choice of the aspect ratio for the following investigation is somewhat arbitrary. If the fault is considered rough, I will use an aspect ratio of $\beta = 0.05$.

5.5 Ground motion variability due to increasing source variability

In order to characterise the changes induced when varying other source parameters, I performed simulations with all source parameters fixed but one. The variable parameters are

- **the energy magnitude:** the values are chosen from a Gaussian distribution with mean 6.0 and the standard deviation $\sigma = 0.24$ obtained from the empirical dataset shown in Fig. 3.4
- **the hypocentre:** hypocentres are placed randomly in the rupture area
- **the rupture velocity:** the ratio between the shear wave velocity and the rupture velocity is varied between 0.5 and 0.98, with the histogram of ratios shown in Fig-

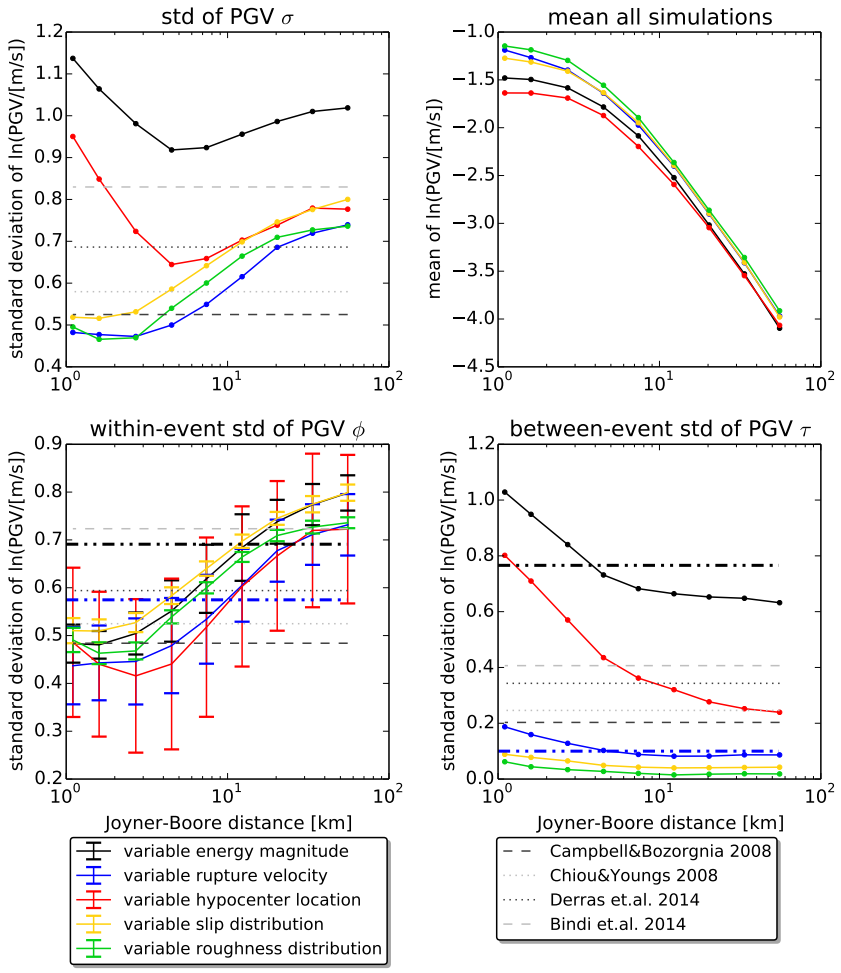

Figure 5.7: Same as Fig. 5.5 but with different coloured lines showing results for simulation series with different variable parameters. Dash-dotted lines additionally show the results of the regression of the simulated data by the NLMER package of Bates et al. (2014).

ure 5.6. The shear wave velocity has the same value for all simulations, only the rupture velocity is varied. Here, the rupture velocity stays constant along the fault.

- **the distribution of slip:** the slip is distributed differently for each simulation, while the total seismic moment stays constant

Figure 5.7 shows the mean PGV, its standard deviation and the within-event and between-event components thereof versus Joyner-Boore distance. The mean value of within-event standard deviations ϕ for the different cases of parameter variations are quite similar. Compared to the case where the roughness distribution is variable only (shown in Section 5.4), the within-event variability is slightly higher if the slip distribution or the energy magnitude are variable. If the hypocentre location is varied, hypocentres positioned closer

to the centre of the fault lead to smaller within-event residuals and the average within-event standard deviation is slightly smaller than for the other simulation series. A similar argument can be applied to the case of varied rupture velocity: for the simulations presented in Section 5.4 the rupture velocity factor was 0.86. In the simulation series with varied rupture velocity, the majority of factors are smaller, leading to smaller rupture speeds. This in turn leads to a reduction of the directivity effects and, consequently, to smaller within-event variability.

The standard deviation of within-event variability is more strongly dependent on the variable parameter than the mean within-event variability itself. When only the roughness distribution is variable, the standard deviation of within-event variability is smallest, less than 0.02, indicating approximately the same within-event variability for all the scenario simulations of one parameter case. The standard deviation for ϕ is larger, if the slip distribution is varied in each scenario and even larger if the rupture velocity or energy magnitude are varied. Highest standard deviations of ϕ are found if the hypocentre is varied. This means, that for certain positions of the hypocentre with respect to the centre of the fault the within-event variability is rather small, while for other scenarios it is very large.

The between-event standard deviation is smallest if only the roughness distribution is varied. It is slightly increased if the slip distribution is variable within the simulation series and further increased if the rupture velocity is variable. However, the between-event standard deviations for these three cases are all smaller than all the values obtained from the empirical relationships shown for comparison in Figure 5.7. Rather high values of between-event variability are found for small distances from the fault for the simulation series with variable hypocentres. At small distances these values are higher than the one obtained from GMPEs, but the variability for my simulations shows a strong dependence on distance. The between-event standard deviation assumes a value at Joiner-Boore distances larger than 10 km which is in between the levels found by the different GMPEs. A very high between-event variability at small distances obtained from the variation of the hypocentre location indicates that either the distribution of hypocentres is not similar to the locations which occur in nature or that the effect occurring in the simulations of extreme hypocentre location are in nature mitigated by other effects. On the other hand, the validity of results from GMPEs is debatable at these small distances, as datasets are limited. The influence of the hypocentre location on the ground motion is further investigated in Section 5.5.1.

Highest between-event variability is found if the energy magnitude is varied. At all distances the ground motion variability is much higher than the variability in observed data. Hence, either the observed variability in energy magnitude as obtained from the data in Fig. 3.4 is too high or the variations in rise time introduced by the scaling to the energy magnitude are too large. In the first case, the uncertainty could probably be reduced, if the station distribution was better and more stations per earthquake were available for a more stable determination of energy magnitude. Additionally, estimates in

energy magnitudes might be improved if better corrections for path and site effects were made, which would for example require more detailed attenuation models or the correction of site-specific attenuation. Still, it is not clear whether those improvements would really lead to a smaller range of energy magnitudes for the same moment magnitude. The second possibility is that the variations in rise time due to the scaling proposed in Sec. 3.2.2 could be too high. This might be the case if the formulation of Equation 3.12 does not correctly describe the energy radiated from the source. Eq. 3.12 is based on Haskell's model (Haskell, 1964) which is a simplified earthquake model based on the assumptions that the rupture propagates unilaterally, slip occurs instantaneously in the direction normal to the rupture propagation and slip at the border jumps from the average slip to zero. Since all of these are oversimplifications with respect to the natural processes, Eq. 3.12 might also be too general and modifications regarding the fault geometry and slip distribution could improve the energy calculation.

In Figure 5.7 the results are compared to a regression performed with the NLMER software of Bates et al. (2014) for the series with variable energy magnitude and variable rupture velocity. This is a mixed effects regression, the results of which should be generally independent of the station configuration. However, it assumes homoscedasticity, i. e. the standard deviation is the same for all distances. In comparison to the findings described above, this regression returns approximately average values of within-event and between-event standard deviations for both simulation series.

5.5.1 Ground motion variability due to hypocentre location

Since Figure 5.7 showed that the between-event and within-event variability is strongly dependent on the hypocentre location and especially the between-event variability is higher than the values obtained by regression of empirical data, it is worth taking a closer look at the residuals related to different hypocentre locations.

Figure 5.8 a shows the dependence between the within-event standard deviation for each scenario at a distance of 12 km and the hypocentre location. For a fault with uniform slip and no variations in strike and dip the variability within the same event is higher the nearer the hypocentre is placed towards the edges of the fault along strike. It also increases with the depth of the hypocentre. This is caused by the stronger directivity effect occurring if the rupture initiates along the edges of the fault. In case of distributed slip along the fault (Fig. 5.8 b), the results are similar at first glance, but the within-event standard deviation is even more strongly dependent on the hypocentre location. The variability of PGV is larger if the rupture propagates towards the region of high slip, such that the slip maximum is in forward directivity. This causes the already high ground motion in forward directivity to increase even more, leading to larger within-event variability. If the rupture propagates away from the region of high slip, merely the ground motions in backward directivity are enlarged, leading to reduced within-event variability. Consequently, the

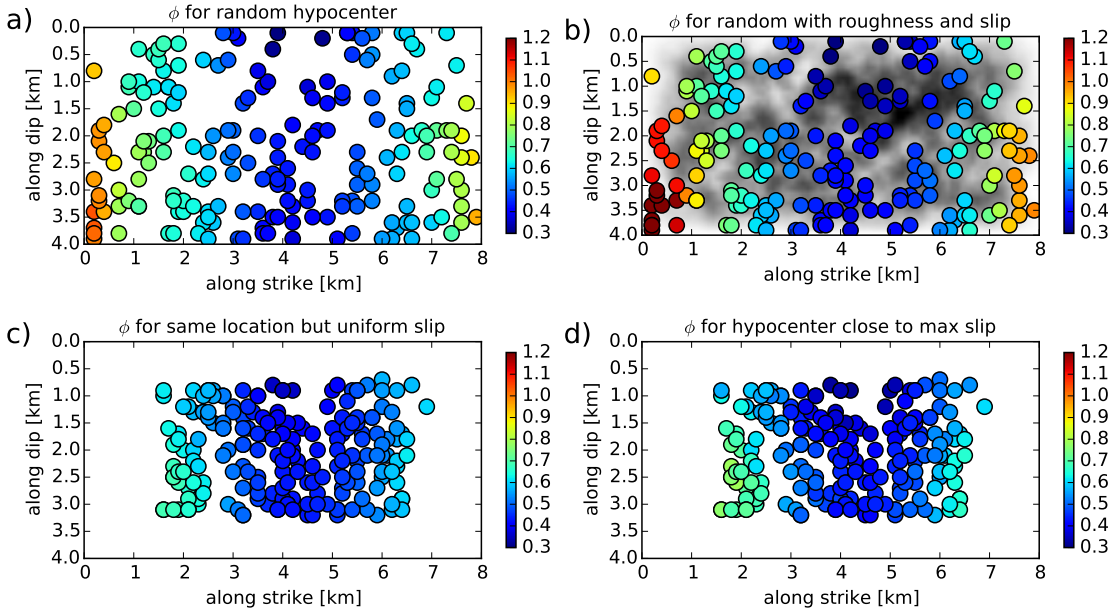

Figure 5.8: Within-event standard deviation of ln(PGV/[m/s]) as a function of the hypocentre location at a station distance of 12 km. The dots indicate the position of the hypocentre along strike and dip of the fault for every single simulation. The colours refer to the within-event standard deviation for each single event. **Top left (a):** Results for random hypocentre locations on a fault without variations in slip, strike and dip. **Top right (b):** Results for random hypocentre locations on a fault with variations in slip, strike and dip. The distribution of slip and roughness is the same for each scenario of this simulation series. The maximum slip is at approximately 5 km in strike and 1.5 km in dip direction. The underlying grey scale visualises the slip distribution, with darker colours indicating higher slip. **Bottom right (d):** Results for the hypocentre located at the closest point to the maximum slip location with slip of $0.5 \cdot \max(\text{slip})$. The roughness and slip distribution are varied for each scenario, such that the slip maximum is located at different places. Consequently, also the hypocentre, which is close to the maximum slip, is located at different places. **Bottom left (c):** Same location as before in (d) but on a fault with uniform slip and no variations in strike or dip.

spread of within-event variabilities is higher for the fault with distributed slip than for the fault with uniform slip.

Manighetti et al. (2005) found from a database of 76 inverted slip models that the rupture tends to nucleate close to the region of maximum slip and they suggest that the distance between maximum slip and the hypocentre measures the size of the main asperity. Following this suggestion I performed a series of simulations with varied distributed slip with the hypocentre being placed at the location closest to the maximum slip where the slip amounts to 1/2 of the maximum slip (Fig. 5.8 d). This means that the slip distribution is different for each scenario in the simulation series. Hence, the maximum slip is located at a different place for each scenario and the closest point at which the slip is reduced to the half of the maximum value is also dependent on the scenario's slip distribution. Consequently

the hypocentre location is variable for each scenario. Due to the slip distribution being tapered towards the edges of the fault, almost none of the hypocentres is now placed close to the fault edges. Scenarios with strong within-event variability do not exist and the distribution of within-event standard deviations is narrowed. Here, the hypocentre being close to maximum slip only contributes a small effect, while the coincidence of the hypocentres not being located close to the margins of the fault contributes the most. This is shown if a series of simulation is calculated with the same hypocentre location but uniform slip (Fig 5.8 c). The within-event variabilities are nonetheless smaller, as no hypocentres are placed at the edges. These results are also reflected in Figure 5.9 c which shows the within-event standard deviation for these simulation series in dependence of Joyner-Boore distance. Within-event variability is highest if the hypocentre is placed randomly on the rough fault with distributed slip. The distributed slip intensifies the directivity effects if the rupture propagates towards high slip, while it reduces it if the rupture propagates away from the highest slip. This also leads to the strongest variation for the within-event standard deviations for the single scenarios. The within-event standard deviation and its variability among single scenarios is reduced if the hypocentre is placed randomly on a fault without roughness and with uniform slip. If the hypocentres are placed close to maximal slip, the scenarios with hypocentres close to the edges of the fault which exhibit largest directivity effects are no longer included and the within-event standard deviation diminishes. It becomes smaller than the empirical observed values at small distances to the fault and assumes values in between those of different GMPEs at distances larger than 12 km. Figure 5.9 c also shows that this reduction in variability is due to the hypocentres being located away from the edges of the fault and less importantly closer to the maximum slip, since the simulation series which uses the same hypocentre locations on a fault with uniform slip results in almost the same within-event variability.

Figure 5.10 a shows how the between-event residual at stations at a distance of 12 km for each scenario depends on the hypocentre location. It should be stressed that the between-event *residuals* are shown, not the between-event standard deviation. The between-event residuals increase the closer the hypocentre is placed to the edges of the fault and the deeper it is located. Again, this can be attributed to the directivity effects, which do not only change the spatial radiation pattern but also the mean ground motion level for each scenario. The series of simulations performed on a fault with distributed slip and roughness (Fig. 5.10 b) shows that the distributed slip diminishes the influence of the hypocentre location on the mean ground motion level, as the between-event residuals are smaller toward the edges than in the case of the uniform fault. Between-event residuals are also plotted for simulations with variable distributed slip with the hypocentre being placed close to the maximum slip (Fig. 5.10 d). Again this causes hypocentres to be placed further away from the edges and, therefore, large between-event residuals do not occur. The same is true if the hypocentres are located at the same places (Fig. 5.10 c), but on a uniform fault. Figure 5.9 d shows the between-event standard deviations for the four simulation series with different hypocentre locations described. It shows that

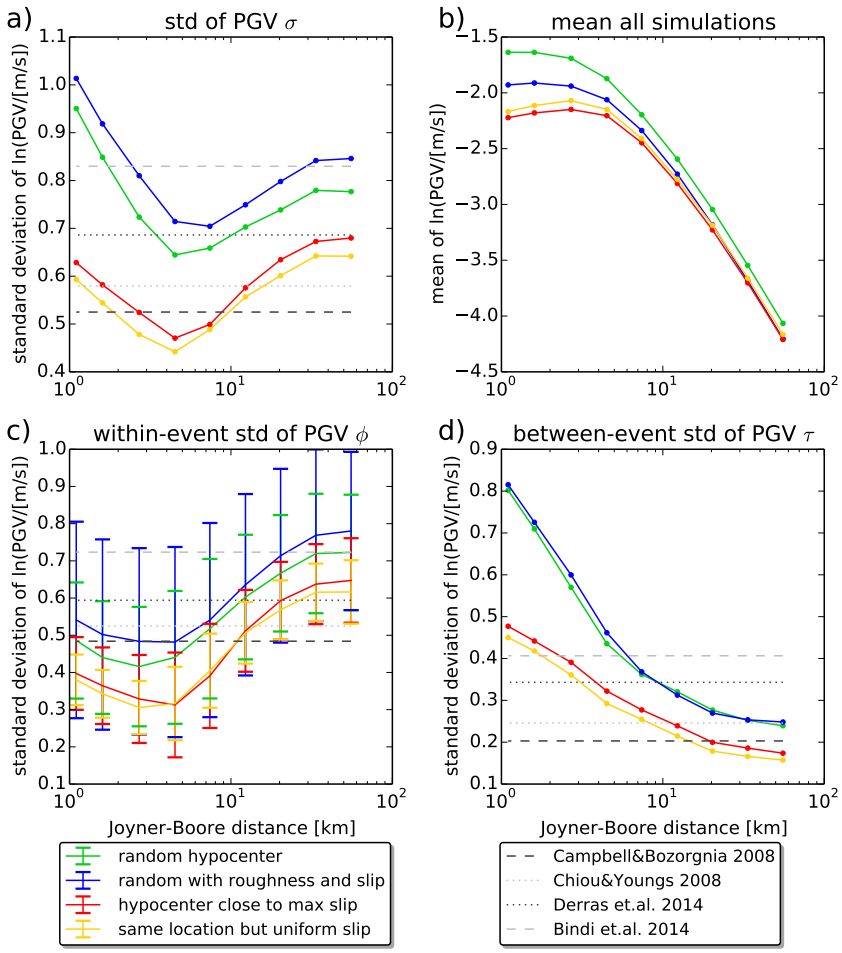

Figure 5.9: Same as Fig. 5.5 but with different coloured lines showing results for simulation series with (a) randomly placed hypocentre on a fault with uniform slip and without roughness, (b) randomly placed hypocentres on a rough fault with distributed slip, (c) hypocentres on rough faults with variable distributed slip, with the hypocentre being placed at proximity to the maximum slip and (d) hypocentres on the same locations as for case (c) but on a fault with no roughness and uniform slip.

scenarios with distributed slip exhibit slightly higher between-event standard deviations than simulation series with hypocentres placed on a fault with uniform slip. For simulation series with randomly places hypocentres, the between-event variability close to the fault is significantly higher than the observed variability. If the hypocentres are only placed away from the fault edges, the between-event variability is smaller, such that for small distances it is close to those GMPEs which found a between-event standard deviation around 0.4 and for large distances it is close to the GMPEs with a τ around 0.2. From my simulation I find again that the between-event variability shows a dependence on the distance from the fault, which opposes the homoscedastic assumption used in the regression of empirical

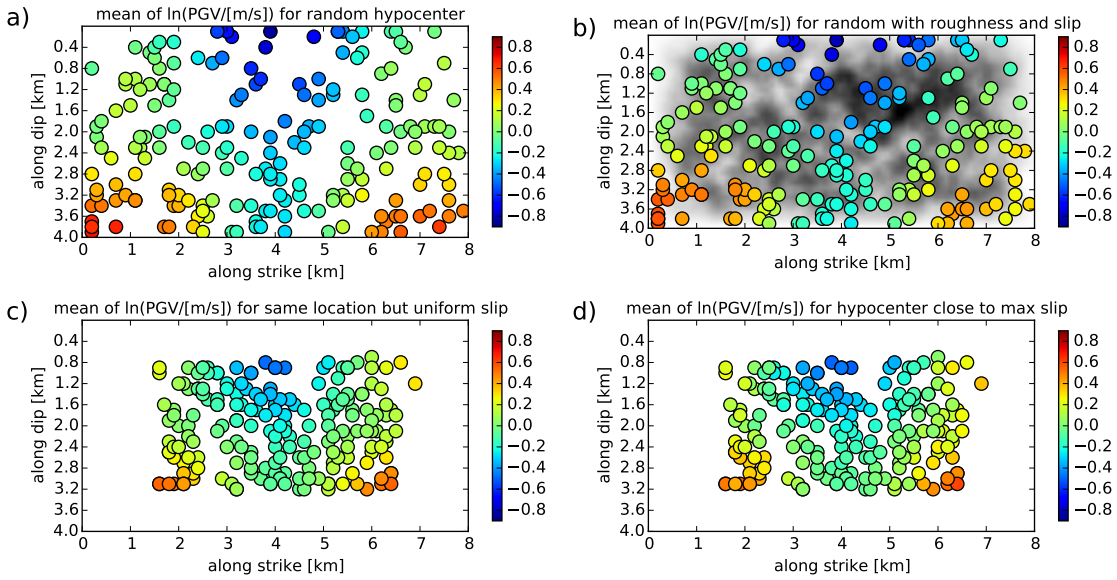

Figure 5.10: Between-event residuals as a function of the hypocentre location. Subfigures (a-d) refer to the same simulation series as in Fig. 5.8. However, here the between-residuals are shown for each single scenario, not the between-event variability.

data. Between-event variability decreases with distance, while within-event variability increases. The total standard deviation as a combination of those two components varies for different distances around the high σ values found by Bindi et al. (2014) and Derras et al. (2014) for the cases of randomly placed hypocentres. It is closer to the lower values obtained by Boore and Atkinson (2008) and Chiou and Youngs (2008) if hypocentres are moved towards the centre of the fault.

This comparison of different options of hypocentre placement reveals the strong influence of the hypocentre locations on the ground motion and its variability, especially at short distances from the fault. In order to limit the variability obtained from synthetic ground motions, we have to determine where the hypocentres are placed relative to the edges of the fault and relative to slip asperities.

5.5.2 Ground motion variability due to energy magnitude

Out of the considered source parameters, the energy magnitude has the strongest influence on the between-event standard deviation and, consequently, on the total standard deviation of PGV. Figure 5.11 shows the between-event and within-event residuals versus energy magnitude for different distances from the source. The between-event residuals are for all distances a monotonous function of the energy magnitude, with higher energy magnitudes resulting in higher residuals. This is what is expected, as higher energy magnitudes result in shorter rise times and stronger ground motion. For Joyner-Boore distances

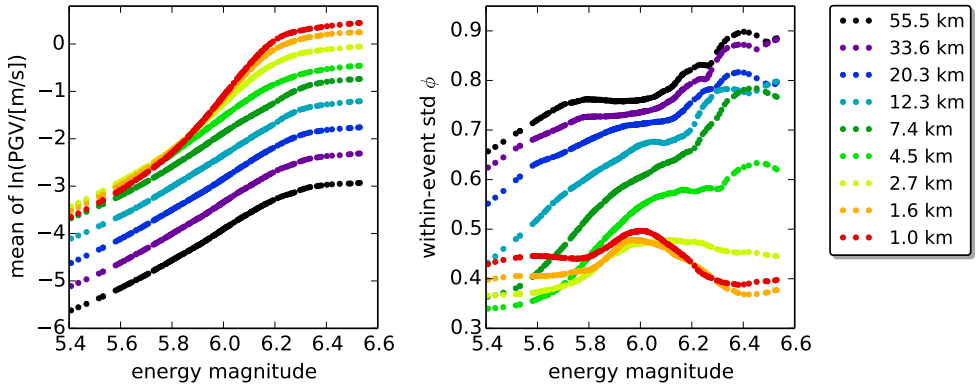

Figure 5.11: Mean (**left:**) and standard deviation (**right:**) of ln(PGV/[m/s]) for each event versus energy magnitude. The colours indicate the distance from the fault. The mean per event relates to the between-event residual, while the standard deviation per event shows the within-event standard deviation for each single simulation.

larger than 4.5 km the relation is nearly linear for energy magnitudes between 5.4 and 6.2. It seems to saturate for energy magnitudes larger than 6.2. However, this might be due to the limited discretisation in time, as the rise times become increasingly smaller and end up with being as small as the sampling frequency. A further increase in the rise time then cannot increase the ground motion level. For very short distances, the slope of the relation between M_e and the between-event residuals is steeper if the energy magnitude is varied around the value of the moment magnitude than if the energy magnitude is more than 0.2 magnitude units smaller or larger than the moment magnitude.

The within-event standard deviations show a less regular behaviour with magnitude. For very short distances, the within-event variability is maximal if the energy magnitude equals the moment magnitude. For distances larger than 3 km the within-event standard deviation increases with increasing magnitudes with the slope being larger for smaller distances. When averaging over all distances, the within-event variability increases with energy magnitude. This would mean that for higher M_e the ground motion increases stronger in places of high shaking than in regions of low shaking.

5.6 Ground motion variability by decreasing source variability

From the modelling point of view, the question of how much variability in ground motion is introduced by varying a certain parameter is interesting to verify the simulation procedure and to make sure that the simulations result in approximately the same ground motion variability as we can observe from natural earthquakes. From the prediction point of view, it would also be interesting to see how much the variability could be reduced if we were able to ultimately predict a certain parameter. For example, if we could predict the

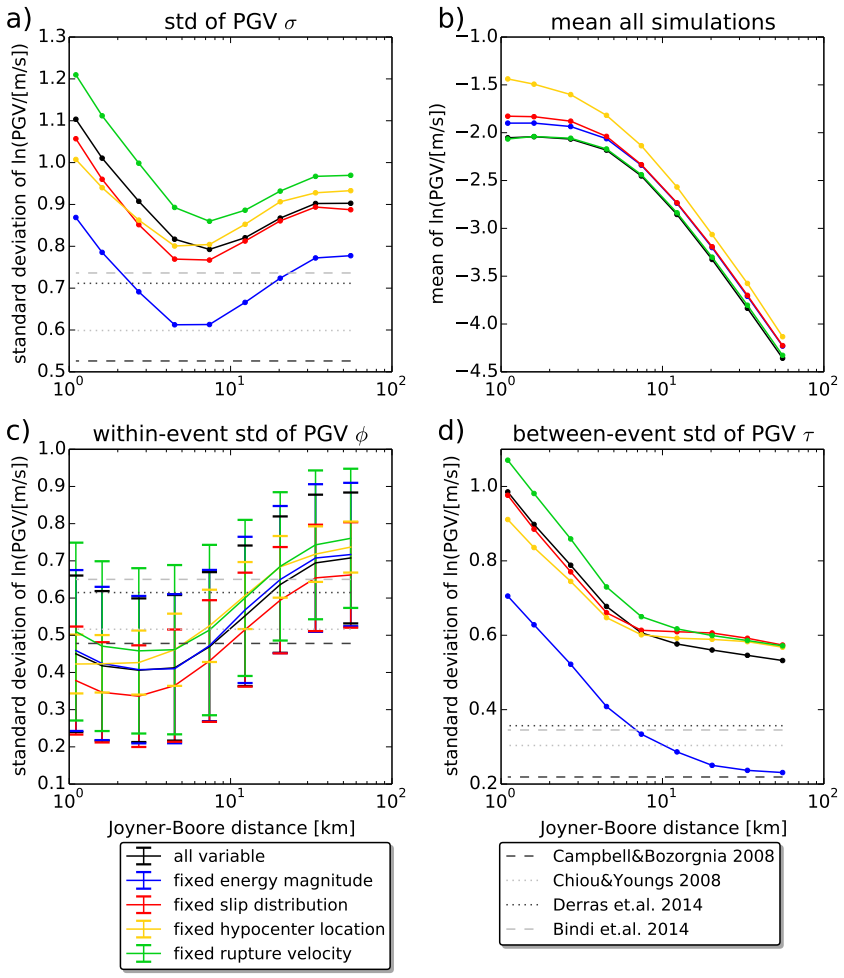

Figure 5.12: Same as Fig. 5.5 but with different coloured lines showing the variability in case of one known parameter, which is fixed while all other parameters are variable.

position of the hypocentre, how much lower would the standard deviation of the predicted ground motion be?

To address this second question, a series of simulations, in which all the parameters used for the source description are variable, is compared to various simulation series, in each of which one parameter is fixed. Intuitively one might expect a reduction of variability if more parameters are fixed. However, Figure 5.12 shows that the interplay of different effects might even lead to an increase in ground motion variability. The total standard deviation is only reduced significantly if we fix the energy magnitude while leaving all other factors variable. Close to the fault, fixing the energy magnitude reduces the total standard deviation by about 0.2, at larger distances the reduction is only approximately 0.12. The within-event variability for fixed energy magnitude is almost the same as for variable M_e. The reduction of the total variability is almost entirely connected

to a reduction in between-event standard deviation. Ground motion variability is also reduced if the slip distribution is fixed. For the series of simulations with the same slip distribution, the within-event variability is reduced at all distances by approximately 0.05. The between-event standard deviation at small distances is not influenced when fixing the slip distribution, while at distances larger than 10 km there is even a small increase in τ by about 0.02. The combination of ϕ and τ to the total standard deviation results in a decrease of σ at distances shorter than 10 km by around 0.05 and almost no change in σ for larger distances.

In contrast, when fixing the rupture velocity both components of the standard deviations increase by 0.02 to 0.05, such that the total standard deviation increases by around 0.08 to 0.1 at all distances. This is mostly due to the relatively high rupture velocity factor of 0.86 chosen here. For the simulation series with varied rupture velocity, on average the rupture velocities are smaller and hence directivity effects are smaller, leading to smaller ground motion residuals between events and within events. If the hypocentre is fixed, similar effects occur: at most distances the within-event standard deviation increases due to the more unilateral rupture propagation when keeping the hypocentre fixed (at 2 km from the left edge of the fault and 3 km from the top of the fault). Clearly, the standard deviation of ϕ is smaller for the fixed hypocentre, which means, that the within-event standard deviation assumes more similar values for the different simulation in the same simulation series. Changes in the between-event standard deviation are small, with a little reduction of the variability close to the rupture and a small increase in τ for distances larger than 10 km.

5.6.1 Dependence of variability decrease on the chosen rupture velocity

Figure 5.13 supports the above findings: it shows the standard deviation σ, and its within-event (ϕ) and between-event (τ) components as a function of the fixed rupture velocity factor used for the simulations for two different distances from the fault (at 55 and 4.5 km Joyner-Boore distance). The standard deviation of PGV and its components all show a clear trend with the rupture velocity factor. A larger factor corresponds to higher rupture velocities, and leads to an increased standard deviation of PGV. At a Joyner-Boore distance of 4.5 km from the fault, the within-event standard deviation rises from 0.35 for $v_{\mathrm{rup}}/v_s = 0.66$ to 0.5 for $v_{\mathrm{rup}}/v_s = 0.96$. At the larger distance of 55 km ϕ is overall higher, but the trend is the same with a rise from 0.6 to 0.82. The between-event standard deviation is also correlated with the rupture velocity factor, with values increasing from 0.61 to 0.73 for the Joyner-Boore distance of 4.5 km. For τ the values are smaller for the distance of 55 km, but again increasing from 0.5 to 0.6. The combination of ϕ and τ leads to an increase in total standard deviation from 0.73 to 0.93 at 4.5 km distance and from 0.83 to 1.04 at 55 km distance.

The relationship between the rupture velocity factor and the ground motion variability is evident. The clear dependence of the within-event variability on the rupture velocity is

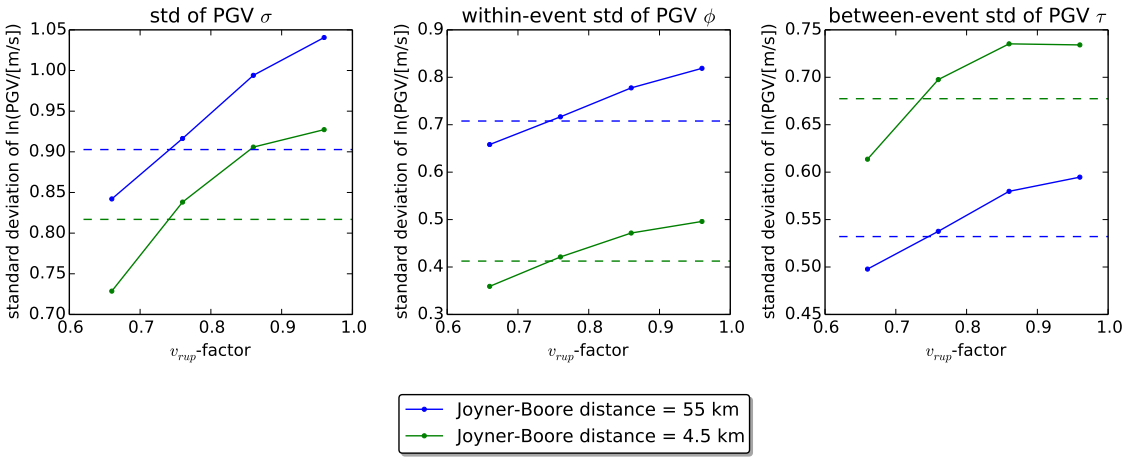

Figure 5.13: Standard deviation σ of ground motion (**left**), within-event standard deviation (**centre**) and between-event standard deviation (**right**) versus the fixed rupture velocity factor used for the simulations while all other source parameters are variable. Two different distances from the fault are shown. The dashed lines indicate the values which were obtained in a simulation series where all parameters were variable.

intuitively understood as higher velocities lead to stronger directivity effects. The increase of the between-event variability with higher rupture velocity is due to the higher rupture velocity intensifying the difference in ground motions resulting from other variable parameters, such as the hypocentre. Overall, the results show, that by constraining the rupture velocity an actual reduction of the ground motion uncertainty can only be achieved, if the rupture velocity is small, or if additional source parameters can also be fixed. Compared to the simulations with a variable rupture velocity, the standard deviation and its components for a fixed velocity are lower only if v_{rup}/v_s is lower than 0.75.

5.6.2 Dependence of variability decrease on the chosen hypocentre location

If the hypocentre is fixed while all other parameters are variable, the change in variability is dependent on the hypocentre location. Figure 5.14 presents the standard deviation of the ground motion and its components in dependence of the location at which the hypocentre is placed. The variability in PGV is larger if the hypocentre is placed closer to the edge of the fault, i. e. if the hypocentre position along strike relative to the top left corner is small. Compared to the case where all parameters are variable, a reduction in simulated variability is achieved if the hypocentre is placed at least at 2 km from the edge along strike direction for a Joyner-Boore distance of 4.5 km. For 55 km Joiner-Boore distance an reduction is achieved only if the hypocentre is placed at 3 km from the fault edge, which means that the rupture propagates mainly bilateral.

The strong correlation between simulated variability and hypocentre location is attributed mostly to the within-event component. For both considered distances, the sim-

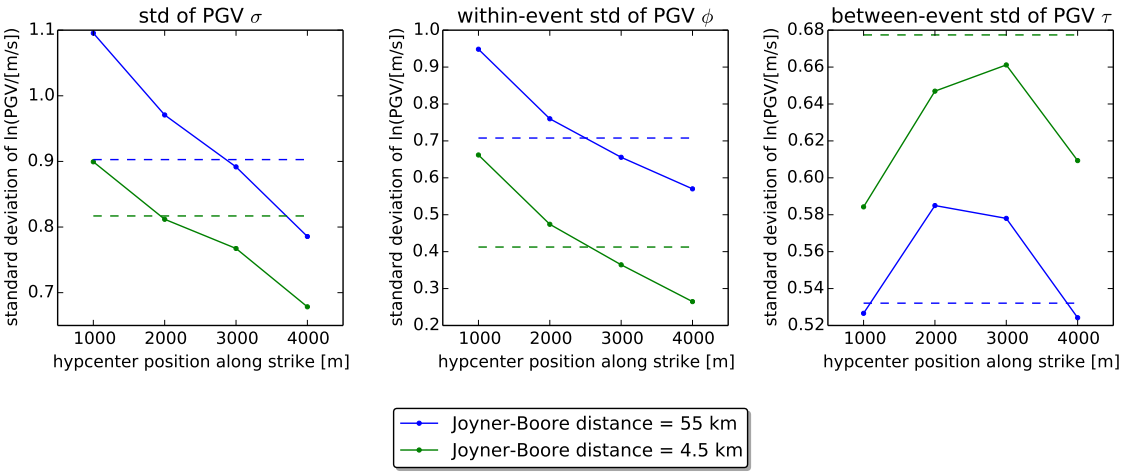

Figure 5.14: Same as Fig. 5.13 but for different fixed hypocentre locations and variable rupture velocity factor. The hypocentre is placed always in 5 km depth but its position along strike is fixed to a different value for each simulation series and the standard deviations and its components are compared for each simulation series.

ulated within-event standard deviation is smaller than in the freely variable case, if the hypocentre is located at more than 2.5 km distance from the edge along strike, i. e. when the rupture propagation is mainly directional.

The effect in between-event-variability due to the hypocentre location is comparatively small: τ changes only by about 0.08, and there is no clear trend with distance from the fault edges. The between-event ground motion is dominated by other source parameters, namely the energy magnitude.

5.7 Discussion

From the point of view of the seismologist who wants to perform a seismic hazard analysis usually the ergodic assumption has to be made in order to analyse existing ground motion datasets. An ergodic process is one in which the statistics of the process computed over time for a single point in space are equivalent to the statistics of the process computed at many points in space for a single point in time. By using synthetic datasets, the ergodic assumption can be removed, as we are able to perform a large amount of simulations for the same site. However for the seismologist who wants to use synthetic seismograms for the prediction of probabilities of exceedance, the mean logarithmic motion and the logarithmic standard deviation are both of equal importance (Stafford, 2014). The study shown here, aimed at the quantification of ground motion standard deviation resulting from the parametric uncertainties connected to the used approach. It showed that the parametric uncertainties in relation to the slip and roughness distribution, the mean rupture velocity and the hypocentre location result in ground motion variabilities which are

comparable to those observed. In contrast, the between-event standard deviation resulting from the variation of the energy magnitude is much higher than the between-event variability found in empirical relationships. This results jeopardises the energy magnitude as a parameter suitable for the characterisation of ground motion. There are two possible explanations: 1) the observed variability on energy magnitude is too large and the estimated radiated seismic energies are over- and underestimated. Or 2) the way of transforming the variation in energy magnitude into a variation in rise time is not correct and the estimated rise times are over- and underestimated. The first explanation calls for a revision of the determination of energy magnitudes and for more sophisticated correction of path and site effects for the calculation of radiated seismic energy. The second explanation calls for a revision of the algorithm used here. The basic assumptions made for the derivation of Eq. 3.12 have to be checked. Pending results of such an investigation, the effects of more complex source descriptions on the energy magnitude have to be taken into account. Cotton et al. (2013) made a similar observation when comparing ground motion variability resulting from synthetic simulations with the stress drop variability observed in seismological source studies to empirical ground motion variability. They equally found that the standard deviation in PGA resulting from the distribution of stress drop is much higher than the standard deviation implied by the GMPEs. They suggested, among other, that the metadata used for the GMPE regressions, such as site characterisations or hypocentre locations, are of better quality for the GMPE developments than for the studies determining stress drops. Additionally, especially for small events, the stress drop calculation could be influenced by the closeness of the κ corner frequency to the event corner frequency, leading to wrong estimation of stress drop. The same argument applies to the determination of energy magnitudes, as made in Sec. 3.2.2: for small moment magnitudes, the effect of the high-frequency attenuation κ on the calculated energy magnitude is stronger, because the second corner frequency (related to κ) is much closer to the first corner frequency (related to the rise time).

This study also revealed a correlation between the ground motion variability and the distance from the fault. For all simulations shown here, the within-event standard deviation increased with distance and the between-event standard deviation decreased with distance. Both results suggest that for sufficiently large datasets a regression should assume that the ground motion variability is not independent from the distance.

5.7.1 Influence of the station configuration

Of course there are numerous factors which influence the resulting variability. For example, the station configuration has to be pointed out. Since the variability is strongly dependent on the radiation pattern and directivity effect, it will also be affected by the station configuration. When a lot of stations are placed in regions with similar ground motion, for example parallel to the fault where directivity effects are smaller, the within-event standard deviation will be minor to the case where stations are placed in areas with spatially

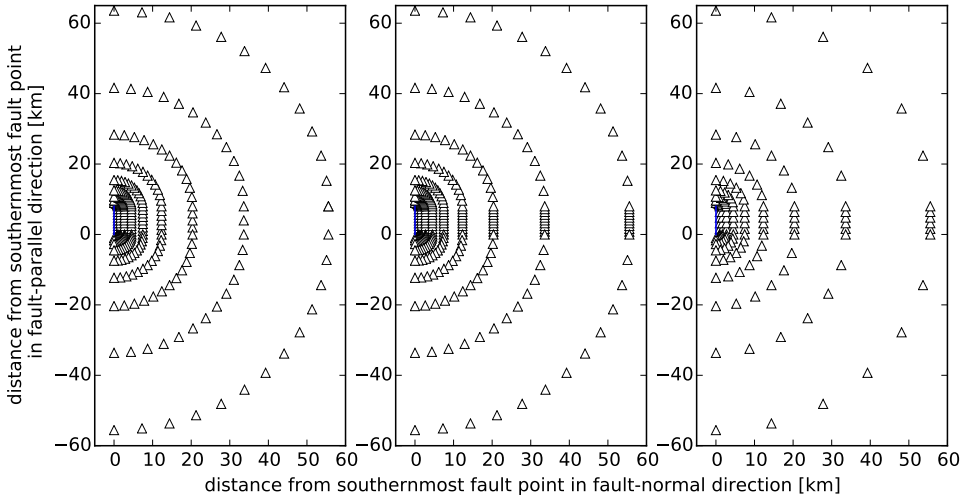

Figure 5.15: The different station configurations used to estimate total, within-event and between-event variabilities for variable energy magnitude. The plot axis are aligned with the fault normal and fault parallel directions for better visibility **Left:** Station configuration used for previous simulation and shown in Fig. 5.2. Stations are approximately evenly distributed. **Center:** Station configuration with 35 stations at each distance with 10 stations parallel to the fault, which leads to a dominant influence of fault parallel stations in the calculation of mean ground motions and their variability. **Bottom right:** Station configuration with 18 stations at each distance, again with a smaller inter-station distance in fault parallel regions for large distances to the fault.

strongly variable ground motion. As an example, Figure 5.16 shows the simulation results in the case of varied energy magnitude for three different station configurations, which are sketched in Figure 5.15. The first station configuration is identical to the one used before. A second series of simulations was performed with 35 stations at each distance. The station locations are the same as before for small distances up to 5 km distance from the fault, with 10 stations placed along a line parallel to the fault. For the larger distances, there are now also 10 station along a line placed parallel to the fault, which leads to a small inter-station distance in this region. Hence, the ground motions at those stations parallel to the fault are similar and the within-event standard deviation is smaller than in the previous case with approximately the same inter-station distances between neighbouring stations. This does not only apply to the within-event standard deviation, but also to the between-event standard deviation. The change in energy magnitude seems to affect the regions parallel to the fault less than the regions in forward or backward directivity. The mean ground motion is now dominated by the more stable values at the fault-parallel stations and, therefore, between-event residuals are smaller. Consequently, the total standard deviation at larger distances is also smaller than in the case with evenly distributed stations.

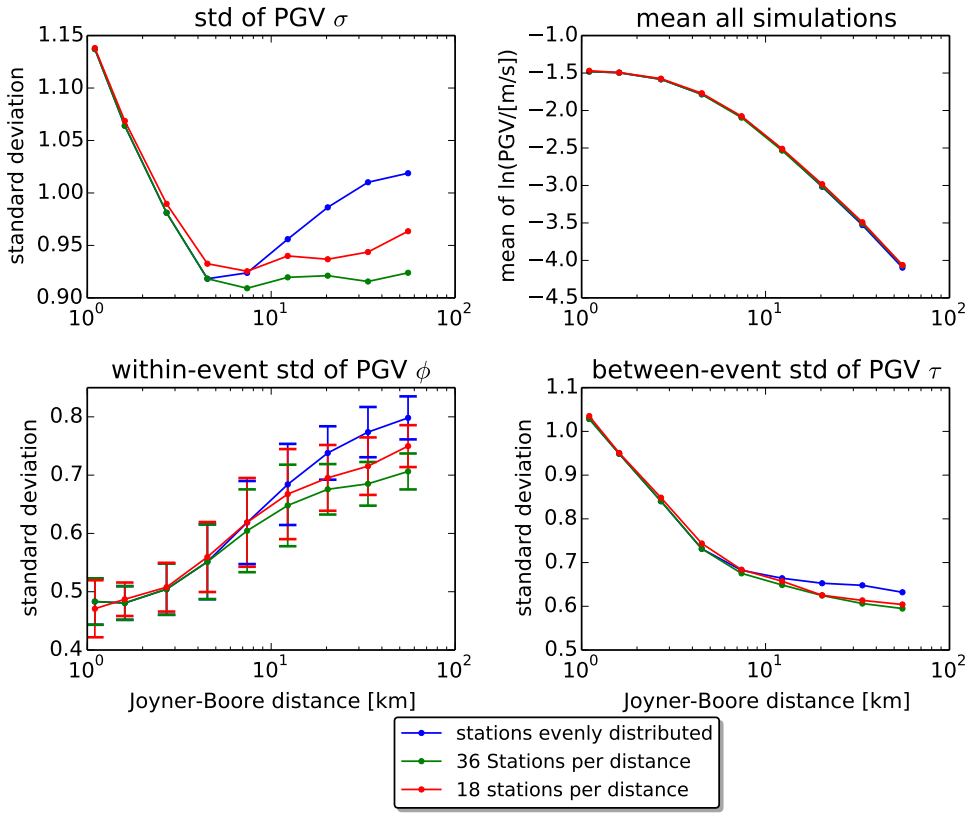

Figure 5.16: Top left: Standard deviation for different station configurations in dependence on their distance from the surface projection of the fault. **Top right:** Mean PGV. **Bottom left:** Within-event standard deviation. The error bar shows the standard deviation of within-event standard deviations. **Bottom right:** Between-event standard deviation.

A third station configuration is similar to the second one, but with only half of the stations (18 at each distance). This leads again to larger differences in ground-motion within the same event, as the inter-station distance is larger, resulting in a slightly increased within-event standard deviation. However, now the between-event standard deviation is not further affected as the quota of stations in regions parallel to the fault and stations in regions in forward and backward directivity remains the same, resulting in approximately the same mean ground motion level as for the station configuration with twice the number of stations.

The between-event standard deviation for all three station configurations is decreasing with increasing distance. In contrast, the within-event standard deviation exhibited a higher within-event variability for larger distances. An increase in standard deviation with distance for distances up to 50 km was also observed in observed data from Japanese earthquakes by Midorikawa and Ohtake (2004). Although, in their case they argued that the observed distance-dependence results from local and regional path effects and the re-

lated attenuation. In contrast, in the simulation presented here, no such path effects can occur, since the model uses a homogeneous halfspace. Recently Imtiaz et al. (2015) also performed synthetic simulations of ground motions for some observed earthquakes in a magnitude range between 5.8 and 6.8 and observed an increase with distance of within-event variability for bilateral rupture propagation only, while for unilateral ruptures they report a decrease. They argued, that unilateral ruptures more significantly experience the radiation pattern, especially in larger distances. Anyway, the dependence of the within-event standard deviation found here, raises the question whether the homoscedastic assumption made during the regression of observed data is justified or whether it would be more appropriate to determine multiple values of standard deviation for several distance bands.

5.7.2 Stability of the results

Another question which may arise concerning the reliability of the presented results is whether 200 simulations are enough to determine stable values for the mean PGV and the standard deviation. Figure 5.17 shows the evolution of the standard deviation, its within- and between-event component and the mean PGV in dependence of the number of simulations for the same simulations as in Fig. 5.7. If only the roughness or the slip distribution are variable, the mean PGV and its standard deviation are almost constant regardless of the number of simulations. If the rupture velocity is variable, the mean PGV as well as the standard deviation and its components fluctuate for less than 50 simulations. For a larger number of simulations, the values converge to a stable level. Greatest fluctuations are observed for variable hypocentre or energy magnitude where stable values are reached only after approximately 100 simulations. In all cases the mean PGV, the total standard deviation and its components have reached a constant value if 200 simulations are performed, such that I consider the number of simulations sufficient to get representative results.

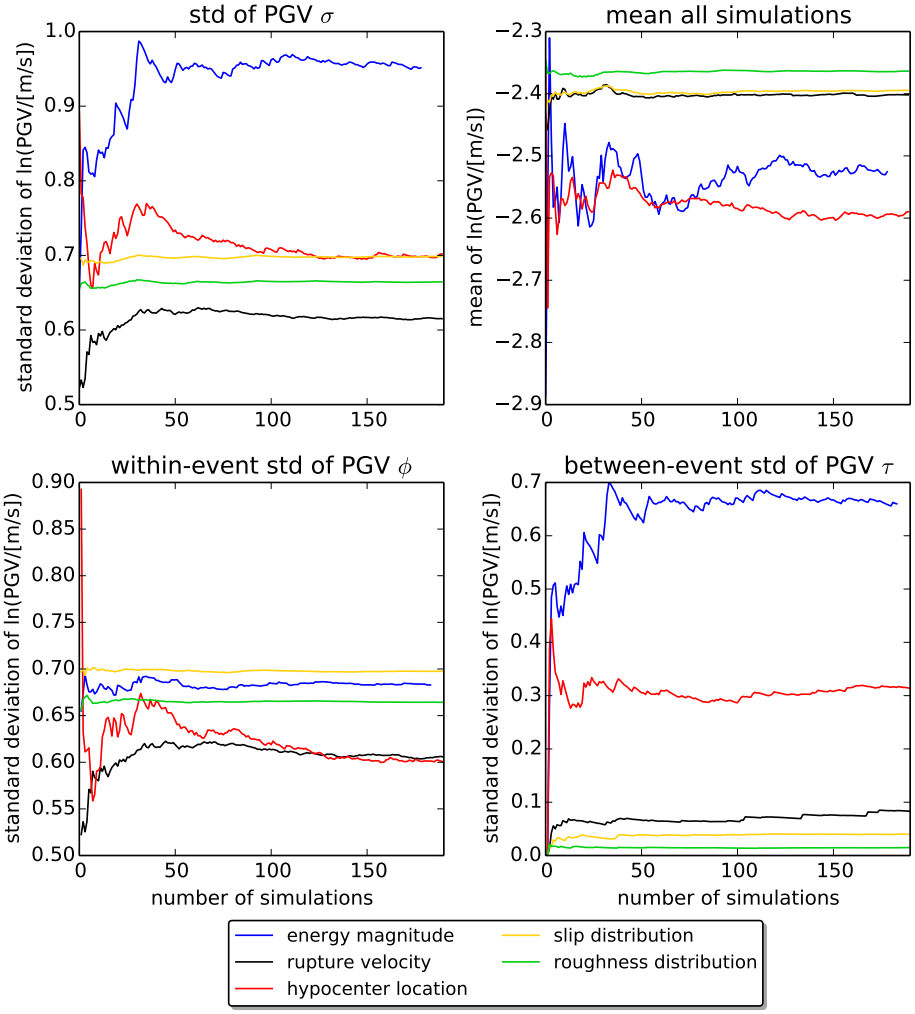

Figure 5.17: Dependence of the total standard deviation σ (**top left**), the mean of the logarithm of PGV (**top right**) , the within-event standard deviation ϕ (**bottom left**) and the between-event standard deviation τ (**bottom right**) on the number of simulations at a distance of 12 km. Coloured lines show results for different variable parameter.

Chapter 6

Conclusions and outlook

This work is dedicated to improving simulations of ground motions, especially in the near-field, and to a better understanding of the influence of the various modelling parameters on the resulting synthetic seismograms. The three main goals of this work were

- to verify that a kinematic source description combined with a purely deterministic wave propagation is suitable for the simulation of ground motion,
- to test the calibration of the high-frequency part of the ground motion by the energy magnitude, and
- to investigate the sensitivity of the ground motion and its variability to parametric uncertainties related to the source description.

To achieve the first goal, I introduced a simulation approach in which the source description is kinematic and includes a considerable amount of stochastic varibility in the distribution of slip on the fault and the distribution of focal mechanisms for the fault's subpatches. The wave propagation is conducted in a layered halfspace with no lateral heterogeneity. This simple velocity model enables to calculate Green's functions in advance and to keep them in a lookup table, which saves a considerable amount of computing time when performing multiple simulations. By comparing simulations with the observations of past events, I was able to show that key ground motion observables such as PGA or response spectra can be reproduced. For this purpose I considered three different earthquakes: the Wenchuan (2008) earthquake as a large crustal earthquake with surface rupture, the Tokachi-Oki (2003) earthquake as a large subduction earthquake and the Northridge (1994) earthquake as a medium-sized crustal earthquake on a blind fault.

With regard to the second goal, for these three examples I also used the energy magnitude as the mean to calibrate the rise time of the moment rate function. I was able to show that this calibration approximately led to the correct level of ground motion in terms of PGA and spectral content, even at high frequencies. This scaling of the frequency content increases the number of model parameters which can actually be estimated from

measured data after the earthquake, as the energy magnitude is determined from recorded seismograms and can be calculated within approximately 20 minutes after the earthquake. The usage of an empirical or guessed stress drop during the simulation is no longer necessary and the simulations are better adjusted to the earthquake. However, to proove that this calibration can deliver stable results, the verification with a wider range of actual earthquakes would be necessary. It would be desirable to show that simulations based on this technique give equally good or better results than simulations based on stress drop estimations. The presented method for the source description may also be combined with more sophisticated wavepropagation methods in order to test its performance and to check how much of the remaining bias is due to the velocity model and how much is caused by the source description.

Third, I considered the sensitivity of ground motion variability to several uncertainties in the source description. The most important result of this study is that the energy magnitude has the greatest influence on the variability of ground motion and causes the standard deviation of PGV to be two to three times higher than the standard deviation found from regression of observed ground motions. Consequently, future studies have to investigate reasons for this discrepancy between observations and simulations. Possible explanations could be an overestimated variability in observed energy magnitudes or an oversimplified relation between energy magnitude and rise time used by the presented approach for the calibration of the high-frequency ground motion. On the one hand, this points to the need for improved methods for the determination of energy magnitudes. I think that especially the possibility of path- and site-specific corrections to the estimated seismic energies have to be considered. On the other hand, this result calls for a more detailed study of the relation between observed energy magnitude and the kinematic source description.

A further finding was the dependence of the within-event variability on the distance to the fault. In all the presented simulation series, the within-event variability increased with distance from the fault, indicating that the homoscedastic assumption of ground motion variability being constant for all distances is an oversimplification. This suggest that future regression analysis, which can take advantage of more complete datasets at small distances, should consider a heteroscedastic approach which allows the variability of ground motion intensity measures to be variable with distance.

However, the information gained from studying the influence of parametric uncertainties on the ground motion variability is still limited. Future works need to consider more scenarios in terms of earthquake magnitude, size of the rupture area, or fault mechanisms. For a more profound study of the sensitivity of the ground motion variability to parametric source uncertainties, partial derivatives of the model outcome with respect to the input could be calculated. As the derivation is not an easy operation for a complex model, a possibility would be an algorithmic differentiation (Sambridge et al., 2007). This kind of study could hint to the most significant model parameters and allow to investigate those in greater detail.

Finally I would like to put the findings of this thesis in the context of suitability of synthetic ground motions for use in hazard studies. As pointed out by Abrahamson (2012), a ground motion simulation approach should be evalutated with respect to the following criteria:

- Verification: The computational correctness has to be shown.
- Calibration: The method has to be able to reproduce observed ground motions.
- Validation of variability: Methods must reproduce the observed variability.
- Robustness: Similar results should be obtained using different methods.
- Transparency: Other researchers must be able to use the code.

In this work the verification of the model was approached in Section 3.5 by comparing results of my simulation to results of another well established simulation method. The calibration was performed in Chapter 4 by reproducing general characteristics of three previously recorded earthquakes. Chapter 5 aimed at the validation of varibility and could show that the variability in PGV found by varying the hypocenter location, slip and roughness distribution and rupture velocity is comparable to the observed variability. Nonetheless this test also showed a strong exceedance of variability if the full variability of energy magnitudes is considered. The transparency is provided by making the code available and an appropriate documentation, although, to my knowledge, the code was not used externally, yet. The code for the source description and the rise-time scaling are freely available via https://github.com/ImadeGENSO/GENSO. The code for the calculation of Green's functions and for their convolution with the moment rate function as well as superposition at the receiver can be obtained by contacting Rongjiang Wang (Helmholtz-Centre Potsdam, German Research Centre for Geosciences). The point of robustness is subject to future work. It would be desirable to compare simulation results, similar to the effort made by researchers contributing to the SCEC Broadband Platform (Dreger et al., 2015).

As with every scientific study, there is still room for improvement and ideas are arising from this work. Regarding the implementation of the algorithm it would be advantageous to connect the discretisation of the source to the S-velocity model. The discretisation used in order to avoid any aliasing effects is dependent on the maximum frequency to be modelled, the S-velocity and the rupture velocity. Higher S-velocities require not as many grid points along the source. Hence, a discretisation adapted to the velocity model would be of benefit to reduce computation time. Moreover, different functional forms of the source-time function may be used to obtain more realistic values of rise time. The Brune's type of source-time function used in this work has a rather smooth form, so in order to make it appear more peaked, the rise-times resulting from the energy scaling are very small, which would translate into very high slip-velocities. Source-time functions of

a different functional form, such as suggested by Tinti et al. (2005) may result in more realistic slip velocities.

Appendix A

Anti-aliasing and zero-padding for Green's functions

In Section 3.3 I hinted to the fact that an anti-aliasing factor may be specified for the calculation of Green's function and a time should be given, after which the Green's functions are padded with zeros. Both of these parameters should avoid numerical artefacts which otherwise may lead to unrealistic results. Here, I shortly want to document the usage of these two parameters, as they may strongly influence the simulation results and as an inexperience modeller at the start of my work, this caused a lot of headache. None of the following is new to the scientific community, but in order to make the use of the method easier for young scientist new to the method, I wanted to add this chapter.

The Green's functions are initially calculated in the frequency domain. The resulting spectrum, regardless of the time window chosen for the Green's functions, includes the whole impulse response of the ground at the specified distance. When applying the inverse Fourier Transform to get from the frequency domain back to the time domain, the limited time window enters the processing. If the signal is longer than the time window, signal components from the end of the time window are mapped to the beginning of the time window. This aliasing effect will cause a wrong signal at the beginning of the time window. An example for this is shown in Figure A.1, which shows one component of the Green's function calculated for the velocity model given in Table 4.3 at a distance of 112 km. Due to the short window length, the signal length is not covered and aliasing introduces artefacts at the beginning of the time window. To suppress the artefacts at the beginning of the time function, the technique of complex frequencies is applied. Instead of the intended Green's function $f(t)$, a modified function is calculated, namely $g(t) = f(t) \cdot e^{-\alpha t}$. In the Fourier domain, this means the calculation of $G(\omega) = F(\omega - \imath\alpha)$ instead of $F(\omega)$. Due to the exponential function, signal amplitudes at later times are reduced, while signal amplitudes at the start are increased. Therefore, signal components after the end of the time window are very small and their mapping to the beginning of the time window has no significant influence on the signal at the start. To recover the amplitudes of the

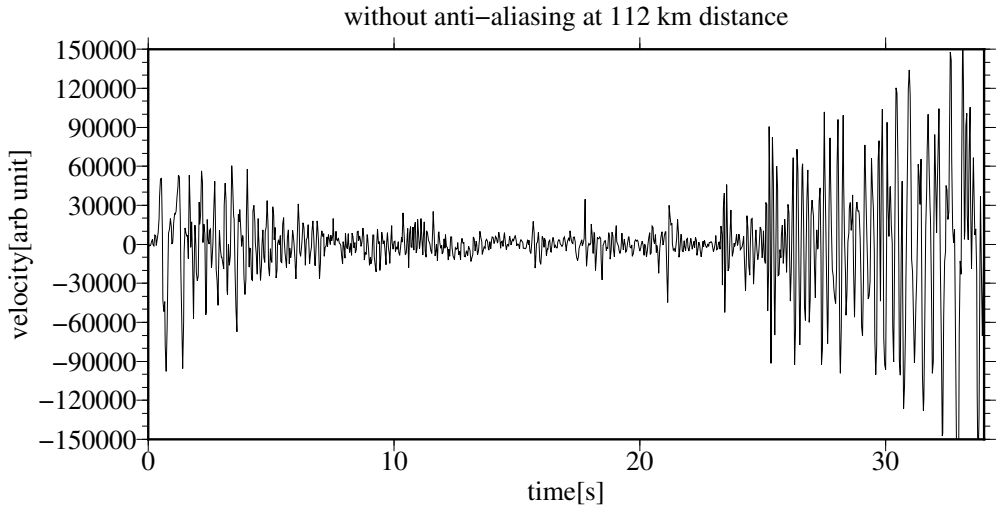

Figure A.1: Green's function for the velocity model given in Table 4.3 at a distance of 112 km. Due to the short time window, aliasing leads to artefacts at the beginning of the time window.

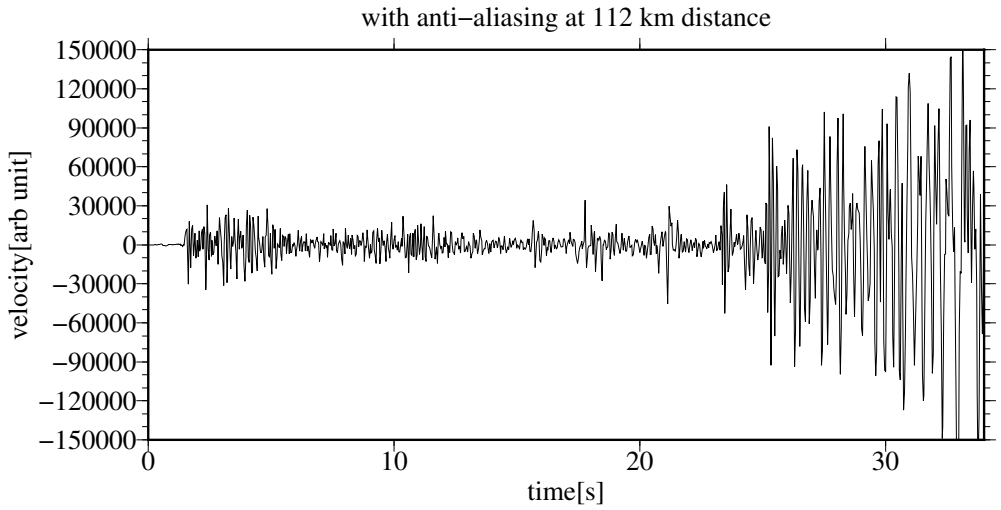

Figure A.2: Same as Fig. A.1 but with an implemented aliasing suppression factor of 0.01, i. e. a strong anti-aliasing function. The signal at the beginning of the time window is no longer influenced by signals from times larger than the time window.

original Green's function, after the Fourier Transform the time signal $g(t)$ is multiplied with $e^{\alpha t}$, resulting in the desired Green's function $f(t) = g(t) \cdot e^{\alpha t} = f(t) \cdot e^{-\alpha t} \cdot e^{\alpha t}$. The corresponding Green's function with the implemented technique of complex frequencies is shown in Fig. A.2. Artefacts due to aliasing are no longer visible at the beginning of the time window.

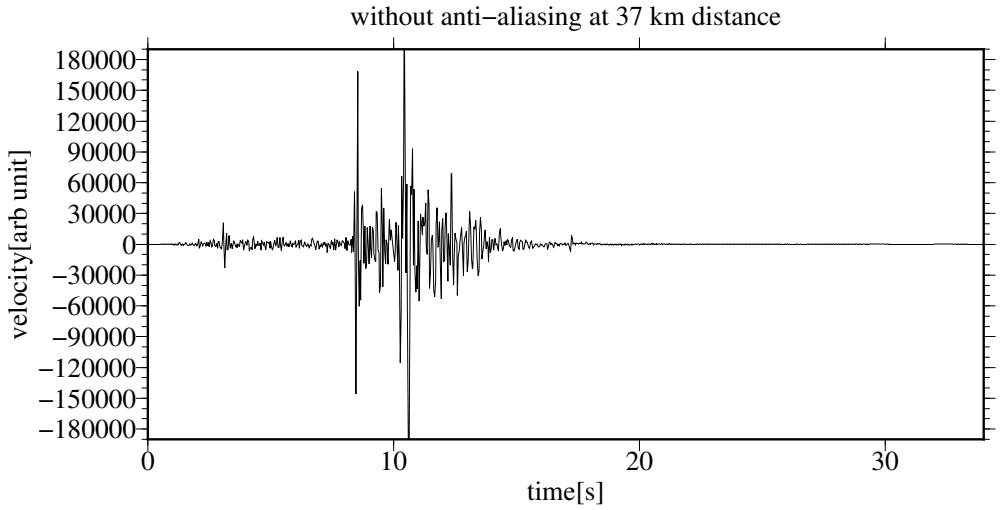

Figure A.3: Same as Fig. A.1 but at a distance of 37 km. Due to the shorter signal length, the full signal is well contained in the specified time window and no aliasing occurs.

This procedure works as expected, if indeed the signal is longer than the time window. If however at small distances the signal is shorter than the time window, at the end of the Green's function the signal should essentially be zero. Unfortunately, due to numerical incorrectness, the calculation does not deliver zero values but very very small amplitudes. This is still suitable if no anti-aliasing is applied, as shown in Figure A.3, which shows a Green's function for the same conditions as in Fig. A.1, but at a smaller distance of 37 km. As the signal is shorter than the window length, so no aliasing occurs. If now we would apply the anti-aliasing function, because we want to apply the same procedure to all Green's function in our database, the numerical noise at the end of the time window would be multiplied by $e^{\alpha t}$ in the last step of the calculation. Hence, the noise would be extremely amplified, which shows in the example of Figure A.4, where artefacts occur at the end of the time window.

In this case the zero-padding option should be applied. The user should estimate the length of the Green's function at the closest and most distant station and specify those times in the input file. A linear relation between signal length and distance from the source is assumed to estimate the signal length for all Green's functions. After the transition to the Fourier domain, the Green's functions are set to zero after the estimated signal length to avoid amplification of artificial noise. The corresponding example is shown in Figure A.5. It shows the same Green's function as Fig. A.4, but with zeros after the time of 20 s.

Concluding, one can say, that a sufficient window length and no anti-aliasing is the recommended way to go. If a window length shorter than the signal length has to be chosen to save computation time, anti-aliasing has to be applied, but should be combined with zero padding for short distances.

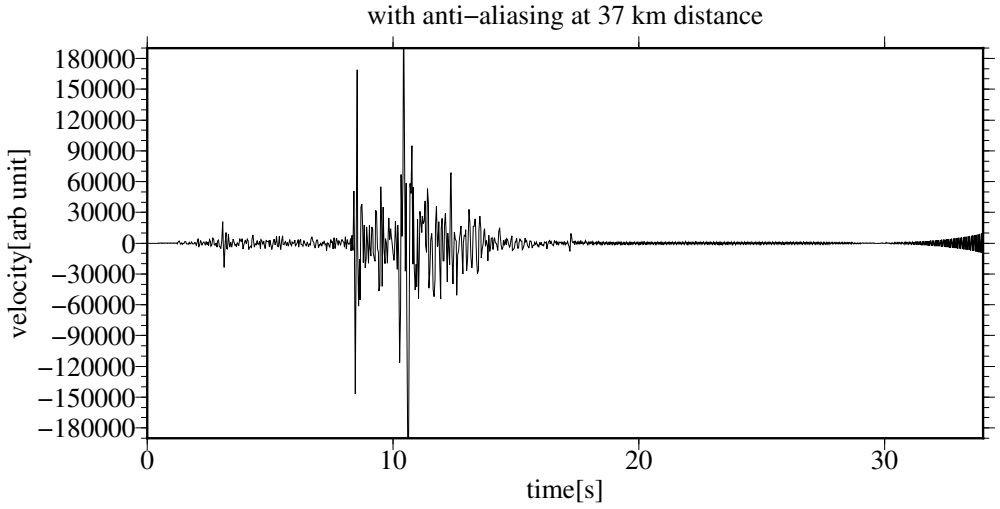

Figure A.4: Same as Fig. A.3 but with an implemented aliasing suppression factor of 0.01, i. e. a strong anti-aliasing function. Due to the multiplication with $e^{\alpha t}$ in the last step of the calculation, numerical noise is amplified at the end of the time window.

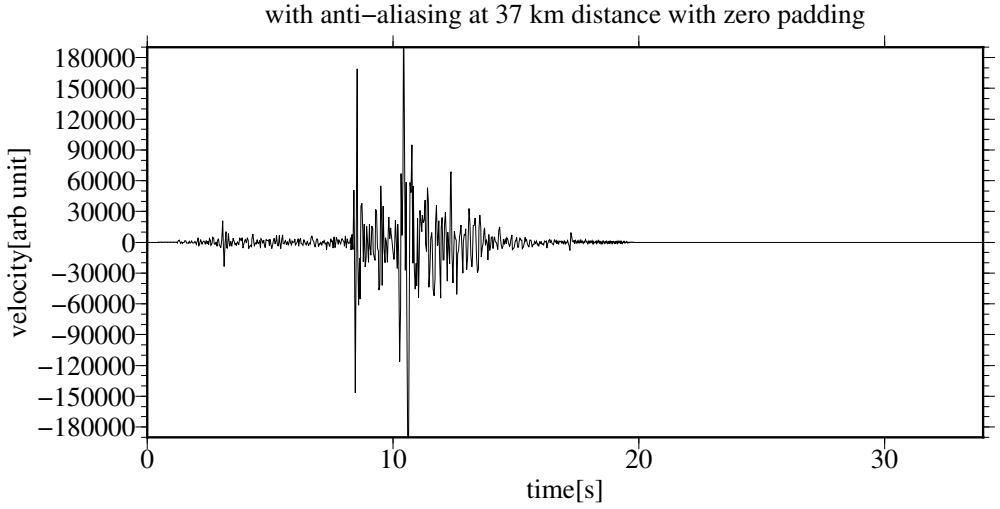

Figure A.5: Same as Fig. A.4 but with zero-padding after 20 s.

Appendix B

Publications

I have published the following articles during the course of this PhD:

- M. Picozzi, D. Bindi, M. Pittore, K. Kieling, and S. Parolai. Real-time risk assessment in seismic early warning and rapid response: a feasibility study in Bishkek (Kyrgyzstan). *Journal of Seismology*, **17**(2) 485–505, 2013. DOI 10.1007/s10950-012-9332-5.

  For this publication I calculated the synthetic seismograms used Section 4.3 "Deterministic synthetic dataset" and wrote a small part of the manuscript (approximately 5%). I also provided feedback on the manuscript.

- K. Kieling, R. Wang, and S. Hainzl. Broadband ground motion simulation using energy constrained rise time scaling. *Bulletin of the Seismological Society of America*, **104**(6) 2683–2697, 2014. DOI 10.1785/0120140063.

  For this publication I implemented the kinematic source description, ran the simulations, prepared all figures and wrote the text. Rongjiang Wang implemented the calculation of the Green's functions and the convolution and superposition. He and Sebastian Hainzl both supervised the work, gave advice to improve the method and provided feedback on the manuscript.

Bibliography

B. T. Aagaard, J. F. Hall, and T. H. Heaton. Characterization of near source ground motions with earthquake simulations. *Earthquake Spectra*, **17**(2) 177–207, May 2001.

N. Abrahamson. Incorporating earthquake source physics into ground motion models for seismic hazard studies. In *ECGS*, 2012.

N. Abrahamson and W. Silva. Summary of the Abrahamson & Silva NGA ground-motion relations. *Earthquake Spectra*, **24**(1) 67–97, 2008. DOI 10.1193/1.2924360.

N. A. Abrahamson and R. R. Youngs. A stable algorithm for regression analyses using the random effects model. *Bulletin of the Seismological Society of America*, **82**(1) 505–510, 1992.

K. Aki. Generation and propagation of G waves from the Niigata earthquake of June 16, 1964: Part 2. Estimation of earthquake moment, released energy and stress drop from the G wave spectra. *Bull. Earthq. Res. Inst.*, **44** 73–88, 1966.

K. Aki. A perspective on the history of strong motion seismology. *Physics of the Earth and Planetary Interiors*, **137**(1-4) 5–11, 2003. DOI http://dx.doi.org/10.1016/S0031-9201(03)00004-9.

K. Aki and P. G. Richards. *Quantitative seismology: theory and methods*. University Science Books, San Francisco, 2 edition, 2002.

S. Akkar and Ö. Özen. Effect of peak ground velocity on deformation demands for SDOF systems. *Earthquake Engineering & Structural Dynamics*, **34**(13) 1551–1571, 2005. DOI 10.1002/eqe.492.

G. Ameri, A. Emolo, F. Pacor, and F. Gallovic. Ground-motion simulations for the 1980 m 6.9 irpinia earthquake (southern italy) and scenario events. *BULLETIN OF THE SEISMOLOGICAL SOCIETY OF AMERICA*, **101**(3) 1136–1151, 2011. DOI 10.1785/0120100231.

S. Aoi, T. Kunugi, and H. Fujiwara. Strong motion seismograph network operated by NIED: K-NET and KiK-net. *Journal of Japan Association for Earthquake Engineering*, **4**(3) 65–74, 2004.

L. A. Atik, N. Abrahamson, J. J. Bommer, F. Scherbaum, F. Cotton, and N. Kuehn. The variability of ground-motion prediction models and its components. *Seism. Res. Lett.*, **81**(5) 794–801, 2010. DOI 10.1785/gssrl.81.5.794.

C. Bach. *Improving statistical seismicity models.* PhD thesis, University of Potsdam, 2013.

A. Baltay, S. Ide, G. Prieto, and G. Beroza. Variability in earthquake stress drop and apparent stress. *Geophysical Research Letters*, **38**(6) L06303, 2011. DOI 10.1029/2011GL046698.

D. Bates, M. MÃ¤chler, B. M. Bolker, and S. C. Walker. Fitting linear mixed-effects models using lme4. *Journal of Statistical Software*, 2014.

C. Baumann and L. A. Dalguer. Evaluating the compatibility of dynamic rupture based synthetic ground motion with empirical ground motion prediction equation. *Bulletin of the Seismological Society of America*, 2014. DOI 10.1785/0120130077.

I. A. Beresnev and G. M. Atkinson. FINSIM–a FORTRAN program for simulating stochastic acceleration time histories from finite faults. *Seis. Res. Lett.*, **69**(1) 27–32, 1998. DOI 10.1785/gssrl.69.1.27.

K. Beyer and J. J. Bommer. Relationships between median values and between aleatory variabilities for different definitions of the horizontal component of motion. *Bulletin of the Seismological Society of America*, **96**(4A) 1512–1522, 2006. DOI 10.1785/0120050210.

D. Bindi, M. Massa, L. Luzi, G. Ameri, F. Pacor, R. Puglia, and P. Augliera. Pan-European ground-motion prediction equations for the average horizontal component of PGA, PGV, and 5%-damped PSA at spectral periods up to 3.0 s using the RESORCE dataset. *Bulletin of Earthquake Engineering*, **12**(1) 391–430, 2014. DOI 10.1007/s10518-013-9525-5.

J. Boatwright and G. L. Choy. Teleseismic estimates of the energy radiated by shallow earthquakes. *Journal of Geophysical Research: Solid Earth*, **91**(B2) 2095–2112, 1986. DOI 10.1029/JB091iB02p02095.

J. Boatwright, K. Thywissen, and L. C. Seekins. Correlation of ground motion and intensity for the 17 january 1994 northridge, california, earthquake. *Bulletin of the Seismological Society of America*, **91**(4) 739–752, 2001. DOI 10.1785/0119990049.

J. J. Bommer and N. A. Abrahamson. Why do modern probabilistic seismic-hazard analyses often lead to increased hazard estimates? *Bulletin of the Seismological Society of America*, **96**(6) 1967–1977, 2006. DOI 10.1785/0120060043.

D. M. Boore. Stochastic simulation of high-frequency ground motions based on seismological models of the radiated spectra. *Bulletin of the Seismological society of America*, **73**(6) 1865–1894, 1983.

D. M. Boore. Simulation of ground motion using the stochastic method. In Y. Ben-Zion, editor, *Seismic Motion, Lithospheric Structures, Earthquake and Volcanic Sources: The Keiiti Aki Volume*, Pageoph Topical Volumes, pages 635–676. Birkhäuser Basel, 2003. ISBN 978-3-7643-7011-4.

D. M. Boore and G. M. Atkinson. Stochastic prediction of ground motion and spectral response parameters at hard-rock sites in eastern North America. *Bulletin of the Seismological Society of America*, **77**(2) 440–467, Apr. 1987.

D. M. Boore and G. M. Atkinson. Ground-motion prediction equations for the average horizontal component of PGA, PGV, and 5%-damped PSA at spectral periods between 0.01 s and 10.0 s. *Earthquake Spectra*, **24**(1) 99–138, 2008. DOI 10.1193/1.2830434.

D. M. Boore and W. B. Joyner. Site amplifications for generic rock sites. *Bulletin of the Seismological Society of America*, **87**(2) 327–341, 1997.

D. M. Boore, J. Watson-Lamprey, and N. A. Abrahamson. Orientation-independent measures of ground motion. *Bulletin of the Seismological Society of America*, **96**(4A) 1502–1511, 2006. DOI 10.1785/0120050209.

P. Bormann, M. Baumbach, G. Bock, H. Grosser, G. L. Choy, and J. Boatwright. *IASPEI New Manual of Seismological Observatory Practice (NMSOP)*, volume 1. GeoForschungZentrum Potsdam, 2002.

P. Bormann and D. Di Giacomo. The moment magnitude M_w and the energy magnitude M_e: common roots and differences. *Journal of Seismology*, **15** 411–427, 2011. DOI 10.1007/s10950-010-9219-2.

D. R. Brillinger and H. K. Preisler. An exploratory analysis of the joyner-boore attenuation data. *Bulletin of the Seismological Society of America*, **74**(4) 1441–1450, 1984.

J. N. Brune. Tectonic stress and the spectra of seismic shear waves from earthquakes. *Journal of Geophysical Research*, **75**(26) 4997–5009, 1970. DOI 10.1029/JB075i026p04997.

J. N. Brune and A. Anooshehpoor. A physical model of the effect of a shallow weak layer on strong ground motion for strike-slip ruptures. *Bulletin of the Seismological Society of America*, **88**(4) 1070–1078, 1998.

K. W. Campbell and Y. Bozorgnia. NGA ground motion model for the geometric mean horizontal component of PGA, PGV, PGD and 5% damped linear elastic response spectra for periods ranging from 0.01 to 10 s. *Earthquake Spectra*, **24**(1) 139–171, 2008. DOI 10.1193/1.2857546.

T. Candela, F. Renard, Y. Klinger, K. Mair, J. Schmittbuhl, and E. E. Brodsky. Roughness of fault surfaces over nine decades of length scales. *J. Geophys. Res.: Solid Earth*, **117** (B8) B08409, 2012. DOI 10.1029/2011JB009041.

C. Cattania, S. Hainzl, L. Wang, F. Roth, and B. Enescu. Propagation of coulomb stress uncertainties in physics-based aftershock models. *Journal of Geophysical Research: Solid Earth*, **119**(10) 7846–7864, 2014. DOI 10.1002/2014JB011183.

M. Causse, F. Cotton, and P. M. Mai. Constraining the roughness degree of slip heterogeneity. *Journal of Geophysical Research*, **115** B05304, 2010. DOI 10.1029/2009JB006747.

B. S.-J. Chiou and R. R. Youngs. An NGA model for the average horizontal component of peak ground motion and response spectra. *Earthquake Spectra*, **24**(1) 173–215, 2008. DOI 10.1193/1.2894832.

F. Cotton, R. Archuleta, and M. Causse. What is sigma of the stress drop? *Seismological Research Letters*, **84**(1) 42–48, 2013. DOI 10.1785/0220120087.

L. A. Dalguer and S. M. Day. Staggered-grid split-node method for spontaneous rupture simulation. *Journal of Geophysical Research: Solid Earth*, **112**(B2) B02302, 2007. DOI 10.1029/2006JB004467.

S. Day. Tests of 3D elastodynamics codes, LIFELINES PROGRAM TASK 1A01 final report to pacific earthquake engineering research center. Technical report, San Diego State University, September 2001.

J. de la Puente, M. Käser, M. Dumbser, and H. Igel. An arbitrary high-order discontinuous Galerkin method for elastic waves on unstructured meshes - IV. Anisotropy. *Geophysical Journal International*, **169**(3) 1210–1228, 2007. DOI 10.1111/j.1365-246X.2007.03381.x.

B. Derras, P. Bard, and F. Cotton. Towards fully data driven ground-motion prediction models for Europe. *Bulletin of Earthquake Engineering*, **12**(1) 495–516, 2014. DOI 10.1007/s10518-013-9481-0.

D. Di Giacomo. *Determination of the energy magnitude M_e : application to rapid response purposes and insights to regional/local variabilities*. PhD thesis, University of Potsdam, 2010. URL `http://opus.kobv.de/ubp/volltexte/2011/5076/`.

D. Di Giacomo, D. Bindi, S. Parolai, and A. Oth. Residual analysis of teleseismic p-wave energy magnitude estimates: inter- and intrastation variability. *Geophysical Journal International*, **185**(3) 1444–1454, 2011. DOI 10.1111/j.1365-246X.2011.05019.x.

D. Di Giacomo, S. Parolai, P. Bormann, H. Grosser, J. Saul, R. Wang, and J. Zschau. Suitability of rapid energy magnitude determinations for emergency response purposes. *Geophys. J. Int.*, **180**(1) 361–374, 2010. DOI 10.1111/j.1365-246X.2009.04416.x.

J. Douglas and H. Aochi. A survey of techniques for predicting earthquake ground motions for engineering purposes. *Surveys in Geophysics*, **29**(3) 187–220, 2008. DOI 10.1007/s10712-008-9046-y.

D. S. Dreger. Empirical Green's function study of the January 17, 1994 Northridge, California earthquake. *Geophysical Research Letters*, **21**(24) 2633–2636, 1994. DOI 10.1029/94GL02661.

D. S. Dreger, G. C. Beroza, S. M. Day, C. A. Goulet, T. H. Jordan, P. A. Spudich, and J. P. Stewart. Validation of the scec broadband platform v14.3 simulation methods using pseudospectral acceleration data. *Seismological Research Letters*, **86**(1) 39–47, 2015. DOI 10.1785/0220140118.

A. Frankel. Simulating strong motions of large earthquakes using recordings of small earthquakes: the Loma Prieta mainshock as a test case. *Bulletin of the Seismological Society of America*, **85**(4) 1144–1160, 1995.

F. Gallovič and J. Brokesova. Hybrid k-squared source model for strong ground motion simulations: Introduction. *Physics of the earth and planetary interiors*, **160** 34–50, 2007.

R. W. Graves, B. T. Aagaard, K. W. Hudnut, L. M. Star, J. P. Stewart, and T. H. Jordan. Broadband simulations for Mw 7.8 southern San Andreas earthquakes: Ground motion sensitivity to rupture speed. *Geophysical Research Letters*, **35**(22) L22302, 2008. DOI 10.1029/2008GL035750.

R. W. Graves and A. Pitarka. Broadband time history simulation using a hybrid approach. In *Proc. 13th World Conf. Earthq. Eng., Vancouver, Canada*, number 1098, 2004.

R. W. Graves and A. Pitarka. Broadband ground-motion simulation using a hybrid approach. *Bull. Seism. Soc. Am.*, **100**(5A) 2095–2123, Oct. 2010. DOI 10.1785/0120100057.

M. Guatteri, P. M. Mai, G. C. Beroza, and J. Boatwright. Strong ground-motion prediction from stochastic-dynamic source models. *Bulletin of the Seismological Society of America*, **93**(1) 301–313, 2003. DOI 10.1785/0120020006.

T. C. Hanks and R. K. McGuire. The character of high-frequency strong ground motion. *Bull Seism Soc Am*, **71**(6) 2071–2095, 1981.

S. Hartzell and D. V. Helmberger. Strong-motion modeling of the Imperial Valley earthquake of 1979. *Bull. Seism. Soc. Am.*, **72**(2) 571–596, 1982.

S. Hartzell, P. Liu, and C. Mendoza. The 1994 Northridge, California, earthquake: Investigation of rupture velocity, risetime, and high-frequency radiation. *J. Geophys. Res.*, **101**(B9) 20091–20108, 1996. DOI 10.1029/96JB01883.

S. H. Hartzell. Earthquake aftershocks as Green's functions. *Geophysical Research Letters*, **5**(1) 1–4, 1978. DOI 10.1029/GL005i001p00001.

N. Haskell. Total energy and energy spectral density of elastic wave radiation from propagating faults. *Bull. Seismol. Soc. Am.*, **56** 1811–1842, 1964.

G. P. Hayes, L. Rivera, and H. Kanamori. Source inversion of the W-phase: Real-time implementation and extension to low magnitudes. *Seismological Research Letters*, **80** (5) 817–822, 2009. DOI 10.1785/gssrl.80.5.817.

T. H. Heaton and D. V. Helmberger. Generalized ray models of the San Fernando earthquake. *Bull. Seism. Soc. Am.*, **69**(5) 1311–1341, 1979.

S. Heimann. *A Robust Method To Estimate Kinematic Earthquake Source Parameters*. PhD thesis, Universität Hamburg, 2010. URL `http://kinherd.org/thesis.pdf`.

A. Herrero and P. Bernard. A kinematic self-similar rupture process for earthquakes. *Bull. Seism. Soc. Am.*, **84**(4) 1216–1228, August 1994.

Y. Hisada. A theoretical omega-square model considering spatial variation in slip and rupture velocity. part 2: Case for a two-dimensional source model. *Bulletin of the Seismological Society of America*, **91**(4) 651–666, 2001. DOI 10.1785/0120000097.

R. Honda, S. Aoi, N. Morikawa, H. Sekiguchi, T. Kunugi, and H. Fujiwara. Ground motion and rupture process of the 2003 Tokachi-oki earthquake obtained from strong motion data of K-NET and KiK-net. *Earth, Planets, and Space*, **56** 317–322, 2004.

K. W. Hudnut, Z. Shen, M. Murray, S. McClusky, R. King, T. Herring, B. Hager, Y. Feng, P. Fang, A. Donnellan, and Y. Bock. Co-seismic displacements of the 1994 Northridge, California, earthquake. *Bulletin of the Seismological Society of America*, **86**(1B) S19–S36, Feb. 1996.

L. Hutchings, E. Ioannidou, W. Foxall, N. Voulgaris, J. Savy, I. Kalogeras, L. Scognamiglio, and G. Stavrakakis. A physically based strong ground-motion prediction methodology; application to PSHA and the 1999 Mw= 6.0 Athens earthquake. *Geophysical Journal International*, **168**(2) 659–680, 2007. DOI 10.1111/j.1365-246X.2006.03178.x.

S. Ide and G. C. Beroza. Does apparent stress vary with earthquake size? *Geophysical Research Letters*, **28**(17) 3349–3352, 2001. DOI 10.1029/2001GL013106.

A. Imtiaz, M. Causse, E. Chaljub, and F. Cotton. Is ground-motion variability distance dependent? Insight from finite-source rupture simulations. *Bulletin of the Seismological Society of America*, **105**(2A) 950–962, 2015. DOI 10.1785/0120140107.

T. Inoue and T. Miyatake. 3D simulation of near-field strong ground motion based on dynamic modeling. *Bulletin of the Seismological Society of America*, **88**(6) 1445–1456, 1998.

K. Irikura and K. Kamae. Estimation of strong ground motion in broad-frequency band based on a seismic source scaling model and an empirical Green's function technique. *Annali Di Geofisica*, **XXXVII**(6) 1721–1743, 1994.

C. Ji, D. J. Wald, and D. V. Helmberger. Source description of the 1999 Hector Mine, California, Earthquake, Part I: Wavelet domain inversion theory and resolution analysis. *Bulletin of the Seismological Society of America*, **92**(4) 1192–1207, 2002. DOI 10.1785/0120000916.

W. B. Joyner and D. M. Boore. Peak horizontal acceleration and velocity from strong-motion records including records from the 1979 imperial valley, california, earthquake. *Bulletin of the Seismological Society of America*, **71**(6) 2011–2038, 1981.

T. Kagawa, K. Irikura, and P. G. Somerville. Differences in ground motion and fault rupture process between the surface and buried rupture earthquakes. *Earth Planets Space*, **56** 3–14, 2004.

S. I. Kaka and G. M. Atkinson. Relationships between instrumental ground-motion parameters and modified mercalli intensity in eastern north america. *Bulletin of the Seismological Society of America*, **94**(5) 1728–1736, 2004. DOI 10.1785/012003228.

M. Käser and M. Dumbser. An arbitrary high-order discontinuous Galerkin method for elastic waves on unstructured meshes I. The two-dimensional isotropic case with external source terms. *Geophys. J. Int.*, **166**(2) 855–877, 2006.

M. Käser and F. Gallovič. Effects of complicated 3-D rupture geometries on earthquake ground motion and their implications: a numerical study. *Geophys. J. Int.*, **172**(1) 276–292, 2008. DOI 10.1111/j.1365-246X.2007.03627.x.

B. Kennett. *IASPEI 1991 Seismological Tables*. Research School of Earth Sciences, Australian National University, Canberra, 1991.

K. Kieling, R. Wang, and S. Hainzl. Broadband ground motion simulation using energy constrained rise time scaling. *Bul. Seism. Soc. Am.*, **104**(6) 2683–2697, 2014. DOI 10.1785/0120140063.

D. Kilb, G. Biasi, J. Anderson, J. Brune, Z. Peng, and F. L. Vernon. A comparison of spectral parameter kappa from small and moderate earthquakes using southern california anza seismic network data. *Bulletin of the Seismological Society of America*, **102** (1) 284–300, 2012. DOI 10.1785/0120100309.

F. Krüger and M. Ohrnberger. Tracking the rupture of the Mw = 9.3 Sumatra earthquake over 1,150 km at teleseismic distance. *Nature*, **435**(7044) 937–939, June 2005. DOI 10.1038/nature03696.

S. Kurahashi and K. Irikura. Characterized source model for simulating strong ground motions during the 2008 Wenchuan Earthquake. *Bull. Seism. Soc. Am.*, **100**(5B) 2450–2475, 2010. DOI 10.1785/0120090308.

X. Li, Z. Zhou, M. Huang, R. Wen, H. Yu, D. Lu, Y. Zhou, and J. Cui. Preliminary analysis of strong-motion recordings from the magnitude 8.0 Wenchuan, China, earthquake of 12 May 2008. *Seis. Res. Lett.*, **79**(6) 844–854, 2008. DOI 10.1785/gssrl.79.6.844.

P. Liu, R. J. Archuleta, and S. H. Hartzell. Prediction of broadband ground-motion time histories: Hybrid low/high- frequency method with correlated random source parameters. *Bul. Seism. Soc. Am.*, **96**(6) 2118–2130, 2006. DOI 10.1785/0120060036.

J. Liu-Zeng, Z. Zhang, L. Wen, P. Tapponnier, J. Sun, X. Xing, G. Hu, Q. Xu, L. Zeng, L. Ding, C. Ji, K. Hudnut, and J. van der Woerd. Co-seismic ruptures of the 12 May 2008, Ms 8.0 Wenchuan earthquake, Sichuan: East-west crustal shortening on oblique, parallel thrusts along the eastern edge of Tibet. *Earth and Planetary Science Letters*, **286**(3-4) 355 – 370, 2009. DOI 10.1016/j.epsl.2009.07.017.

M. Lu, X. J. Li, X. W. An, and J. X. Zhao. A comparison of recorded response spectra from the 2008 Wenchuan, China, Earthquake with modern ground-motion prediction models. *Bull. Seism. Soc. Am.*, **100**(5B) 2357–2380, 2010. DOI 10.1785/0120090303.

P. M. Mai and G. C. Beroza. A spatial random field model to characterize complexity in earthquake slip. *J. Geophys. Res.*, **107**(B11) 2308, Nov. 2002. DOI 10.1029/2001JB000588.

I. Manighetti, M. Campillo, C. Sammis, P. M. Mai, and G. King. Evidence for self-similar, triangular slip distributions on earthquakes: Implications for earthquake and fault mechanics. *Journal of Geophysical Research*, **110** B05302, 2005. DOI 10.1029/2004JB003174.

B. Mena, P. M. Mai, K. B. Olsen, M. D. Purvance, and J. N. Brune. Hybrid broadband ground-motion simulation using scattering Green's functions: Application to large-magnitude events. *Bull Seism Soc Am*, **100**(5A) 2143–2162, Oct. 2010. DOI 10.1785/0120080318.

S. Midorikawa and Y. Ohtake. Variance of peak ground acceleration and velocity in attenuation relationships. In *13 th World Conference on Earthquake Engineering, Vancouver, B.C., Canada*, number 325, August 1-6 2004.

D. Motazedian and G. M. Atkinson. Stochastic finite-fault modeling based on a dynamic corner frequency. *Bulletin of the Seismological Society of America*, **95**(3) 995–1010, 2005. DOI 10.1785/0120030207.

A. Nozu and K. Irikura. Strong-motion generation areas of a great subduction-zone earthquake: Waveform inversion with empirical Green's functions for the 2003 Tokachi-oki Earthquake. *Bull. Seism. Soc. Am.*, **98**(1) 180–197, 2008. DOI 10.1785/0120060183.

K. B. Olsen, S. M. Day, J. B. Minster, Y. Cui, A. Chourasia, D. Okaya, P. Maechling, and T. Jordan. TeraShake2: Spontaneous rupture simulations of Mw 7.7 earthquakes on the southern San Andreas fault. *Bulletin of the Seismological Society of America*, **98**(3) 1162–1185, 2008. DOI 10.1785/0120070148.

K. B. Olsen, R. Madariaga, and R. J. Archuleta. Three-dimensional dynamic simulation of the 1992 Landers Earthquake. *Science*, **278**(5339) 834–838, 1997. DOI 10.1126/science.278.5339.834.

F. Pacor, G. Cultrera, A. Mendez, and M. Cocco. Finite fault modeling of strong motions using a hybrid deterministic-stochastic approach. *Bull. Seis. Soc. Am.*, **95**(1) 225–240, 2005. DOI 10.1785/0120030163.

S. Peyrat and K. B. Olsen. Nonlinear dynamic rupture inversion of the 2000 Western Tottori, Japan, earthquake. *Geophysical Research Letters*, **31**(5) n/a–n/a, 2004. DOI 10.1029/2003GL019058.

M. Picozzi, D. Bindi, M. Pittore, K. Kieling, and S. Parolai. Real-time risk assessment in seismic early warning and rapid response: a feasibility study in Bishkek (Kyrgyzstan). *Journal of Seismology*, **17**(2) 485–505, 2013. DOI 10.1007/s10950-012-9332-5.

A. Pitarka, L. A. Dalguer, S. M. Day, P. G. Somerville, and K. Dan. Numerical study of ground-motion differences between buried-rupturing and surface-rupturing earthquakes. *Bull. Seism. Soc. Am.*, **99**(3) 1521–1537, 2009. DOI 10.1785/0120080193.

A. Pitarka, P. Somerville, Y. Fukushima, T. Uetake, and K. Irikura. Simulation of near-fault strong-ground motion using hybrid Green's functions. *Bulletin of the Seismological Society of America*, **90**(3) 566–586, 2000. DOI 10.1785/0119990108.

F. Renard, T. Candela, and E. Bouchaud. Constant dimensionality of fault roughness from the scale of micro-fractures to the scale of continents. *Geophys. Res. Lett.*, **40**(1) 83–87, 2013. DOI 10.1029/2012GL054143.

J. Ripperger, P. M. Mai, and J.-P. Ampuero. Variability of near-field ground motion from dynamic earthquake rupture simulations. *Bulletin of the Seismological Society of America*, **98**(3) 1207–1228, 2008. DOI 10.1785/0120070076.

M. Sambridge, P. Rickwood, N. Rawlinson, and S. Sommacal. Automatic differentiation in geophysical inverse problems. *Geophysical Journal International*, **170**(1) 1–8, 2007. DOI 10.1111/j.1365-246X.2007.03400.x.

SCEC CVM4. SCEC Southern California Earthquake Center. Caltech. Community Velocity Model, Version 4, 2014. DOI 10.7909/C3WD3xH1.

J. Schmedes, R. J. Archuleta, and D. Lavallé. Correlation of earthquake source parameters inferred from dynamic rupture simulations. *Journal of Geophysical Research: Solid Earth*, **115**(B3) B03304, 2010. DOI 10.1029/2009JB006689.

Z.-K. Shen, B. X. Ge, D. D. Jackson, D. Potter, M. Cline, and L.-Y. Sung. Northridge earthquake rupture models based on the global positioning system measurements. *Bull. Seismol. Soc. Am.*, **86**(1B) S37–48, Feb. 1996.

S. K. Singh and M. Ordaz. Seismic energy release in Mexican subduction zone earthquakes. *Bulletin of the Seismological Society of America*, **84**(5) 1533–1550, 1994.

P. Somerville, K. Irikura, R. Graves, S. Sawada, D. Wald, N. Abrahamson, Y. Iwasaki, T. Kagawa, N. Smith, and A. Kowada. Characterizing crustal earthquake slip models for the prediction of strong ground motion. *Seism. Res. Lett.*, **70** 59–80, 1999.

S. G. Song and P. Somerville. Physics-based earthquake source characterization and modeling with geostatistics. *Bulletin of the Seismological Society of America*, **100**(2) 482–496, 2010. DOI 10.1785/0120090134.

P. J. Stafford. Crossed and nested mixed-effects approaches for enhanced model development and removal of the ergodic assumption in empirical ground-motion models. *Bulletin of the Seismological Society of America*, **104**(2) 702–719, 2014. DOI 10.1785/0120130145.

F. O. Strasser, N. A. Abrahamson, and J. J. Bommer. Sigma: Issues, insights, and challenges. *Seismological Research Letters*, **80**(1) 40–56, 2009. DOI 10.1785/gssrl.80.1.40.

X. Sun, X. Tao, S. Duan, and C. Liu. Kappa (k) derived from accelerograms recorded in the 2008 wenchuan mainshock, sichuan, china. *Journal of Asian Earth Sciences*, **73**(0) 306 – 316, 2013. DOI http://dx.doi.org/10.1016/j.jseaes.2013.05.008.

E. Tinti, E. Fukuyama, A. Piatanesi, and M. Cocco. A kinematic source-time function compatible with earthquake dynamics. *Bulletin of the Seismological Society of America*, **95**(4) 1211–1223, 2005. DOI 10.1785/0120040177.

C. Van Houtte, S. Drouet, and F. Cotton. Analysis of the origins of κ (kappa) to compute hard rock to rock adjustment factors for GMPEs. *Bulletin of the Seismological Society of America*, **101**(6) 2926–2941, 2011. DOI 10.1785/0120100345.

A. Venkataraman and H. Kanamori. Effect of directivity on estimates of radiated seismic energy. *J Geophys Res*, **109** B04301, 2004. DOI 10.1029/2003JB002548.

D. J. Wald and T. H. Heaton. Spatial and temporal distribution of slip for the 1992 Landers, California, earthquake. *Bulletin of the Seismological Society of America*, **84** (3) 668–691, 1994.

D. J. Wald, T. H. Heaton, and K. W. Hudnut. The slip history of the 1994 Northridge, California, earthquake determined from strong-motion, teleseismic, GPS, and leveling data. *Bulletin of the Seismological Society of America*, **86**(1B) S49–70, Feb. 1996.

D. J. Wald, V. Quitoriano, T. H. Heaton, and H. Kanamori. Relationships between peak ground acceleration, peak ground velocity, and modified mercalli intensity in california. *Earthquake Spectra*, **15**(3) 557–564, 1999. DOI 10.1193/1.1586058.

R. Wang. A simple orthonormalization method for stable and efficient computation of Green's functions. *Bull. Seism. Soc. Am.*, **89(3)** 733–741, 1999.

Y.-Y. Wen, K.-F. Ma, and D. D. Oglesby. Variations in rupture speed, slip amplitude and slip direction during the 2008 Mw 7.9 Wenchuan Earthquake. *Geophysical Journal International*, **190**(1) 379–390, 2012. DOI 10.1111/j.1365-246X.2012.05476.x.

C. Xu, Y. Liu, Y. Wen, and R. Wang. Coseismic slip distribution of the 2008 Mw 7.9 Wenchuan Earthquake from joint inversion of GPS and InSAR data. *Bull. Seism. Soc. Am.*, **100**(5B) 2736–2749, 2010a. DOI 10.1785/0120090253.

Y. Xu, Z. Li, R. Huang, and Y. Xu. Seismic structure of the Longmen Shan region from S-wave tomography and its relationship with the Wenchuan Ms 8.0 earthquake on 12 May 2008, southwestern China. *Geophys. Res. Lett.*, **37**(2) L02304, Jan. 2010b. DOI 10.1029/2009GL041835.

Y. Yagi. Source rupture process of the 2003 Tokachi-oki earthquake determined by joint inversion of teleseismic body wave and strong ground motion data. *Earth Planets Space*, **56** 311–316, 2004.

Y. Zeng and J. G. Anderson. A composite source model of the 1994 Northridge earthquake using genetic algorithms. *Bull. Seism. Soc. Am.*, **86**(1B) S71–S83, 1996.

Y. Zeng, J. G.Anderson, and G. Yu. A composite source model for computing realistic synthetic strong ground motions. *Geophys. Res. Lett.*, **21**(8) 725–728, 1994. DOI 10.1029/94GL00367.

J. X. Zhao, J. Zhang, A. Asano, Y. Ohno, T. Oouchi, T. Takahashi, H. Ogawa, K. Irikura, H. K. Thio, P. G. Somerville, Y. Fukushima, and Y. Fukushima. Attenuation relations of strong ground motion in japan using site classification based on predominant period. *Bulletin of the Seismological Society of America*, **96**(3) 898–913, 2006. DOI 10.1785/0120050122.

A. Zollo, G. Iannaccone, M. Lancieri, L. Cantore, V. Convertito, A. Emolo, G. Festa, F. Gallovič, M. Vassallo, C. Martino, C. Satriano, and P. Gasparini. Earthquake early warning system in southern Italy: Methodologies and performance evaluation. *Geophys. Res. Lett.*, **36**(5) L00B07, Feb. 2009. DOI 10.1029/2008GL036689.

Acknowledgements

At this point I like to express my thanks to all who accompanied me along my way to this thesis.

Thanks to everyone who gave useful comments and criticism, hints and motivation.

Thanks to Frank Scherbaum for providing advice, for not giving up on me and for helping me to see the bigger picture.

Thanks to Sebastian Hainzl for his patience, for his support, for his scientific criticism, for repeated corrections and his trust.

Thanks to Rongjiang Wang for his enormous help at the start of my PhD, for his enthusiasm and his believe in the method.

Thanks to Konrad Kieling for his patience, for proofreading, for not giving up and again more patience.

Thanks to Camilla Cattania for proofreading, for nice chats in the office and for her curiosity.

Thanks to Olga Zakharova, Christoph Bach, Sanjay Singh Bora and Christian Molkenthin for helpful discussions, for distraction and just being around.

Thanks to Sreeram-Reddy Kotha for providing his calculations, over and over again.

Thanks to Fabrice Cotton for expressing his interest in my work at a stage when I almost lost my interest.

Thanks to Eleonora Rivalta for leading our very helpful “writing club” and being a role model.

Thanks to all people in section 2.1 of GFZ. It was a pleasure working among you.

Thanks to all of my family for providing support and suffering my moods.

Thanks to Frank Krüger, who taught me all the basics about ten years ago, who passed on his passion for seismology and showed me how exciting a seismogram can be.

Thanks to my dad, without whom I would not have started the way.

Declaration

Herewith I declare, that I prepared the Thesis "Quantification of ground motions by broadband simulations" on my own and with no other sources and aids than quoted. This work has not previously been presented in identical or similar form to any other examination board.

Hiermit erkläre ich an Eides statt, dass ich die vorliegende Dissertation "Quantification of ground motions by broadband simuations" selbständig angefertigt habe und keine weiteren außer den angegebenen Quellen und Hilfsmitteln verwendet habe. Diese Arbeit hat in gleicher oder ähnlicher Form noch keiner anderen Prüfungsbehörde vorgelegen.

Potsdam, June 22, 2015